Volumetric Optical Strain Mapping Technique for Strain Measurement in Monolithic Silica Aerogel Nanocomposites

Submitted by

Allen G. Ma

in partial fulfillment of the requirements for the degree of

Master of Science in Mechanical Engineering

School of Engineering
Tufts University
Medford, Massachusetts
February 2021

Author ....
Department of Mechanical Engineering
August 31, 2020

Certified by..
Dr. Stephen Alan Steiner III
Aerogel Technologies, LLC
Thesis Supervisor

Certified by..
Dr. Jeffrey S. Guasto
Professor of Mechanical Engineering
Thesis Supervisor

Certified by..
Dr. Richard J. Henshaw
Postdoctoral Associate
Committee Member

Certified by..
Dr. Marc Hodes
Professor of Mechanical Engineering
Committee Member

Accepted by...
Dr. Chris Rogers
Professor of Mechanical Engineering
Chair, Department of Mechanical Engineering

Abstract

Aerogels are a diverse class of high-porosity solid-phase nanostructured materials that exhibit a wide range of extreme materials properties, such as low bulk density and low thermal conductivity. Aerogel products can be made in various form factors, with the most common commercial form factors being blankets and particles. Aerogel monoliths (i.e., shaped 3D aerogel forms) offer unique opportunities for applications such as insulating windows and polymer aerogel products that can be machined into complex shapes without collapsing. However, monoliths can crack, deform, or otherwise undergo mechanical failure during supercritical drying, requiring overly conservative and thus time-consuming and expensive processes to achieve usable parts. The mechanisms for such failure are not fully understood, as they could possibly be due to solvent-solid interactions or nonuniform strain states. It is necessary to be able to make *in situ* strain measurements during the drying process to understand these failure mechanisms. Volumetric optical strain mapping during supercritical drying is a promising method for measuring strain in real time. Here, we develop a technique for strain mapping by utilizing photon upconversion fluorescent particles and mapping the fluorescence intensity of upconversion nanoparticles to the strain state of the drying gel. To demonstrate this capability, we first establish the ability to illuminate a voxel within an aerogel with infrared lasers. The voxel is used as an optical probe for interrogating a given location within the monolith. A silica aerogel nanocomposite is embedded with inorganic $NaYF_4$:Yb/Er upconversion nanoparticles (UCNPs). We demonstrated the feasibility of utilizing UCNPs for volumetric strain mapping in *ex situ* analysis, and with modification to the technique there is promise for *in situ* applications.

Acknowledgements

The work described in this thesis was performed in support of a collaboration among Tufts University, Missouri University of Science and Technology, and Aerogel Technologies, LLC, and was funded by the National Science Foundation under the award CMMI-1530603. The author thanks his advisors (Dr. Stephen A. Steiner III, Prof. Jeffrey S. Guasto), committee members (Dr. Richard J. Henshaw, Prof. Marc Hodes), and collaborators at Tufts University (Georgios Karamanis) and Aerogel Technologies (Justin S. Griffin, Ryan A. Nelson) for their support and guidance throughout the course of this work. The author also acknowledges the Center for Nanoscale Systems at Harvard University, which provided valuable assistance in characterizing materials in this work.

Table of Contents

List of Figures

List of Tables

Chapter 1:

Introduction

Aerogels are a diverse class of high-porosity solid-phase nanostructured materials that exhibit a wide range of extreme materials properties, such as extremely low bulk density, high internal surface area, high strength-to-weight mechanical properties, and low thermal conductivities [1–3]. The materials properties of an aerogel can be tuned over a wide range of values by adjusting the composition and synthesis parameters. For example, silica aerogels can be transparent and are electrically insulating [1,4], while carbon aerogels have high opacity and are electrically conductive [1]. Such extreme and tunable properties make aerogels useful for a wide range of challenging technological applications, such as thermal superinsulation for buildings [5,6], winter apparel [7,8], automotive thermal engine covers [9] and vehicle thermal management systems [10], and carbon dioxide capture [11–13], all of which can help to solve pressing issues such as the mitigation of climate change.

For most types of aerogel materials, manufacturing of an aerogel involves four stages: sol-gel-based formation of a wet-gel precursor, aging of the resulting gel, solvent exchange of the pore fluid in the gel for a pure solvent, and finally, removal of the pore fluid from the gel. A gel has two components, a nanoporous solid skeleton that gives the gel its structure, and a liquid permeating the pores of that skeleton. The skeleton of the gel will eventually become the aerogel. The composition of the gel precursor and the subsequent morphological, chemical, and mechanical changes the skeleton of that gel experiences as the gel is processed into an aerogel define the properties of the resulting aerogel. For example, in the case of silica-based aerogels, the first manufacturing step involves formation of a silica wet-gel precursor, in which the silica skeleton of the gel is formed when the silica precursor polymerizes into nanometer-scale particles that crosslink to form the skeleton [1,14]. Next, the gel is aged to increase the mechanical strength of the silica structure; unreacted monomers add to the initial skeletal network, and silica precipitates out of solution to further strengthen the network. After aging, a solvent exchange step is performed, where the gel is placed in sequential baths of a pure solvent, during which the target solvent displaces the solvent within the pores of the gel via diffusion and dilution. This prepares the gel for the drying stage, in which the pore fluid of the gel is extracted and replaced by a gas. There exist several methods for extracting the pore fluid from gels to produce aerogels, such as supercritical drying, evaporative ambient pressure drying, and freeze drying. If the solvent in a gel is evaporated under ordinary ambient conditions, the solvent within the pores undergoes a phase change from liquid to gas, creating a gas-liquid interface. This interface creates very high capillary stresses due to the small pore size within the gel (~20-40 nm), and typically leads to collapse of the solid structure of the gel [1].

The resulting low-porosity material is called a xerogel [15], and it is structurally distinct from an aerogel. To dry a gel and produce an aerogel, the pore fluid of the gel must be removed from the gel's solid skeleton such that the nanoporous skeleton of the gel does not undergo significant irreversible shrinkage. Supercritical drying with carbon dioxide ($SCCO_2$ drying) is the method most commonly utilized to make aerogels today [16]. Supercritical drying is a process through which the pore fluid is heated and pressurized to beyond the pore fluid's critical point (the temperature/pressure beyond which the gas and liquid phases can no longer be distinguished), and so the pore fluid is now called a supercritical fluid. There is no gas-liquid interface for supercritical fluids, so the removal of the pore fluid will not produce the capillary stresses that result in the structural collapse of the gel skeleton. Since supercritical drying typically involves high temperatures and pressures, it is safer to first exchange a gel's pore fluid for a nonflammable solvent such as CO_2. $SCCO_2$ drying circumvents the problem of capillary stresses by exchanging the original solvent with liquid CO_2, then heating/pressurizing the new CO_2 solvent. As the pressure and temperature increase beyond the critical point, the liquid CO_2 transitions to a supercritical fluid. Supercritical fluids exhibit no gas-liquid interface and thus exert no capillary stresses throughout the pore structure as they diffuse out of the gel's solid structure. The $SCCO_2$ becomes gaseous following an isothermal reduction in pressure, and the gel becomes an aerogel.

Aerogels are commonly produced in several different form factors, including particles/granules used for insulation of pipes, and blankets used when flexible insulation is required [1]. While particles and blankets are cheap and simple to produce compared to other form factors, they lack structural rigidity and do not have isotropic properties (particles are nonuniform in size and shape, and blankets are fibrous). Monolithic aerogels (shaped contiguous aerogels such as plates) are used in applications that particles and blankets cannot be. For example, transparent monoliths can be used in insulating windows [17], and polymer aerogels with high strength and stiffness properties and low friability can be machined into complex shapes that hold their form without collapsing, allowing for use in applications such as lightweight airline interior wall panels [18].

However, the manufacture of monolithic aerogels introduces challenges not faced by the manufacture of particles or blankets. In particular, aerogel monoliths can crack, deform, or otherwise undergo mechanical failure during the drying process [16]. This hinders broad commercialization of monoliths, resulting in low part quality, low product yields, difficult-to-scale manufacturing processes, and/or increased costs, thereby making large-scale production of monolithic aerogel parts difficult. However, the mechanisms for such failure modes during supercritical drying are not fully understood. Supercritical drying involves the heating and pressurization of fluid within nanoscale pores to beyond the critical point, resulting in complex stress and strain states dependent on fluid composition (the interaction of the liquid pore fluid with liquid CO_2 and $SCCO_2$ changes as more of the original solvent is exchanged out), time (the aforementioned fluid composition changes over time), and space (the geometry of the gel affects stress and strain), all of which can invoke unexpected and undesired mechanical responses.

Having the capability to make *in situ* strain measurements during the drying process is a desirable but missing technique for understanding these failure mechanisms. Presently, the techniques used to investigate the mechanical properties of aerogels include uniaxial and biaxial tension tests, FTIR spectroscopy, and SEM imaging [19,20]. These methods can be performed only on monoliths post-manufacturing, because the equipment required for these techniques is incompatible with the complex pressure vessels used for aerogel drying due to size, transparency, and/or harsh environmental conditions. Strain mapping is a technique that could be used to measure envelope strain [21–24], but it is usually limited to surface strain as it lacks the penetrative ability to see within complex geometries (such as those of a 3D aerogel part), where the strain state can be very complex. This necessitates the need for a technique that can see within a monolith, even while it is still drying in a pressure vessel. Volumetric optical strain mapping during supercritical drying would thus be a promising method for measuring 3D strain states within aerogels in real time and could enhance our understanding of the origins of part failure in the manufacturing of monolithic aerogel materials.

Here, we develop a technique for volumetric strain mapping within a post-drying transparent silica monolith by utilizing fluorescent upconverting particles and mapping the fluorescence intensity of the particles to the strain state of an aerogel as a first-step towards *in situ* volumetric strain mapping of aerogels during supercritical drying. To demonstrate this capability, we establish the ability to illuminate a visible voxel ("volumetric pixel") within an aerogel using an infrared laser. The voxel is then used as an optical probe for spatially scanning and interrogating the strain state at a given location within the monolith.

1.1: Motivation

Supercritical drying is the technique most often used when manufacturing aerogel products [16]. Aerogel form factors such as particles and blankets can be made efficiently with large-scale supercritical drying, but such techniques are not always practical or amenable for the manufacture of monoliths; particles are made with subcritical drying techniques that result in large deformations and pulverization, while blankets do not need to preserve their mechanical properties because the gel is reinforced with fibers [1]. Monolith manufacture is slower and more complicated than the manufacture of other form factors due to issues like solid-solvent interactions (e.g., the interactions between the solid gel skeleton and the liquid pore fluid) and nonuniform strain states that lead to structural failures of the monoliths, such as cracks and fractures [16]. Supercritical drying of monoliths is also diffusion-limited and involves the exchange of one fluid for another, which introduces entropy of mixing effects. The gel skeleton may also undergo unexpected distortions due to the high temperatures and pressures of supercritical drying, and the compositions of certain gels may trap solvents within the pore structure/skeleton and prevent complete solvent exchange. These issues further complicate monolith production.

Since supercritical drying involves exposure of the gel to (supercritical) fluids at elevated temperatures and pressures, it must be performed in heavy-duty stainless steel pressure vessels that make direct measurements of drying gels challenging. The inability to observe and quantitatively measure monoliths as they are drying has limited the opportunities to understand the exact mechanisms that can lead to failure. Thus, it is necessary and crucial that *in situ* observation of drying monoliths be developed.

1.2: Thesis Outline

In this thesis, the development of a volumetric optical strain mapping technique for measuring the 3D strain state within aerogels using strain-dependent upconversion emission from micro- and nanoparticles in an aerogel nanocomposite is discussed. This works serves as the foundation for future work which will focus on applying such a technique to the observation of drying aerogel monoliths *in situ* for measuring the strain state of a drying aerogel monolith in real time.

In Chapter 2, an overview of aerogels and their properties is discussed, as well as the significance of aerogels in technological applications, including those that can serve to mitigate climate change. This is followed by a discussion of the physics of upconversion emission and its applicability to this work and overview of strain mapping techniques that have been used before for measuring strain states.

In Chapter 3, the objectives and the methodology of this thesis are presented. The approach used to develop a volumetric optical strain mapping technique is described.

In Chapter 4, the synthesis of novel monolithic silica aerogel nanocomposites embedded with upconverting micro- and nanoparticles is detailed. Synthesis and characterization of silica nanocomposites using commercially-available upconverting micro- and nanoparticles is described, as well as efforts made to synthesize various types of upconverting nanoparticles.

In Chapter 5, the development of a volumetric optical strain mapping technique for measuring the non-linear optical response of upconverting silica aerogel nanocomposites presented in Chapter 4 is described. The approach used to develop the technique is presented, including the design of supporting instrumentation used such as laser optics, motorized linear stages, and data collection, along with efforts undertaken to achieve an appropriately-shaped millimeter-scale single-voxel probe.

In Chapter 6, measurements of emission intensity of upconverting silica aerogel nanocomposites using the aforementioned instrumentation are presented. Measurements of voxel brightness in nanocomposite monoliths versus applied compressive load are made at the single-voxel level. The evolution from performing measurements with single voxels to full-monolith-volume brightness intensity mapping is detailed in support of developing a method for volumetric optical strain mapping of already-dried silica aerogel nanocomposites *ex situ* of a supercritical dryer.

In Chapter 7, the results of numerical simulations of compression of multiple aerogel formulations are presented. Models of silica aerogel, cellulose aerogel, and two formulations of graphene aerogel with different Poisson's ratios are subjected to varying levels of stress, and the effects of variable stress and variable particle size on volumetric strain are described. The results of the simulations are used to inform the direction of potential additional physical experiments.

In Chapter 8, important discoveries of this thesis are summarized, and recommendations for future work and practical implementation of this strain mapping technique are presented.

Chapter 2: Background

The various properties of aerogels have made them very attractive in many applications, from the commonplace (e.g., cosmetics) to the exotic (e.g., collection of comet dust). Their potential use in mitigating climate change through improving energy efficiency in industry, commercial buildings, and transportation has been explored by many, as discussed in this chapter. In this chapter, we survey the fundamentals of aerogels as a materials system, their production, and their applications, as well as review the physics of upconversion emission and its applicability to this work and the state of the art of optical strain mapping as it applies to related material systems.

2.1: Properties of Aerogels and Aerogel Production

Aerogels are a diverse class of dry, porous, low-density materials that have a wide range of extreme properties. For example, silica aerogels have pores on the nanoscale (average pore diameter of 20 to 40 nm), high pore volumes (typically above 90%), high surface areas (around

1000 m^2 g^{-1}), and low densities (on the order of 0.020 g cm^{-3}) [1–3]. Silica aerogels are generally nonflammable and have low thermal conductivities (typically around 0.015 W m^{-1} K^{-1}, in comparison to polyurethane foam at 0.025 W m^{-1} K^{-1}) [1,25], making them excellent for use as thermal insulation. Of particular interest for our current work is the high optical transparency of silica aerogels (with a transmission coefficient of 93%) and their low refractive index (approximately 1.05) [1,4]. These properties have made silica aerogels a viable option in certain niche applications where the brittleness and difficulty of manufacture are outweighed by their unique materials properties, such as Cherenkov radiators in nuclear experiments [26], or as insulation for the electronics of the Sojourner Mars rover from the extreme temperature swings of Mars [27]. However, their high cost of production limits aerogel product usage.

Production of aerogels can be separated into four distinct stages: sol-gel-based formation of a wet-gel precursor, aging of the resulting gel, solvent exchange of the pore fluid in the gel for a pure solvent, and finally, removal of the pore fluid from the gel (Fig. 2.1). The first stage, gelation, results in the formation of the gel skeleton. For silica-based aerogels, silica molecules in aqueous solution undergo polymerization and bond together to form particles. These particles further bond together to form yet larger particles that eventually crosslink, creating chains of silica particles. These chains constitute the gel skeleton, with the gaps between the chains forming the nanoporous structure of aerogels [1,14,28].

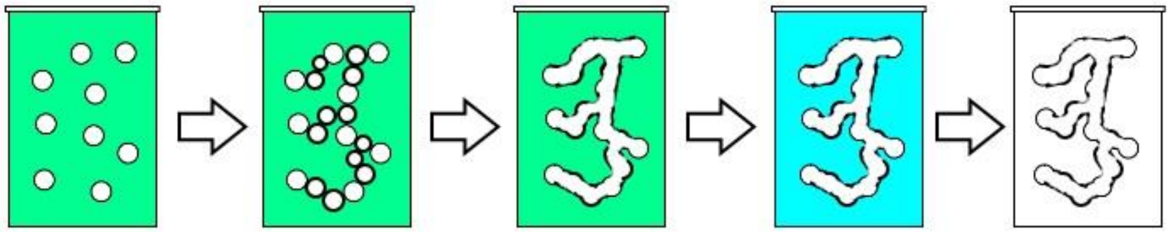

Figure 2.1 A silica precursor undergoes gelation to form the skeleton, aging to strengthen the network, solvent exchange to purify the pore fluid, and drying to become an aerogel.

The next stage, aging, strengthens the skeleton. After gelation, the solution still has unreacted silica monomers, so leaving the wet-gel to sit in the solution for several hours or days after gelation allows for those unreacted monomers to bond to the skeleton. The dissolution-reprecipitation of silica enhances the inter-particle necks that connect the particles of the skeleton together [1,16,29,30].

The next stage is solvent exchange. Gels can be formed in many different solvents, like water, n-hexane, methanol, and ethanol [31,32]. However, not all solvents are miscible with liquid CO_2, and if the next stage, drying, utilizes $SCCO_2$, the solvent within the pores of the gel must be miscible with CO_2. In addition, even if the solvents are miscible with CO_2, if the pore fluid has impurities that are not miscible (e.g., water from the gelation stage), then drying the gel will likely lead to structural failure due to capillary stresses. Thus, the gel is placed in sequential baths of a pure solvent, displacing the impure pore fluid via diffusion and dilution. This prepares the gel for the drying stage, in which the pore fluid of the gel is extracted and replaced by a gas.

The final stage of aerogel production is the drying stage, where the pore fluid within the gel is replaced with CO_2/air. There exist several methods for extracting the pore fluid from gels to produce aerogels, such as supercritical drying, evaporative ambient pressure drying, and freeze drying. Ambient pressure drying can produce larger quantities of aerogels, but if the solvent in a gel is evaporated under ordinary ambient conditions, the solvent within the pores undergoes a phase change from liquid to gas, creating a gas-liquid interface. This interface creates very high capillary stresses due to the small pore size within the gel (~20-40 nm), and typically leads to collapse of the solid structure of the gel [1]; the resulting low-porosity material is called a xerogel, due to its properties being very distinct from those of an aerogel's. Much progress has been made to improve the viability of ambient pressure drying, with Aerogel Technologies producing the largest monolithic aerogel in the world using ambient pressure drying [33–37].

Freeze drying and supercritical drying both avoid capillary stresses by circumventing the phase change from liquid to gas, though they do so in different ways. Freeze drying freezes the liquid pore fluid into a solid before subliming the solid solvent directly into a gas. This avoids capillary stresses, but it still can damage the gel structure through the growth of the solid solvent crystals. The transparency of freeze-dried silica is also decreased when compared to supercritically dried monoliths. The process is very time-consuming and energy-intensive [38], so it is not used often to dry aerogels, but recent efforts have been made to improve the viability of the drying method [39–43].

To dry a gel and produce an aerogel, the pore fluid of the gel must be removed from the gel's solid skeleton such that the nanoporous skeleton of the gel does not undergo significant irreversible shrinkage. To this end, $SCCO_2$ drying is the method most commonly utilized to make aerogels today [16]. $SCCO_2$ drying circumvents the problem of capillary stresses by exchanging the original solvent with liquid CO_2, then heating/pressurizing the new CO_2 solvent. Many studies on $SCCO_2$ drying have been motivated by a desire to increase understanding of the fundamentals governing the transport process, for example, diffusion coefficients and densities of dynamically-changing fluid mixture compositions [44–47], solvomechanical responses of porous substrates [48,49], and drying rates [44,50,51], but none have attempted direct measurements of the strain state of an aerogel monolith while drying *in situ*. Kocon et al. investigated a technique to supercritically dry ultralow density uncracked transparent silica aerogels with low shrinkage [52]. García-González et al. studied how drying time duration affected the end textural properties of the dried aerogels; for silica aerogels, they found that short drying times resulted in nontransparent monoliths with cracks and shrinkage, while longer drying times increased transparency and mechanical stability [50]. Sanz-Moral et al. found that the majority of noticeable aerogel shrinkage of silica monoliths occurred during CO_2 decompression at the end of the drying process [53]. Griffin et al. investigated the kinetics of the $SCCO_2$ drying process by continuously measuring alcohol extraction rates; their results were comparable to a conjugate mass transfer model assuming pure diffusion [44]. Quiño et al. used one-dimensional Raman spectroscopy to perform *in situ* analysis of the ethanol-CO_2 concentration profiles within a drying silica monolith [54]. These studies have furthered understanding of the mechanisms that can affect the monolith as it dries. Quiño et al. in particular recognized the importance of *in situ* analysis; before their work, there were no measurements directly revealing the mass transport mechanisms within drying gels [54]. However, none of these studies directly determined the strain state of the aerogel skeleton as the monolith dried, an important consideration that is missing from the literature.

2.2: Significance of Aerogels: Environmental, Economic, and Societal Importance

The extreme properties of aerogels allow for a wide range of applications. One of those applications is in the mitigation of climate change. Due to the threat of anthropogenic global warming, there is a desire to decrease global greenhouse gas emissions, particularly CO_2 released through the burning of fossil fuels. Improving energy efficiency of major sources of emissions is one important way this could be achieved. According to the EPA [55], in 2017, the largest sources of CO_2 emission in the US came from transportation (28.9%) and electricity production (27.5%). While new and improved technologies have been and are currently being developed to decrease energy consumption in the transportation and power generation sectors, the effects of these improvements are largely long-term; immediate progress must be made to decrease CO_2 emissions to meet the proposed goal of a stabilized atmospheric CO_2 concentration below 500 ppm [1,56]. The porous nature of aerogels has prompted the exploration of their application in carbon capture [11–13,57–59], and recently aerogels were investigated for methane adsorption [60] and storage [61]. However, it is through the use of aerogels as superinsulation in buildings and as lighter-weight alternatives to existing structural materials used in automobiles and airplanes [18] that they can provide immediate reductions in greenhouse gas emissions.

The buildings sector accounts for roughly 40% of global energy consumption, and HVAC (heating, ventilation, and air conditioning) accounts for the bulk of a building's energy costs. However, the effectiveness of thermal insulation in many buildings globally is poor [5]. In Europe, buildings are responsible for about 36% of total CO_2 emissions, and about 68% of a building's energy consumption is spent on heating and cooling [62]. It is through this that immediate improvements may be made worldwide. This is an application where the thermal insulation properties of aerogels make them very attractive [6].

In 2014, the global aerogel market was estimated to be about USD 353.88 million. Almost 91% of that market was in the oil and gas and construction segments; most aerogel products used in these sectors are for insulation, as there is a high demand for materials with very low thermal conductivity. Predicted global aerogel market will be USD 547.96 million in 2019, with 84% of that in the oil and gas and construction segments [63]. However, the global insulation market was valued at USD 52.30 billion in 2017 [64]. Thus, despite the superlative insulative properties of aerogels, the market share of aerogel products used as insulation was less than 0.9% of the global insulation market.

When aerogel products are used in insulation, they are usually blankets, as they are flexible and easier to produce than monoliths. Two of the leading manufacturers of aerogel insulation in the world, Cabot Corporation and Aspen Aerogels, primarily produce blankets (and particles, for Cabot) and usually sell only to industrial partners and government labs [37,65,66]. In 2004, Aerogel Technologies sought to commercialize monoliths with the goal of making aerogel products readily accessible to the public. Over the next 15 years, Aerogel Technologies developed and commercialized a mechanically robust aerogel monolith without compromising its low thermal conductivity, and they collaborated with private companies like Ford and Airbus and government agencies like NASA to explore the potential applications of these new monoliths [9,18,37]. This development suggests that monoliths are a very promising new form factor, as they can be utilized not just for thermal insulation, but also for acoustic insulation, construction, and transportation.

However, monolith production introduces difficulties that blanket production does not. During the drying process, aerogel parts can undergo various failures. They can shrink, crack, warp, fracture, and otherwise deform; if the aerogel part was intended to have a specific shape or uniform properties, any of these failures could render the aerogel unusable. For blankets, deformations are not usually a concern, as the fibers of the blanket bind with the aerogel. However, for the applications that require monoliths (e.g., insulated windows; approximately 20% of the energy loss of a one-story house is through the windows [67]), deformations are very important. Scherer has done much work in analyzing stress mechanics during supercritical drying. His work with Smith and Anderson [68] demonstrated that gel shrinkage is largely caused when the capillary pressure exerted by the pore fluid (affected by drying rate and fluid composition) exceeds the modulus of the solid skeleton. He also found that pressure gradients in the pore fluid result in differential strain, creating additional drying stresses, and that severe stresses occur wherever the gel is in contact with its container and when the heating rate and/or depressurization rate are excessive [29,69,70]. Bisson et al. also had similar results, where shrinkage occurs due to the imbalance between capillary pressure and resistance to compression of the skeleton, and that gel fracture can result from rapid heating and depressurization causing the evaporative flow rate to become too high [16].

Thus, the complexity of avoiding these failure modes increases the difficulty (and the cost) of aerogel monolith production, especially when it is not always known exactly what it was that caused any one failure. To better understand the underlying mechanisms that cause these failure modes, it is necessary to understand the stresses and strains throughout the monolith as it dries. While capillary stresses are one known source of stress during drying, there are other stresses which can cause aerogel failure during drying. For this reason, one must observe the drying process *in situ*; it is not always known which of these stresses caused any particular failure, so observations as the failure occurs are crucial.

2.3: Upconverting Nanoparticles for *In Situ* Observations

Supercritical pressure vessels are generally made of thick-wall stainless steel bodies that offer limited optical access and other direct measurement techniques, but for this project, a pressure vessel with six orthogonal sapphire windows was commissioned, allowing the observation of any monoliths placed inside throughout the drying process. The monoliths used were silica monoliths embedded with upconverting nanoparticles (UCNPs). These UCNPs absorb light of a specific wavelength (e.g., infrared), then emit light of a shorter, high-energy wavelength (e.g., visible). We propose that by mapping the concentration of the UCNPs to the intensity of their emission, the strains that occur within the monolith structure during the drying process can be mapped as well, thus furthering understanding of the reasons for structural failures.

In typical single-photon fluorescence, a single photon of a certain wavelength and energy is absorbed by an orbital electron of an atom, molecule, or nanostructure. The energy from the absorbed photon excites the electron to a higher energy state. When the electron relaxes back to its ground state, part of the absorbed energy is released as a photon with a longer wavelength and less energy than the absorbed photon; the rest of the energy is lost to thermal modes. In two-photon absorption, two photons arrive at a single electron "simultaneously" (within 0.5 fs) and are absorbed together. Their combined energies push the electron to a higher energy state than would a single absorbed photon. Thus, when that electron relaxes back to its ground state, the emitted photon has a shorter wavelength and higher energy than either of the two individual photons that were absorbed [71,72]. In this way, infrared light can be absorbed by a nanoparticle and reemitted in the visible spectrum. Two-photon imaging has many applications in the biomedical sciences, as it allows researchers to perform experiments on live animals and cells with minimal tissue damage [71,73–76]. The infrared radiation used has less energy than ultraviolet, which decreases the likelihood of causing damage to living tissue. Similarly, infrared light is unlikely to damage silica aerogels monoliths; silica aerogels have low absorption of near-IR radiation [77], limiting any damage that could occur from high levels of IR light.

While similar to two-photon absorption, upconversion emission has a significant difference: two-photon absorption requires the two photons to be absorbed within femtoseconds of one another (and thus the process requires very high instantaneous power densities), but with upconversion, the time between the absorptions of the two photons is on the range of 10^{-5} s (i.e., microseconds). Thus, upconverting phosphors can visibly emit light at much lower power densities than can two-photon phosphors. This makes upconversion an attractive and viable alternative to two-photon in low-scattering, deep-penetration imaging [78,79], such as the imaging that is desired for this project. Additionally, because upconverting phosphors do not require the high power densities of two-photon phosphors, weaker lasers that are more compact can be used. This feature allows for the utilization of upconversion in experiments with high spatial limitations, such as within the confines of a pressure vessel.

The most commonly studied mechanisms of upconversion are excited state absorption (ESA) and energy transfer upconversion (ETU). ESA is similar to two-photon absorption (2PA), with the most significant difference being the time scale. In ETU, the mechanism is more distinct from 2PA. Two electrons absorb one photon each, and each electron moves to the first excited state S_1. One of the excited electrons transfers its energy to the other electron. The first electron falls back to the ground state, while the second electron jumps up to the second excited state S_2. Then, the second electron falls back down to the ground state, releasing its energy as a single photon with shorter wavelength than the wavelengths of the absorbed photons.

The fluorescent materials used in this work are lanthanide-doped nanoparticles. The 4f orbitals of lanthanide ions allow for a large number of possible excited states, thus promoting the circumstances in which upconversion can occur. $NaYF_4$:Yb/Er nanoparticles are very commonly used, and so there is an abundance of work demonstrating their effectiveness [80–88]. A recent paper by Lei et al. demonstrated a viable method of synthesizing $NaBiF_4$:Yb/Er nanoparticles [89]. Substituting bismuth for yttrium allows for a quick and simple process for cheaply producing large quantities of nanoparticles, and the mechanisms of fluorescence for both the $NaYF_4$:Yb/Er particles and the $NaBiF_4$:Yb/Er particles are very similar. These NPs undergo ETU; the ytterbium absorbs the photons and passes the energy to the erbium, which then emits the new photon. The absorbed photons have a wavelength of 980 nm (infrared light), whereas the emitted photons have a wavelength of 540 nm (green visible light).

2.4: Strain Mapping Techniques

Digital image correlation (DIC) is a computer vision technique that compares the features in a pair of digital images of a subject before and after deformation, thus extracting whole field displacement data. It is a powerful technique for measuring surface strain and is used often in the literature [22,90–93]. X-ray tomography has been used in the development of digital volume correlation (DVC), the 3D analog to DIC [21,24,94]. However, neither DIC nor DVC can be utilized *in situ*. Thus, having the capability to make *in situ* strain measurements is a necessary but missing technique for understanding the strain state of complex objects like 3D aerogel parts.

2.5: 3D Illumination and Volumetric Displays

While the focus of this work is on strain mapping in aerogel monoliths, the demonstration of voxel illumination of embedded fluorescent particles has applications in other areas, such as in 3D volumetric displays. By focusing and aiming IR light at specific voxels within the monolith, an image in 3D space can be created. As demonstrated by Wang and Liu [80], by varying the lanthanides used in the synthesis of the UCNPs and the wavelengths of the IR incident light, one can control the wavelength of the emitted visible light. Thus, not only can a three-dimensional image be formed, but that image can also be in full RGB color as well. Though other groups have published work on 3D volumetric illumination and displays [95–102], no other groups have used aerogels as the solid medium for the UCNPs. This potential application of the illumination technique is an interesting topic to pursue in future experiments, though the technique has had more development as a strain mapping tool in this work.

Chapter 3:

Objectives and Approach

The goal of this work was to develop a technique that enables measurements of the strain state of a transparent aerogel monolith in real time. Collecting real-time information on the strain state of a drying aerogel monolith would further our understanding of the mechanics of drying aerogels. We can then reduce manufacturing costs by implementing that knowledge to decrease the number of mechanical failures that often occur during drying.

We hypothesized that embedding fluorescent particles into the solid skeleton of transparent silica monoliths would allow us to optically probe the strain of said monolith. The known concentration of particles would correlate with fluorescence intensity, thus changes to the intensity of the fluorescence was hypothesized to correlate to changes to the structure of the monolith (i.e., strain) (Fig. 3.1). By mapping fluorescence intensity to strain, any changes to the intensity could be used to determine the strain state of the monolith *in situ*, including during the drying process.

To test this hypothesis, we used fluorescent upconversion $NaYF_4$:Yb/Er nanoparticles and embedded them within silica aerogel monoliths at known concentrations. These fluorescent silica nanocomposites were subjected to known loads while voxels were systematically illuminated within the monolith by a focused 980 nm infrared laser. The intensity of the fluorescence of the illuminated voxel was observed with a camera as a function of time, a function of space, and a function of induced strain. These *ex situ* strain measurements were used to establish a correlation between fluorescence and strain. The conclusions reached through these physical experiments were complemented with simulations and modelling in COMSOL.

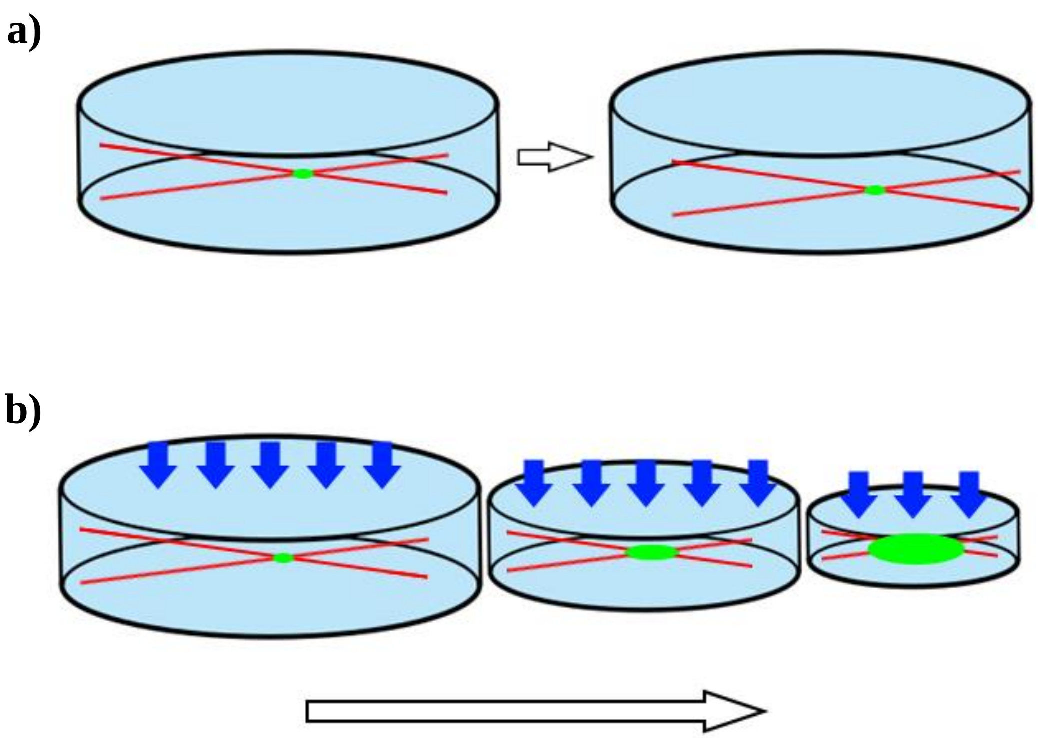

Figure 3.1 A description of the 3D volumetric strain mapping technique. a) A focused infrared laser beam leads to fluorescence at the focal spot (i.e., the "voxel"). As the focal spot moves throughout the monolith, the voxel moves as well. b) The intensity of the fluorescence of the voxel changes based on the particle density of the fluorescent particles. Increasing volumetric strain increases the particle density, which in turn increases the intensity of the fluorescence.

Future steps include 1) applying the established correlation between fluorescence intensity and induced strain to determine static strain states during supercritical drying, and then 2) mapping the dynamic strain states *in situ*. The technology developed in the refinement of this technique could be used for real-time strain measurements of any translucent material that can support embedded fluorescent nanoparticles. Novel volumetric displays could be invented using this technique as well. The *ex situ* strain measurements are a proof of concept to help understand the technical and engineering advantages, challenges, and limitations of the technique.

Chapter 4:

Development of Upconversion Silica Aerogel Composite Monoliths

The ultimate goal of this work was to develop a technique that could measure the strain state of a drying aerogel monolith in real time. The monoliths would be embedded with fluorescent particles during the gelation process, then those particles would be exposed to infrared light to induce fluorescence. To observe the monoliths drying *in situ*, the monoliths must be produced in-house and cannot be purchased elsewhere. The particles can be purchased from external sources, but the low quantities and high costs of commercial nanoparticles limit the number of composite monoliths that can be produced. As such, the synthesis of fluorescent nanoparticles in-house was first explored, before both commercial microparticles and commercial nanoparticles were purchased.

4.1: Methods and Materials for the Production of Composite Monoliths

Two formulations of nanoparticles were followed: the first by Wang and Liu [80], and the second by Li and Zhang [81]. These papers outlined how to synthesize $NaYF_4$:Yb/Er nanoparticles, though their methods differed (see Chapters 4.1.2 and 4.1.3). A third protocol, taken from a paper written by Lei et al. [89], outlined how to synthesize $NaBiF_4$:Yb/Er nanoparticles, substituting yttrium (an expensive rare-earth metal) for bismuth. After each protocol was followed, the resulting nanoparticles were embedded within silica aerogel monoliths at concentrations of at least 0.01 mg/mL during gelation. The aerogel composites were then exposed to 980 nm laser light, and any fluorescence was recorded.

4.1.1: Procedure for Setting/Drying Silica Aerogel Monoliths with Embedded Particles

To set the aerogel monolith, the protocol for silica aerogel from Aerogel.org was followed, with minor modifications to quicken setting times and to introduce the particles [103]. A 1.458 millimolar stock solution of ammonium fluoride dissolved in deionized water was prepared. For a fluorescent nanoparticle concentration of 0.01 mg of particles per mL of sol, a solution of 10 mL of tetramethoxysilane (TMOS), 10 mL of methanol, and 0.35 mg of particles was prepared in a glass beaker. The catalyst solution was prepared by mixing 5 mL of ammonium fluoride stock with 54 µL of ammonium hydroxide and 10 mL of methanol in a separate glass beaker. The TMOS/particle solution was sonicated for 5 minutes, after which the catalyst solution was immediately poured into the TMOS/particle solution and stirred for 3 minutes. The mixed solution

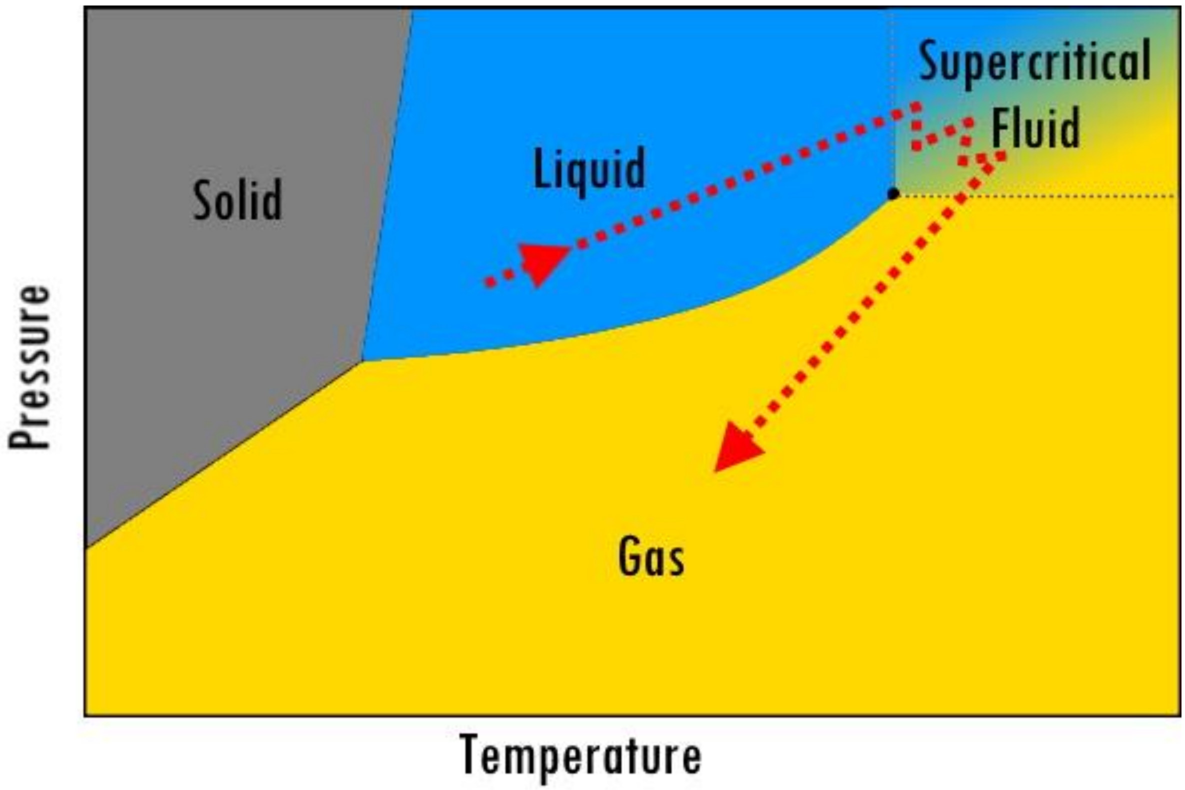

Figure 4.1 A generic phase diagram of CO_2 (temperature and pressure axes not to scale) illustrating the path that the supercritical drying pressure vessel takes to dry an aerogel product (red dotted line). The liquid CO_2 initially within the pores of the gel is heated and pressurized until the liquid CO_2 passes the liquid-vapor critical point and enters the supercritical fluid regime (i.e., once the temperature and pressure exceed 31.04 °C and 7380 kPa, respectively). The pressure and temperature are then repeatedly decreased and increased until both can be decreased to below the critical point, whereupon the supercritical CO_2 becomes gaseous CO_2 within the pores of a dried aerogel.

was poured into molds (the sol should set 4 minutes after the catalyst and TMOS solutions are initially mixed) and allowed to age under methanol atmosphere for 24 hours. After aging, solvent exchange was initiated; the molds were fully submerged in a methanol bath, with the bath being replaced with new methanol every 24 hours for up to three exchanges. After solvent exchange, the molds were dried over three days via supercritical CO_2 drying in a pressure vessel using the facilities of Aerogel Technologies. The drying process followed the general path traced by the dotted red arrows in Figure 4.1, where the temperature and pressure of the liquid CO_2 within the pores of the gel were increased until both properties were well-past the liquid-vapor critical point of 31.04 °C and 7380 kPa [104]. The vessel was heated until the pressure increased to about 9650 kPa, then roughly 1550 kPa of pressure was slowly released over 10-20 min through a pressure release valve. This was repeated until the temperature reached 50-60 °C without the pressure increasingly significantly with added heat [105]. The vessel was then depressurized to about 3450 kPa over 60 min, then depressurized further to ambient over 20 min. The result was a dried aerogel monolith with embedded particles.

4.1.2: Synthesis of Nanoparticles: Protocol 1

The first protocol for the synthesis of $NaYF_4$:Yb/Er nanoparticles was that of Wang and Liu [80]. A solution of 70.10 mg of sodium chloride, 145.6 mg of yttrium chloride hexahydrate, 41.849 mg of ytterbium chloride hexahydrate, and 4.581 mg of erbium chloride hexahydrate in 9 mL of ethylene glycol and 150 mg of PEI was agitated well in a glass beaker. Another solution of 71.1 mg of ammonium fluoride in 6 mL of ethylene glycol was created, and the fluoride solution was added to the chloride solution and stirred until the ammonium fluoride flakes were fully dissolved. The mixed solution was transferred to an autoclave and was heated at 200 °C for two hours. The nanoparticles were collected via a centrifuge (4000 RPM), washed with an ethanol/water solution (1:1 by volume) three times, and dried under heated vacuum (50 °C) for 24 hours (Figure 4.2a).

4.1.3: Synthesis of Nanoparticles: Protocol 2

The second protocol for the synthesis of $NaYF_4$:Yb/Er nanoparticles was by Li and Zhang [81]. A solution of 156.2 mg of yttrium chloride hexahydrate, 50.3 mg of ytterbium chloride hexahydrate, and 5.5 mg of erbium chloride in 3 mL of oleic acid and 17 mL of octodecene was created in a glass flask. The flask was heated under argon atmosphere until homogeneous, then cooled to room temperature. Another solution of 10 mg of sodium hydroxide and 148 mg of ammonium fluoride in 10 mL of methanol was created, then slowed added to the flask. The mixed solution was stirred for approximately 30 minutes until all fluoride flakes had dissolved. The solution was slowly heated to evaporate the methanol, degassed at 100 °C for 10 minutes, then held at 300 °C for one hour under argon atmosphere. The solution was cooled to room temperature. Adding ethanol to the solution created nanocrystal precipitates, which were centrifu ged out at 4000 RPM and washed with an ethanol/water solution (1:1 by volume) three times (Figure 4.2b).

4.1.4: Synthesis of Nanoparticles: Protocol 3

The third protocol was by Lei et al. [89]. Unlike the first two protocols, this protocol was for the synthesis of $NaBiF_4$:Yb/Er nanoparticles. A solution of 378.36 mg of bismuth nitrate pentahydrate, 89.83 mg of ytterbium nitrate pentahydrate, 8.87 mg of erbium nitrate pentahydrate, and 169.98 mg of sodium nitrate pentahydrate in 10 mL of ethylene glycol was created. Another solution of 148.15 mg of ammonium fluoride in 25 mL of ethylene glycol was created. The fluoride solution was vigorously stirred into the nitrate solution. The time stirred v aried depending on the desired size of the nanoparticles (according to Lei et al., 5 s for smaller particles with

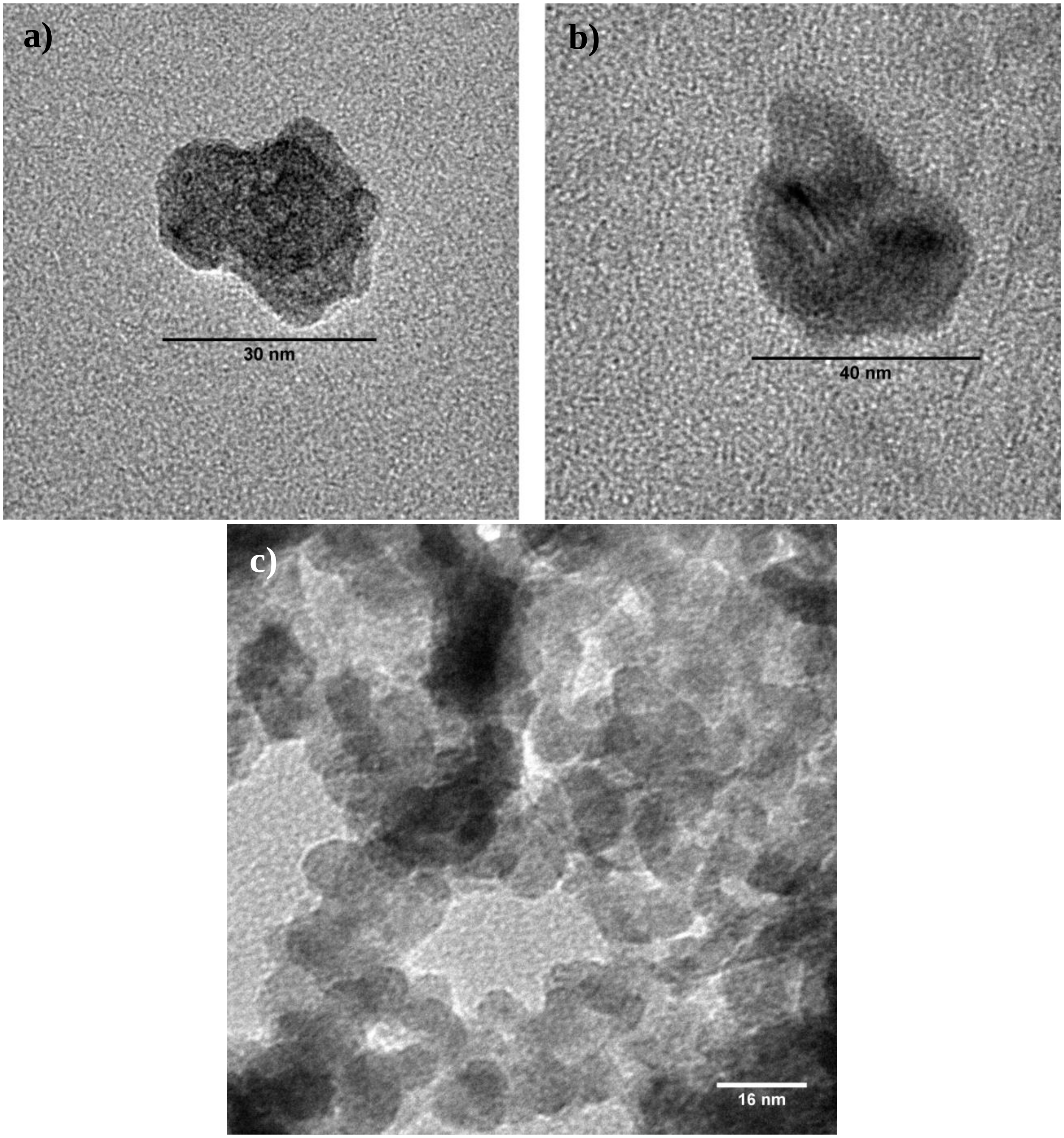

Figure 4.2 TEM of synthesized nanoparticles. a) $NaYF_4$:Yb/Er nanoparticles synthesized via Wang and Liu; scale bar indicates 30 nm. Nanoparticles ranged in diameter from 15 nm (often in large clusters ~100 nm across) to 30 nm (usually individual particles). b) $NaYF_4$:Yb/Er nanoparticles synthesized via Li and Zhang; scale bare indicates 30 nm. Nanoparticles ranged in diameter from 10 nm (often in very large clusters on the order of 100 nm to 1 μm) to 40 nm (usually individual particles). c) $NaBiF_4$:Yb/Er nanoparticles synthesized via Lei et al.; scale bar indicates 16 nm. Nanoparticles ranged in diameter from 20 nm (when stirring for 5s) to 480 nm (when stirring for 60 s).

diameters ~20-50 nm, and 60 s for larger particles with diameters ~480 nm). The particles were centrifuged out at 4000 RPM, washed three times with anhydrous ethanol, and dried at room temperature in a fume hood over 24 hours (Figure 4.2c).

4.2: Results

After synthesizing the nanoparticles by following the three protocols, the fluorescence of the particles was tested. The particles were exposed to 980 nm laser light from two different lasers. The first was a 25 mW laser purchased from Roithner Lasertechnik, SHP980-25. The second was a 500 mW laser purchased from BigLasers.com, IRX7. The particles were exposed to the lasers when the particles were in dry powder form, when the particles were in solution (within both water and ethanol), and when the particles were embedded within dried silica aerogel monoliths at concentrations of at least 0.01 mg/mL and up to 1 mg/mL.

4.2.1: Protocols 1 and 2: Yttrium Nanoparticles

The synthesis of the $NaYF_4$:Yb/Er nanoparticles using both formulations (Wang and Liu; Li and Zhang) was unsuccessful in producing particles that could detectably fluoresce when embedded within silica monoliths. Both formulations took a considerable length of time to complete (several hours of exposure to high heat, followed by at least several hours of drying/cooling to ambient temperature and pressure), and both produced small quantities of nanoparticles. Li and Zhang in particular required the reagents to be heated to many specific temperatures for varying lengths of time, increasing the complexity of the procedure and increasing the likelihood of errors. Initial analysis under an optical microscope revealed particles on the order of several micrometers, but TEM analysis (Fig. 4.2a, 4.2b) showed that both formulations were able to produce particles on the nanoscale (~10-40 nm in diameter), and that the larger particles were likely clumps of nanoparticles. When dry, the nanoparticles exhibit weak fluorescence when exposed to sufficiently intense infrared laser light (500 mW focused through +25.4 mm FL lens), but when put in 1 mg/mL solutions or when embedded in dried monoliths, neither formulation exhibited detectable fluorescence.

4.2.2: Protocol 3: Bismuth Nanoparticles

Lei et al. documented a formulation for the synthesis of $NaBiF_4$:Yb/Er nanoparticles, replacing the yttrium for bismuth. The relatively simple protocol was able to produce large quantities of nanoparticles of tunable size. The bismuth particles visibly fluoresced at lower power densities (25 mW focused through +25.4 mm FL lens), in contrast to the yttrium particles. However, these also did not detectably fluoresce when in 0.01 mg/mL solutions or 0.1 mg/mL solutions or when embedded in monoliths, and they exhibited detectable fluorescence only when in dry powder form at high concentrations.

4.3: Monoliths with Embedded Microparticles

The ability to synthesize nanoparticles in-house was desired due to the high costs of purchasing nanoparticles from other providers. However, all three followed protocols were unable to produce particles that could fluoresce when embedded in silica aerogel monoliths. As such, particles had to be purchased. Due to the aforementioned high cost of purchasing nanoparticles, $NaYF_4$:Yb/Er microparticles were purchased from Sigma-Aldrich instead (part number 756555-25G). These particles were able to fluoresce both when in dry powder form and when embedded within monoliths.

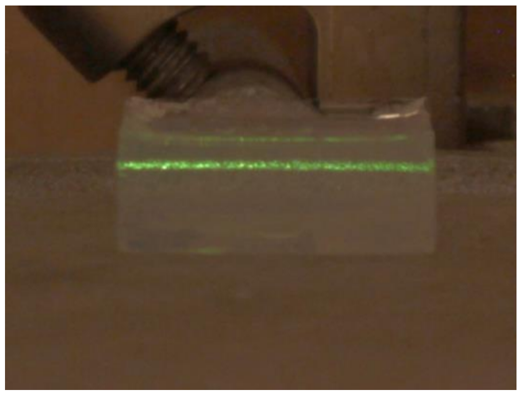

Figure 4.3 A silica monolith (25 mm across) with embedded $NaYF_4$:Yb/Er microparticles that absorb 980 nm infrared light and emit mostly 540 nm green light, shown here illuminated with an unfocused 25 mW laser.

As seen in Figure 4.3, even without focusing the 25 mW laser, the microparticles were able to fluoresce brightly enough to be visible to the naked eye. However, a line of fluorescence was not sufficient for probing singular points within the monolith, for that goal, a smaller voxel with an aspect ratio closer to 1:1 was desired. As such, preparations began for the development of a system where the strain at any given point within a monolith could be determined through optical scanning.

Chapter 5: Optical Scanning System for Volumetric Strain Mapping in Aerogel Monoliths

Before any *in situ* experiments were performed, a technique was formulated based on *ex situ* experiments by observing how an already-dried aerogel monolith was affected by external strain. *Ex situ* strain experiments would demonstrate the viability of the strain mapping technique and the limitations of its eventual utilization for *in situ* measurements. The final set up of the equipment used is shown in Figure 5.1, with previous set ups and configurations detailed below and in Chapter 6.

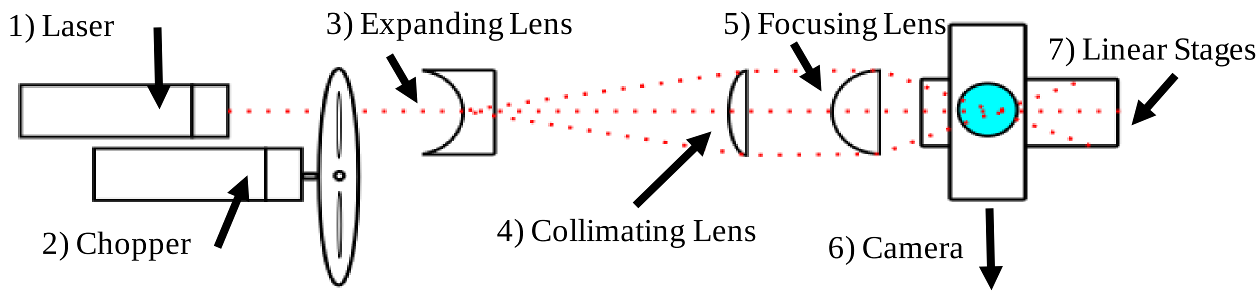

Figure 5.1 Schematic of equipment for the scanning system, with relative placements of the 1) 980 nm laser, 2) mechanical chopper, 3-5) lens configuration, 6) camera, and 7) linear stages.

5.1: Lens Configuration

Early experiments used a +300 mm FL spherical focusing lens without a beam expander. As described in Chapter 6.1.1, this was insufficient for probing singular voxels, as the particles fluoresced throughout the path of the beam as it travelled through the monolith; low beam divergence from the long focal length lens resulted in low excitation contrast near the focal point, thus the entirety of the excited beam path was visible. An alternative configuration using crossed beams was similarly insufficient: a 50-50 beam splitter and mirrors were used to split the laser beam and cross them together within the monolith. Both beams still triggered visible fluorescence throughout their paths, with the fluorescence at the intersection of the beams appearing to be only linearly increasing instead of quadratically increasing (emission intensity scales as a power of the excitation power, where the power is equal to the number of photons required for emission [79]; thus, because upconversion requires the absorption of two photons, upconversion should be a quadratic process).

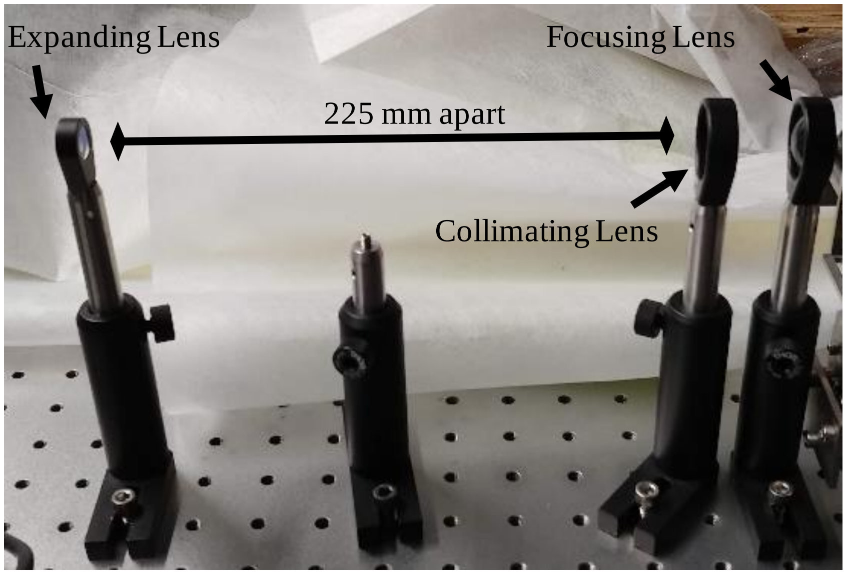

Figure 5.2 Lens configuration; the expanding lens (-25 mm FL) and the collimating lens (+250 mm FL) must be exactly 225 mm separated for the beam expander to have a magnifying power MP = 10. The collimating lens and the aspheric focusing lens (+25.4 mm FL) are an arbitrary distance separated.

To decrease the size of the focal spot such that the fluorescence of the upconverting particles would be a small voxel rather than a line of fluorescence, a beam expander was utilized to decrease the size of the waist of the beam. The IR laser beam passed through a beam expander with a magnifying power MP = 10 before being focused by an aspheric lens (FL = +25.4 mm) (Fig. 5.2). The diameter of the beam before expansion was 2.5 mm, so with a beam expander of MP = 10, the expanded diameter was 25 mm, very near to the maximum beam diameter that could still be focused by the aspheric lens (diameter 25.4 mm). Both the beam expander and the aspheric lens tightened the focus of the beam and decreased the size of the illuminated voxel to a length of ~2.5 mm and a waist radius of approximately 0.15 mm, as described in Chapters 6.1.2 and 6.1.3. For the beam expander to work, the expanding lens and the collimating lens must be separated by a distance equal to the sum of the focal lengths of the component lenses. If the beam expander component lenses are properly aligned and positioned, the distance between the collimating lens and the focusing lens is arbitrary, as a collimated beam should have limited divergence and should not disperse with distance. To produce a small voxel with low aspect ratio, a focusing lens with short focal length was used (FL = +25.4 mm).

5.2: Mechanical Chopper: Decreasing Voxel Aspect Ratio

A mechanical chopper was added to the beam path (before the beam expander) to eliminate photon saturation and decrease the size and aspect ratio of the excited voxel (Fig. 5.3). Photon saturation allows for larger regions than the voxel to fluoresce, increasing the size of the excited region [78,79]. The mechanical chopper consisted of discs of aluminum with apertures cut out of them that were mounted to a DC motor that could rotate at revolutions ranging from 5,000 RPM to 20,000 RPM. The laser was modulated to decrease the number of photons that any given volume of the monolith would be exposed to over a given length of time; due to the limitations of the laser used in these experiments, true pulsing of the laser through electronic means was not viable, as the laser was unstable when pulsed at lower than 50% duty cycle. For experimentation, the motor was set to rotate at 6000 RPM, and the discs were aligned such that the effective duty cycle of the laser was 1% (50 μs "on", 4950 μs "off"). This duty cycle was based on the experiments of Hodak et al. [78], where they electronically pulsed their laser at 1% duty cycle to induce fluorescence in their upconverting nanoparticles.

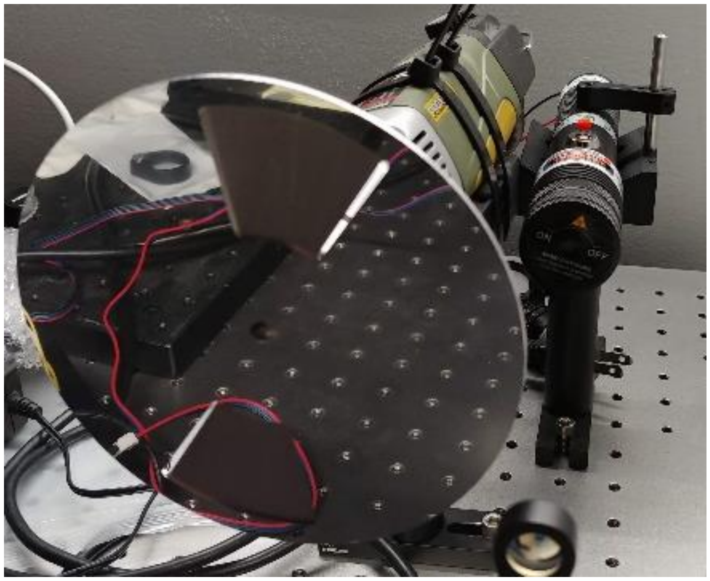

Figure 5.3 Mechanical chopper with 500 mW laser, with 25.4 mm between the set holes of the optical table. During experimentation, the motor rotated at 6000 RPM, and the laser beam passed through the slits in the aluminum discs, creating an effect similar to "pulsing" the laser at 1% duty cycle.

5.3: Camera: Capturing Intensity of Emissions

Early experiments used a Canon EOS REBEL T5i camera with aperture set to f/3.5. When capturing the fluorescence of microparticles illuminated by the weak 25 mW laser, the intensity of the fluorescence was faint enough that a high gain (ISO-1600) and long exposure time (2 s) needed to be used to obtain clear images. These factors increased the noise of the camera, such that analysis of the images was often unable to produce sound conclusions (see Chapter 6.3.1).

After the Canon was deemed too ineffective due to noise, a CMOS camera (Basler ace acA2040-90um) was used to capture images of the fluorescence. Because the primary wavelength of emission of the upconverting particles was 540 nm, the camera was outfitted with a bandpass filter with a range of 540 nm ±15 nm. The camera was also outfitted with an IR filter with an optical density of OD 8 at wavelength 980 nm and at least OD 5 for most other near-IR wavelengths. The camera was connected to both an Arduino Uno and a computer, with the computer running Basler's Pylon Viewer Version 5.2 64 bit. Pylon allowed for the camera to be controlled via a graphic user interface, and the camera was set to automatically take one image every time it received a signal from the Arduino (controlled through MATLAB – Appendix A).

Later experiments utilized another CMOS camera, a FLIR Blackfly S BFS-U3-51S5M-C (see Chapter 6.3.1), with another bandpass filter with a range of 335 nm to 610 nm. The FLIR was less noisy than the Basler, with higher EMVA quantum efficiency (72% vs 62.1%), lower dark noise (2.31 e^- vs 13.8 e^-), and comparable signal-to-noise ratio (40.06 dB vs 40.8 dB) [106,107]. This new camera was a contributing factor in reducing the noise floor to 0.1%. A low noise floor was crucial in obtaining a high signal-to-noise ratio, as the signal was anticipated to be less than 1% due to the range of applied stresses that were accessible in these silica aerogel monoliths without yielding.

5.4: Linear Translation Stages: Scanning Within the Monolith

To perform three dimensional interrogations of the monolith volume, it was necessary to scan the illuminated voxel throughout the monolith. Here we chose to the move the sample while keeping the optical system and illumination spot fixed in space. The position of the aerogel monolith was manipulated through Thorlabs' PT3-Z8 25 mm three-axis motorized translation stage. These stages enabled precise localization of the interrogation beam within the monolith as well as scanning capabilities in three dimensions for volumetric intensity mapping. The stages were positioned such that moving the stages in the positive X direction moved the stages closer to the camera, moving the stages in the positive Y direction moved the stages further from the laser, and moving the stages in the positive Z direction moved the stages up (Fig. 5.4). The stages were controlled via three KDC101 K-Cube brushed DC servo motor controllers, one for each axis. The controllers were in turn commanded by MATLAB scripts (Appendix A.1.1), which utilized DLL files provided freely on the Thorlabs website [108].

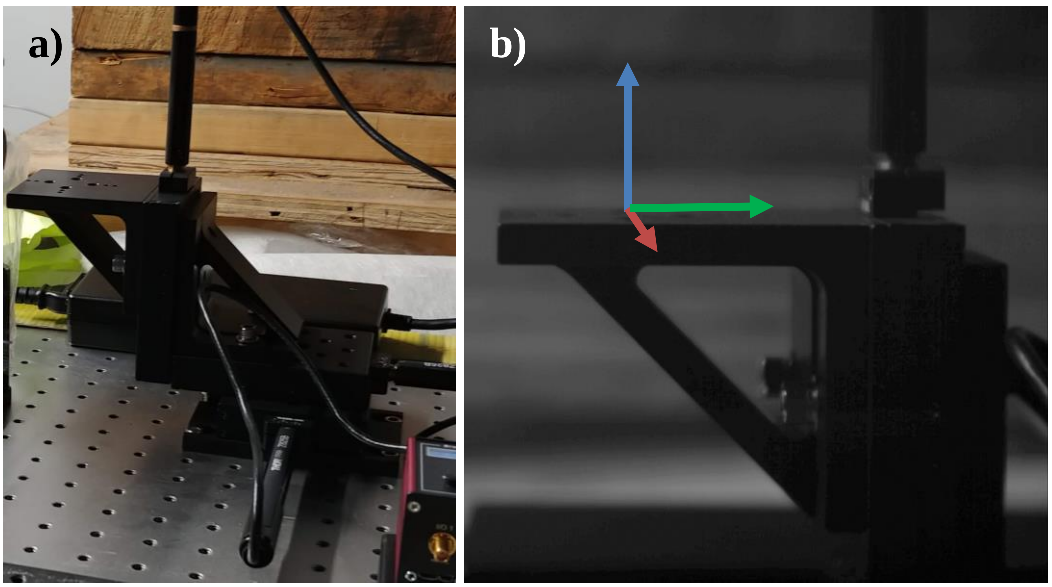

Figure 5.4 Linear translation stages purchased from Thorlabs. a) Relative size of the stages, with 25.4 mm between the set holes of the optical table. b) Each arrow represents one axis of motion, with X (red arrow), Y (green arrow), and Z (blue arrow).

An alternative method of scanning was considered but ultimately dismissed for *ex situ* experiments: mirrors controlled by galvanometers. The linear stages allowed for interrogation throughout the monolith by moving the monolith itself; the voxel (i.e., at the focal point of the focusing lens) did not move through the monolith, but rather the monolith moved around the voxel. With galvanometers, the laser beam would be reflected off mirrors and redirected to precise locations within the monolith. As the galvanometers rotated, the voxel would truly move throughout the monolith. While the consideration of galvanometers was intriguing for *in situ* experiments (especially when paired with beam sheets), the use of the beam expander and short focal length aspheric lens made moving the voxel unviable, as interrogation would not be possible along the axis aligned with the laser (i.e., the Y axis of the linear stages).

Chapter 6:

Voxel Illumination in Silica Aerogel Nanocomposites

The ultimate goal of this research was to observe the strain of a drying aerogel monolith *in situ* using the intensity of emissions calibrated by the initial particle density of fluorescent particles. To that end, observing upconverting aerogel nanocomposite monoliths under strain *ex situ* (i.e., after it has already dried) was used to vet the viability of the optical strain mapping technique and determine whether or not it is possible to observe a change in strain using such an approach. Thus, a series of experiments were conducted in which aerogel monoliths embedded with upconverting particles (as described in Chapter 4) were exposed to focused infrared laser light, while applying uniaxial compressive loads, and monitored with a camera to measure strain-induced changes in voxel brightness. Once it could be demonstrated that strain within such monoliths could be accurately determined *ex situ* through optical means, plans for *in situ* experimentation would follow.

6.1: From Line Illumination to Voxel Illumination

Early experimentation started with a 25 mW laser and commercial fluorescent $NaYF_4$:Yb/Er microparticles (average diameter 1-5 μm) purchased from Sigma-Aldrich (part number 756555). The weak laser was sufficient for triggering fluorescence in the microparticles both in solution and embedded in a monolith, even without a focusing lens, resulting in a visibly observable line of green illumination throughout the medium. A lens was then added to focus the laser into a voxel that could serve as an optical probe for interrogating the strain state of the monolith at a specific point. However, it quickly became apparent that the equipment and materials used were not sufficient for producing a voxel with a low-enough aspect ratio and well-defined shape, required for robust analysis of the strain state within a monolith. Thus, multiple steps were taken, such as utilizing nanoparticles and an aspheric lens, to decrease the voxel size and aspect ratio and to control voxel shape to the point where voxel illumination could serve as a viable tool for probing strain states.

6.1.1: Microparticles, Non-Scientific Camera, Low-Power Laser, and Long Focal Point Lens

Initial experiments utilized a 25 mW infrared laser with wavelength of 980 nm (purchased from Roithner Lasertechnik, SHP980-25). The laser was focused through a plano-convex lens with a focal length of 30 cm. A representative image of a monolith and the resulting green fluorescence can be seen in Figure 6.1. The monolith discs were 25 mm in diameter and 10 mm in height, and as can be seen in Figure 6.1b, the laser triggered fluorescence throughout the full diameter of the monolith and along the full path of the beam. The camera used for these early experiments (the Canon camera, described in Chapter 5), was set to ISO-1600, f/3.5, and 2 s exposure time. The relatively long exposure time and small f-number (i.e., large aperture) allowed for more light to be captured by the camera, and the high ISO value provided high gain, which amplified the signal at the expense of increased noise.

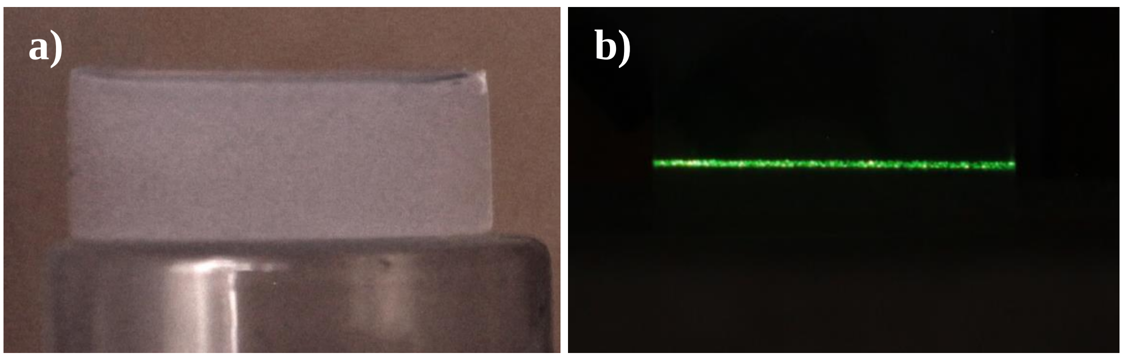

Figure 6.1 a) A silica aerogel monolith (25 mm across) with embedded $NaYF_4$:Yb/Er microparticles (0.01 mg/mL); b) A monolith exposed to 980 nm IR laser (25 mW), focused through a 30 cm FL lens, with resulting fluorescence spanning the diameter of the monolith (25 mm)

To quantify the fluorescence, images of the fluorescence were analyzed using a MATLAB image analysis script (Appendix A.1.2). The camera used for these early experiments was a full-color camera, so the "green" component of the RGB image was isolated for analysis (since most of the emitted light was in the green spectrum). All pixel values below a certain threshold were converted to "not a number" values (NaN) such that those pixel values would be ignored when determining the intensity of the beam's fluorescence. The threshold was determined based on the intensity of the fluorescence; the camera settings were such that the intensity usually peaked at around 220 (out of a maximum of 255), so the threshold was set to roughly half of that peak intensity value.

Figure 6.2 shows the analysis of a representative image. According to the Beer-Lambert law (Equation 6.1), light will attenuate as it passes through a physical medium according to an exponential function:

$$\frac{dI(x)}{dx} = -\mu I(x)$$

$$I(x) = I_0 e^{-\mu x} \tag{6.1}$$

where I is the intensity, I_0 is the initial intensity, μ is the coefficient of absorption of the medium (defined as $\mu = 2\omega n/c$, where ω is the frequency of the beam, n is the index of refraction of the medium, and c is the speed of light in a vacuum), and x is the depth through the medium.

The Beer-Lambert law can be modified to describe multiphoton absorption, where it is known that the absorption is nonlinearly proportional to excitation. Thus, Equation 6.2 describes how multiphoton absorption attenuates according to a power law function:

$$\frac{dI(x)}{dx} = -\beta[I(x)]^a$$

$$I(x) = \left[\frac{(1-a)(I_0)^{a-1}}{1-a-\beta x(I_0)^{a-1}}\right]^{\frac{1}{a-1}} \tag{6.2}$$

where β is the bulk multiphoton optical density and a represents the order of the process. In upconversion fluorescence, the intensity of emissions (and thus absorption) is proportional to the square of excitation (i.e., $a = 2$), thus Beer-Lambert becomes:

$$I(x) = \frac{I_0}{1+\beta x I_0} \tag{6.3}$$

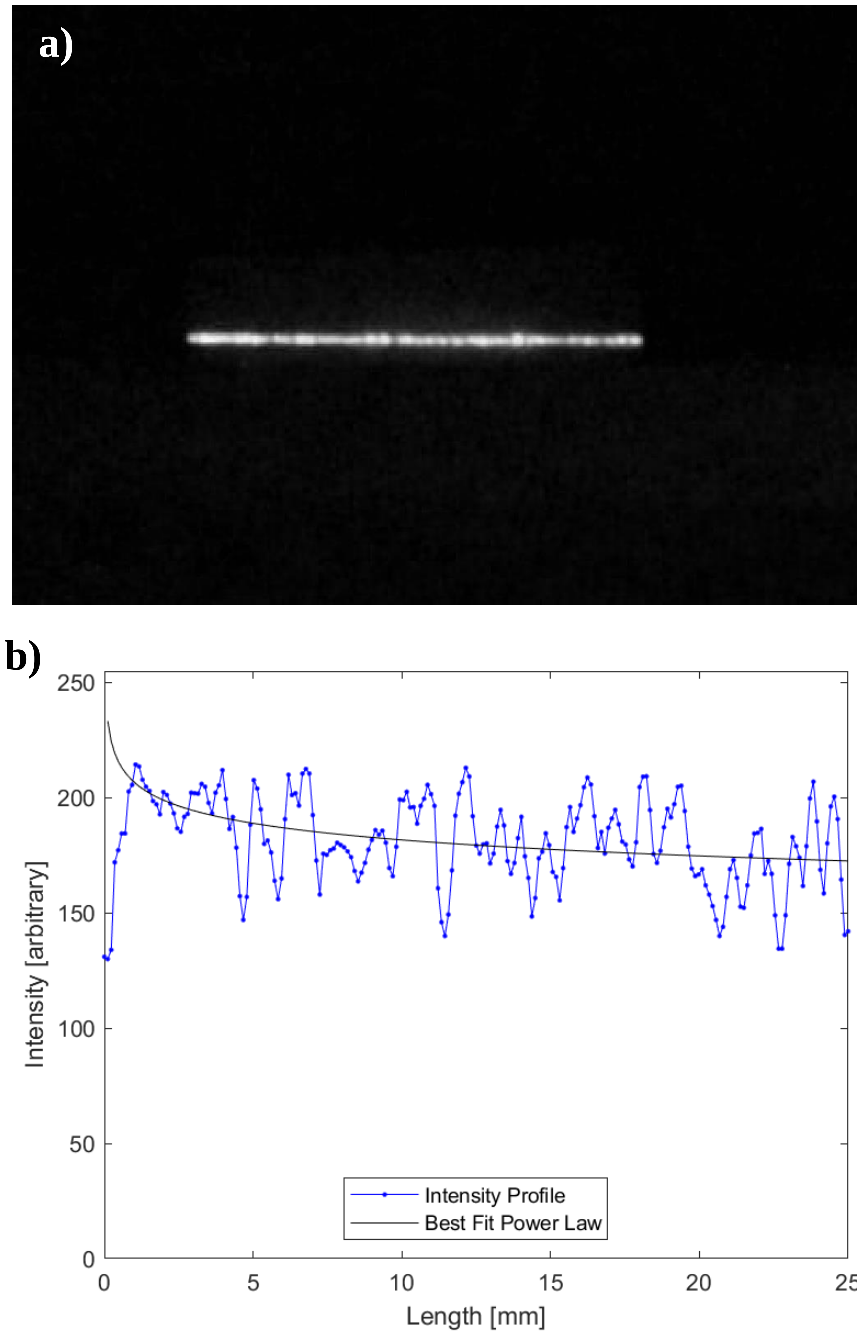

Figure 6.2 a) "Green" component of image of fluorescence through silica aerogel, 25 mm diameter. The fluorescence is fragmented, with brighter and fainter regions, presumably due to microparticle clustering. b) The intensity profile of the fluorescence, with best fit power law $y = 206.8131x^{-0.0562}$ (R^2 = 0.1618, RMSE = 0.0955).

As can be seen in Figure 6.2b, the intensity profile of the line of fluorescence cannot be fit to a power law. The equation fit was $y = Ax^b$, where A = 206.8131 and b = -0.0562. Due to the high variability of the data (R^2 = 0.1618, RMSE = 0.0955), the fit is very poor, such that strong conclusions cannot be made. The attenuation through the monolith was low, and the behavior of the decay cannot be discerned from the data analysis.

One source of image noise was likely the clustering of the microparticles (Figure 6.2a). Additional sources of image noise likely were due to camera settings. As noted, the camera was set to high aperture, long exposure, and high gain. Due to the low power of the laser (25 mW), the emitted fluorescence was of low intensity, requiring a longer exposure time and higher gain for the camera to capture it. The long exposure time and high gain increased noise, but both were required to measure the fluorescence. In addition, the lens used had a long focal length and low aperture, which meant that the camera could not properly focus on the monolith when it was too close, requiring the camera to be positioned roughly 1 meter away from the monolith. This decreased the size of the region of interest of the image such that the actual fluorescence accounted for fewer than 250 pixels across the image.

6.1.2: Decreasing Voxel Size: Stronger Laser, Beam Expander, and Short Focal Point Lens

To address some of the issues presented discussed previously, such as line of fluorescence caused by the long focal point lens, two steps were taken. The first was to utilize a beam expander. Focusing a small-diameter beam with a long focal length lens results in a relatively large waist, defined as the radius of the focused beam at the focal point (Figure 6.3). To narrow the waist, one can either increase the diameter of the beam or decrease the focal length of the focusing lens. Since the goal was to focus a laser to a small point to probe the strain state of a monolith while it dries, a narrower waist was desired, so both increasing the beam diameter and decreasing the focal length were implemented. To increase the beam diameter, a beam expander was designed to increase the diameter by a factor of 10 (i.e., magnifying power MP = 10). The equations below were used both in designing the beam expander and in calculating the waist:

$$MP = \frac{D_o}{D_i} \qquad [6.4]$$

where D_i is the diameter of the beam before expansion, D_o is the diameter of the beam after expansion, and MP is the magnifying power of the beam expander;

$$\tan\theta = \frac{D_o}{2f} \qquad [6.5]$$

where f is the focal length of the focusing lens and θ is the angle of the beam after focusing;

$$PD = \frac{P}{\pi(w_f)^2} \qquad [6.6]$$

where P is the power of the beam, w_f is the waist of the beam, and PD is the power density at the waist;

$$w_f = \frac{2\lambda f}{\pi D_o} \qquad [6.7]$$

where λ is the wavelength of the beam.

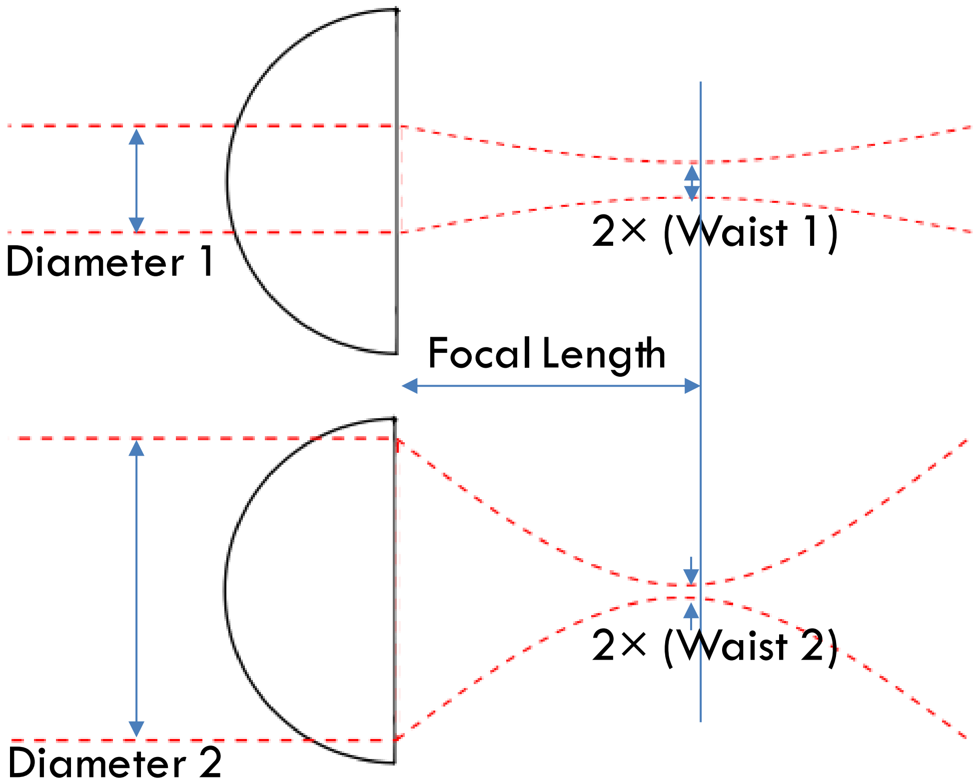

Figure 6.3 Expanding the beam diameter decreases the waist, according to Equation 6.7. Thus, the beam expander is required to increase the diameter of the beam and decrease the waist, sharpening the focus of the beam and decreasing the size of the voxel.

As seen in Equation 6.7, using a focusing lens with a smaller focal length would decrease the waist. Thus, the focusing lens was changed to a 25.4 mm FL lens. As seen in Figure 6.4a, the combination of the beam expander and the shorter focal point lens allowed for a smaller region of fluorescence when compared to the line of fluorescence that spanned the full diameter of the monolith. However, the low power of the laser still resulted in low intensity of fluorescence. Thus, the second step made to alleviate the issues noted above was to acquire a stronger laser. Such a

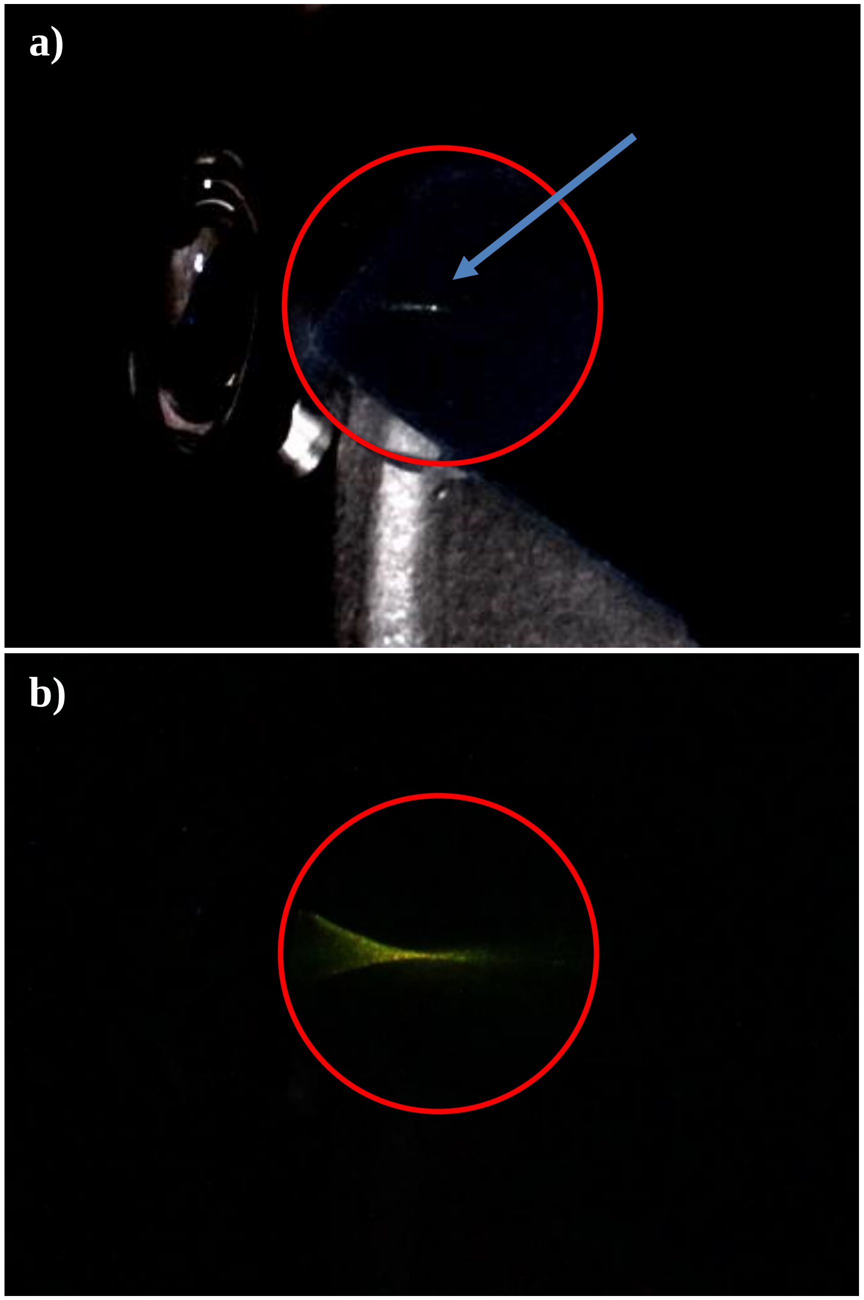

Figure 6.4 Two images of the same silica monolith with 0.01 mg/mL of $NaYF_4$:Yb/Er microparticles, taken with the same camera from the same position. a) Fluorescence from the 25 mW laser, ISO-1600, f/3.5, and 2 s exposure. The red circle shows the location of the monolith (25 mm diameter) with a blue arrow pointing at the fluorescence in the center of the monolith. b) Fluorescence from the 500 mW laser, ISO-200, f/3.5, and 0.5 s exposure. The red circle shows the location of the monolith (25 mm diameter) with the fluorescence in the center of the monolith.

laser would result in higher intensity of fluorescence, allowing for shorter exposure times and lower gain. A 500 mW laser was purchased from BigLasers.com, part number IRX7. A comparison of the difference between the 25 mW laser and the 500 mW laser is shown in Figure 6.4. As can be seen, the fluorescence has a much larger region of fluorescence with the 500 mW laser compared to the 25 mW laser. The intensity was bright enough that the gain and exposure time could both be dropped by a factor of 4 (from ISO-1600 to ISO-200, and from 2 s exposure to 0.5 s exposure).

However, while the beam expander, the new focusing lens, and the stronger laser alleviated the issues of the line of fluorescence, other issues remained. Suspected microparticle clustering that manifested as local bright spots was still observed. Additionally, instead of a long line of fluorescence or a small voxel of illumination, using the 500 mW laser with the microparticles resulted in a cone with a stretched focal spot (Figure 6.4b). With these issues, it became unclear exactly how to measure the intensity of the resulting "voxel," since the "voxel" did not have clear boundaries. The next goals were to reduce particle clustering and to reduce the size and aspect ratio of the illuminated voxel. The utilization of nanoparticles was believed to address both of these problems.

6.1.3: Further Decreasing Voxel Size: Nanoparticles, Aspheric Lens, and Chopper

It was hypothesized that both the observed particle clustering and the voxel size were related to the size of the fluorescent particles. The heavy microparticles would settle and agglomerate during production of the aerogel composites, leading to the nonuniform fluorescence pattern; nanoparticles are light enough that they can stay in suspension longer, resulting in more uniform distribution than the heavier microparticles. Additionally, larger particles compose a higher volume fraction of the composite monoliths, resulting in emissions at lower power densities. Increasing the diameter of a particle by a certain factor increases the volume of the particle by the cube of that factor, so with nanoparticles, which can have diameters two or three orders of magnitude smaller than microparticles, only the regions closest to the focal point would fluoresce. These hypotheses formed the basis for pursuing the use of nanoparticles.

As documented in Chapter 4, in-house attempts to synthesize nanoparticles were not successful in producing aerogel nanocomposites that could visibly fluoresce, even when exposed to the 500 mW laser. As such, $NaYF_4$:Yb/Er nanoparticles were purchased from Sigma-Aldrich (part number 900556). These nanoparticles were 20 nm in diameter and absorbed 980 nm infrared light to emit 540 nm green light. A representative image of a silica aerogel monolith embedded with these nanoparticles can be seen in Figure 6.5a. When compared to the fluorescence of the microparticles, the cone of fluorescence from the nanoparticles is much less bright, while the fluorescence from the focal point is stretched out into a short line roughly 5 mm long.

Though the nanoparticles provided a notable improvement in voxel shape over the microparticles, the long aspect ratio of the voxel was higher than desired. It became clear that spherical aberrations caused by using spherical lenses were a significant problem that needed to be addressed, so an aspheric lens was acquired. As seen in Figure 6.5b, the fluorescence achieved with the use of an aspheric lens became much more localized, resulting in a voxel measuring roughly 2.5 mm in length and a waist of 0.15 mm, with the shape of the voxel changing to an approximate bicone centered around the focal point of the laser.

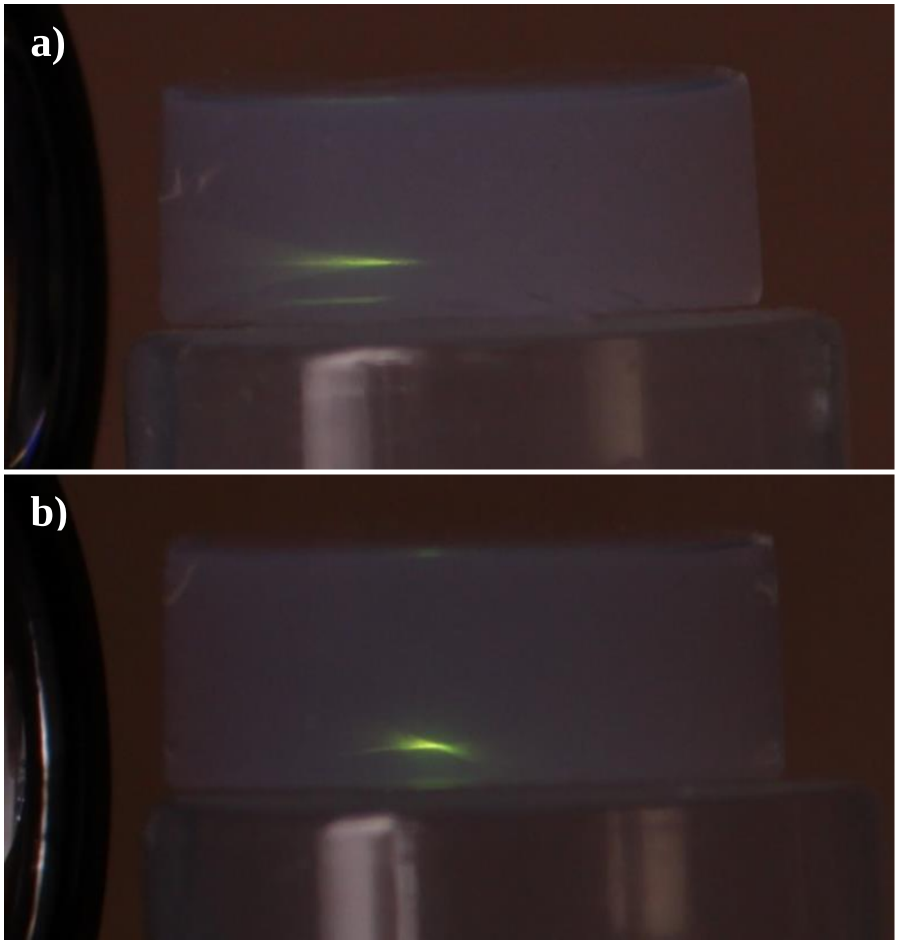

Figure 6.5 A monolith (25 mm diameter) embedded with nanoparticles at 0.01 mg/mL, illuminated with 500 mW laser. a) With a spherical lens the voxel is ~5 mm long. b) With an aspheric lens the voxel is ~2.5 mm long.

While this was a definite improvement, the aspect ratio of the voxel was not yet close enough to 1:1, and it was believed that the aspect ratio could be decreased further. Hodak et al. 2016 demonstrated a method of decreasing the voxel size and aspect ratio through pulsing their laser [78], so a similar method was applied here. Due to limitations of the laser used in these experiments, true pulsing of the laser through electronic means was not viable, as the laser output would suddenly drop to 0 W when electronically pulsed at greater than 50% duty cycle. Instead, the mechanical chopper described in Chapter 5 was used; the motor spun at 6000 RPM fitted with rotating aluminum discs with apertures aligned such that the effective duty cycle of the laser was 1% (50 μs on, 4950 μs off). Figure 6.6 shows a representative image of the voxel with and without chopper-based pulsing of the laser. The length of the voxel with pulsing is much shorter, at about 1 mm instead of 2.5 mm, and the aspect ratio is roughly 1.5:1. However, the voxel was so faint that the camera required high gain (ISO-3200) and long exposure time (4 s) to capture the fluorescence. Monoliths containing higher concentrations of nanoparticles should in principle exhibit higher intensity fluorescence, but the quantity of commercial nanoparticles that would have been required was cost-prohibitive. As such, experiments involving the chopper were not pursued further.

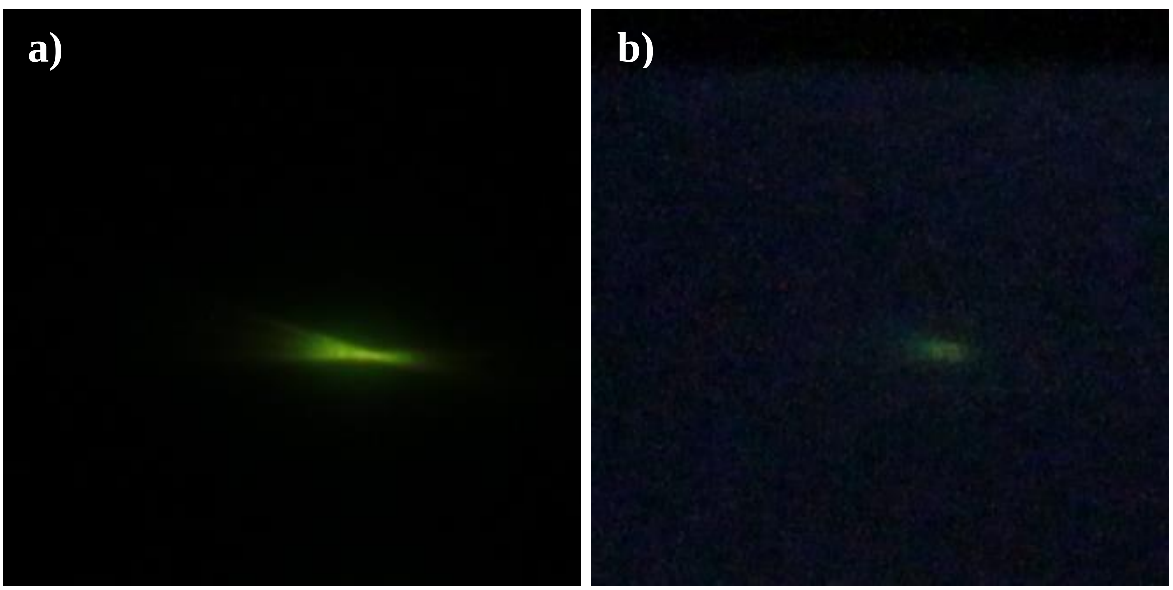

Figure 6.6 Fluorescence of nanoparticles (0.01 mg/mL) from 500 mW laser. a) Without pulsing, the voxel length is ~2.5 mm (ISO-200, f/3.5, and 0.5 s exposure). b) With pulsing, the voxel length is ~1mm (ISO-3200, f/3.5, and 4 s exposure).

6.2: Compression Tests, Strain and Emission, and Volumetric Scanning Protocol

With the use of the 25.4 mm FL aspheric lens, the voxel size was decreased to roughly 2.5 mm in length. At this point, the voxel was small enough to begin experiments with nanocomposite monoliths under strain and scanning the voxel throughout the monolith in an effort to spatially map the strain within the monolith. Both were necessary steps, as they were key features of the proposed optical technique and thus needed to be evaluated; if it was possible to observe a change in the fluorescence *ex situ* corresponding to a known strain imposed upon a monolith, and if it was possible to determine strain values at any given location within the monolith, then the proposed technique could then be applied to *in situ* strain mapping of gels during supercritical drying.

6.2.1: Brightness of 0D Voxels as a Function of Strain: Straining a Stationary Monolith

To characterize the strain at a single position in the monolith, a silica aerogel monolith embedded with upconverting nanoparticles was positioned on linear stages as seen in Figure 6.14. The stages were kept stationary for these experiments. The monolith was sanded flat on both the top and bottom surfaces with fine-grit sandpaper, and two platens machined from acrylic were placed both over and under the monolith (Figure 6.14). Both of these actions were taken in an effort to create a uniform surface on both the top and bottom of the monolith, such that any optical effects experienced by the laser near the top and bottom surfaces of the monolith (such as reflection) would be as similar as possible.

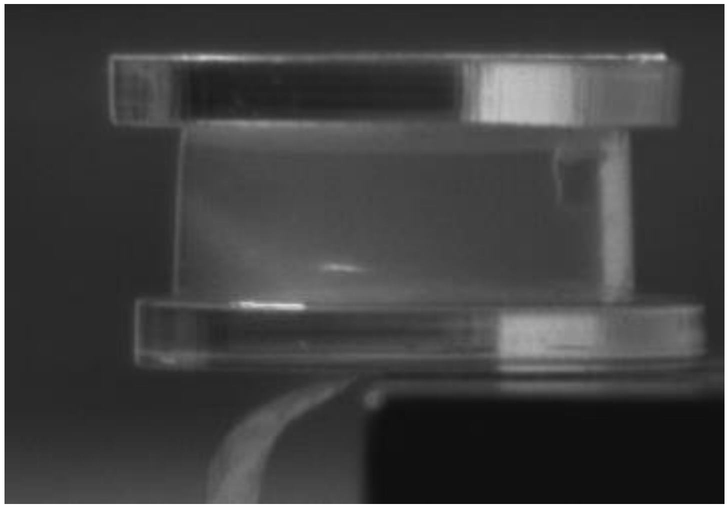

Figure 6.7 A monolith (25 mm diameter) between two platens, positioned on the translation stages. The platens serve to make the top and bottom surfaces as uniform as possible, while the translation stages can move the monolith such that the voxel (seen in the center of the figure) can be positioned throughout the monolith. This image was taken with the monochrome Basler camera with the lights on, while images analyzed for Figure 6.8 were taken in complete darkness, with the only source of visible light from the illuminated voxel.

The monolith was strained by careful manual application of masses to the top platen that weighed 30.83 g, 90.40 g, and 150.20 g, respectively. Accounting for the area of the top surface, those three weights translated into four loads: Load 0 (0.0 kPa), Load 1 (0.73 kPa), Load 2 (2.19 kPa), and Load 3 (3.65 kPa). For this experiment, the laser was warmed up for 45 min prior to image capture by the Basler camera (instead of the Canon camera used in previous experiments). The monolith was held in one position by the linear stages while it was subjected to the four experimental loads, with the camera capturing images recording the fluorescence. The monolith was then moved via the linear stages to a different position 0.5 mm away (though the voxel was kept relatively close to the center of the monolith) and the four loads were again applied. The intensity profiles of 17 positions were calculated via the "boxing" method, described in detail in Chapter 6.3.3 below, then averaged together to calculate the mean trend of fluorescence vs. applied load (Figure 6.8). In Figure 6.8, the fluorescence has a positive correlation with applied load, which matches with initial hypotheses; as the monolith is exposed to higher stresses, the monolith will experience volumetric strain, increasing the local number density of particles and thus increasing the intensity of the fluorescence of the voxel. However, the error bars in Figure 6.8 show that there is enough variability in the data that no strong conclusions can be made from this analysis.

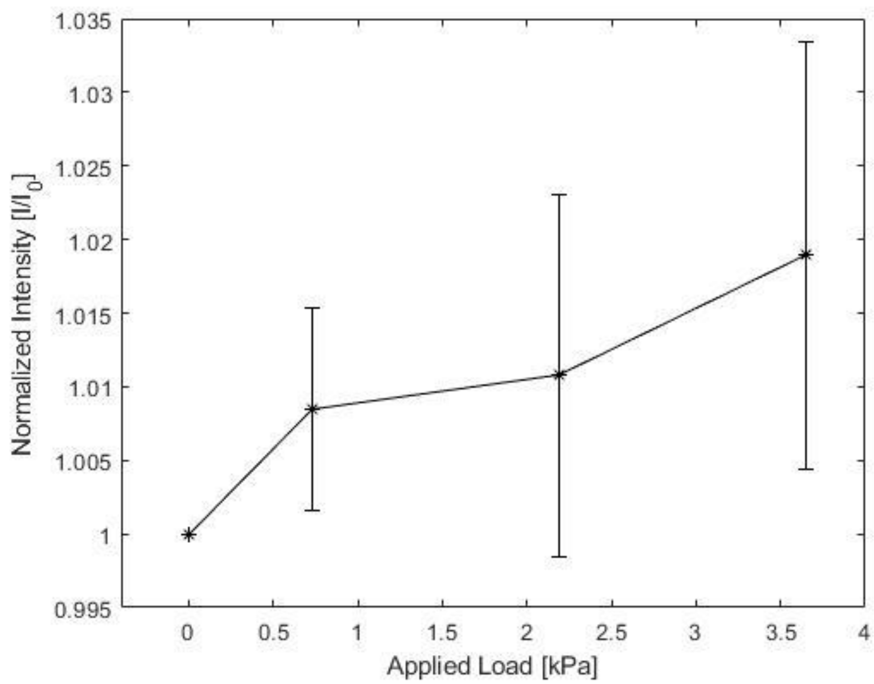

Figure 6.8 Intensity of fluorescence versus applied load, initialized by the intensity of Load 0. The fluorescence seems to increase in intensity with increasing applied loads, matching with hypotheses, but with error bars (standard error, $\frac{\sigma}{\sqrt{n}}$), it can be seen that there is too much variability to make strong conclusive comments.

One source of the variability was from the 17 different positions. As seen in Appendix A.3, some of the positions showed a positive correlation between intensity and load, while others showed a negative correlation. Still other positions showed no clear correlation, increasing in intensity with one load then decreasing with the next. It was hypothesized that this variability was not actually caused by the different positions, but rather by the laser having non-uniform power output over time (discussed in Chapter 6.3.2 below). This led to the acquisition of the laser power meter to track the power fluctuations of the laser in real time, though this experiment has not yet been repeated with said power meter.

Another source of variability was possibly the loading method of manually placing the weights on the monolith. This loading method was crude and rudimentary, with many opportunities to introduce noise; manually placing and removing the weights could shift the monolith's position, thus changing the location of the voxel in between loads. There were plans to improve the loading method, either by automating it or utilizing screws and springs, but those plans were not detailed, and other experiments were prioritized.

6.2.2: 1D Line Scans: Scanning Along One Axis

After the stationary loading experiments demonstrated that the fluorescence within the monolith had high variability based on the spatial position of the voxel, the next experiments focused on mapping the strain throughout the monolith. To start, line scans along one axis were performed. The monolith was placed on the linear stages such that the voxel was initially positioned near the top surface of the monolith. The intensity of the fluorescence was recorded with the Basler camera, then the monolith was moved such that the voxel was further from the top surface (along the Z-axis). This was performed for 100 positions, starting at the top of the monolith and ending near the bottom. The images were analyzed via the "boxing" method described in

Chapter 6.3.3 below. The results can be seen in Figure 6.9. Near the top and bottom surfaces, the fluorescence was generally lower than the fluorescence at the center of the monolith, with the exception of the 10 points at the very top of the monolith. It was hypothesized that this was due to the voxel being too close to the top surface; optical effects like reflection and refraction from the top platen and top surface could artificially increase the fluorescence of those first points. Beyond those points, the fluorescence intensity profile was relatively symmetric, with the fluorescence near the top and bottom being lower than the fluorescence near the center. It was unclear why this was. One possible reason was a combination of the shape of the monolith and settling of the nanoparticles; if the nanoparticles settled during the aging process of production, then the fluorescence should be brighter closer to the bottom of the monolith (i.e., where more nanoparticles would reside), but if the monolith gradually increased in diameter from top to bottom, then the fluorescence should decrease closer to the bottom (as the laser would attenuate more due to traveling through more material). The combination of these two factors could contribute to the shape of the intensity profile.

Subsequent to scanning along one axis, scans along all three axes were performed. The X-axis was defined as the axis aligned with the camera's optical axis, with positive X moving closer to the camera. The Y-axis was defined as the axis aligned with the laser propagation direction, with positive Y moving away from the laser. The Z-axis was the same as in the previous experiment, with positive Z moving up. In this experiment, the monolith was placed on the linear stages, which were controlled such that the voxel started at one position and moved along one axis, with the camera capturing the fluorescence at 100 positions per axis. Along the X-axis, the monolith moved 18 mm closer to the camera, thus moving the voxel in the relative negative X-direction. Along the Y-axis, the monolith moved 13 mm further from the laser, thus moving the voxel in the relative negative Y-direction. Along the Z-axis, the monolith moved 5.5 mm up, thus moving the voxel in the relative negative Z-direction. Those distances were chosen due to the physical constraints of either the monolith (e.g., 18 mm spanned most of the 25 mm diameter of the monolith while avoiding edge effects) or the linear stages (e.g., the short focal length of the 25.4 mm FL focusing lens limited movement along the Y-axis). The results of the experiment can be seen in Figure 6.10.

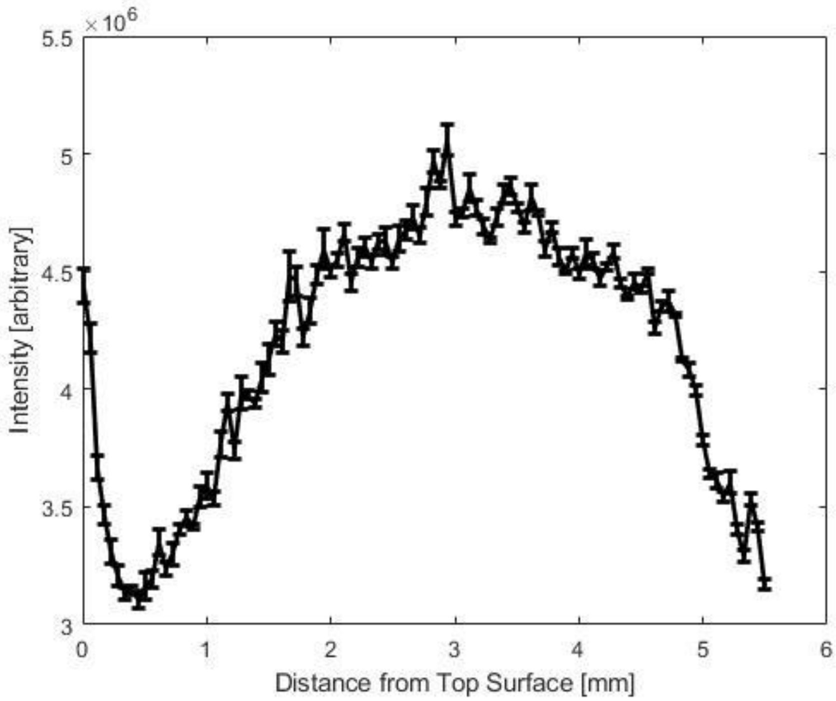

Figure 6.9 Intensity of fluorescence of line scans along the Z-axis, starting at the top of the monolith and ending near the bottom, with error bars (standard error, $\frac{\sigma}{\sqrt{n}}$) derived from four line Z-axis scans at the same X-Y position.

Figure 6.10a shows the intensity of the scans (normalized by the mean intensity of each respective scan) versus the relative position of the voxel. The results of the Z-axis scan were very similar to the results seen in Figure 6.9, demonstrating the repeatability of the experiment. The X-axis scan had predictable results; the position with the greatest intensity was the position that placed the voxel closest to the camera. As the light from the fluorescence had less material to travel through before reaching the camera, there was less attenuation when the voxel was closer to the camera compared to when it was further. Conversely, it is unclear why the Y-axis scan had such an intensity profile. It was assumed that, as the monolith moved further from the laser, the voxel would appear to move closer to the laser, thus resulting in less attenuation and thus higher intensity of fluorescence. That is not what is seen in Figure 6.10a, as the intensity of the scan increases as the voxel moves closer to the laser before dropping again roughly halfway through the scan. One possible reason for this was the geometry of the monolith; because the monolith was disc-shaped, the curvature of the monolith could have refracted some of the light of the fluorescence away from the camera whenever the voxel was too far from the center of the monolith. If this experiment were to be repeated, the disc-shaped monoliths should be replaced with cuboidal/rectangular monoliths, to prevent the curvature of the monolith from affecting the fluorescence captured by the camera.

Figure 6.10b shows a 3D scatter plot of the normalized intensities of the scans, plotted according to the real positions (in millimeters) of the voxels, relative to the center of the monolith. As can be seen, the X-axis scan was brightest when the voxel was closest to the camera, when there was less attenuation of the emission. The Y-axis scan was symmetric about the center, with the hypothesized reason given above (the shape of the monolith refracted light away from the

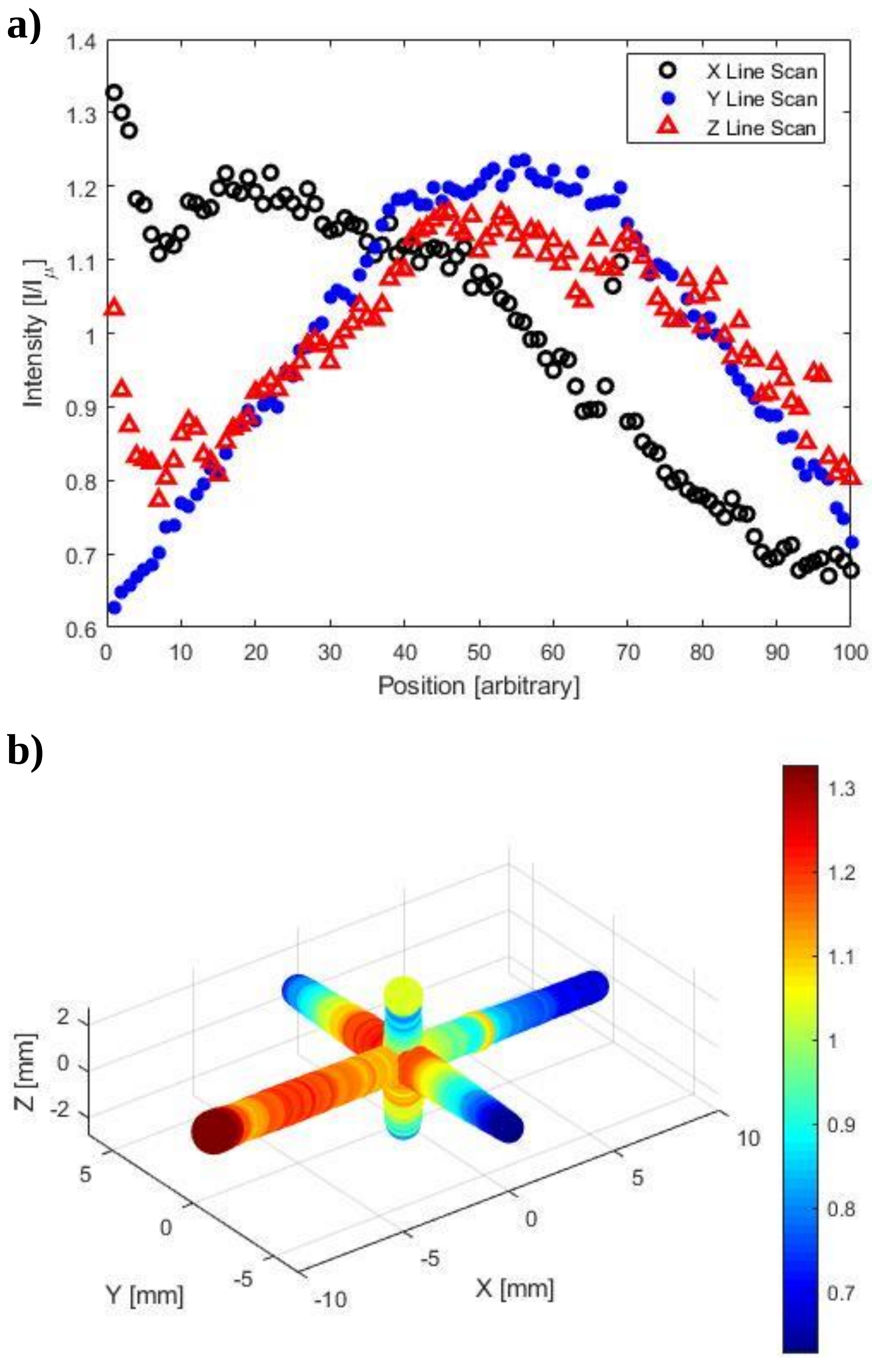

Figure 6.10 Intensity of fluorescence of line scans along the XYZ axes. a) Intensities of the three scans, normalized by the mean intensity of each scan. b) 3D scatter plot of the normalized scans, showing the to-scale lengths of each scan and relative intensity at each position.

camera). The Z-axis scan was brighter at the very top before dropping, then steadily rising again until it peaked at the center of the monolith. Using what was learned from these line scans, the next planned experiment was to scan a specified volume of the monolith and interpret the results.

6.2.3: 3D Volume Scans: Scanning Along Three Axes

To push closer to the ultimate goal of *in situ* analysis of the strain within a drying monolith, scanning a specified volume of the monolith using the linear stages to manipulate the monolith's position was the next experiment to perform. The scanning protocol was written in MATLAB (Appendix A.1.1) to start with the voxel at the top of the monolith, in the corner closest to both the camera and the laser. Then the stages moved the monolith such that the voxel would move away from the laser (along the Y-axis), with the camera capturing the fluorescence at 15 positions. The stages then moved one position over along the X-axis (away from the camera) and repeated the scan along the Y-axis. Once a 15x15 position square was captured, the stages moved the voxel back to the initial position, moved the voxel one position downward (along the Z-axis), then repeated the scans along both the X-axis and the Y-axis. The scans continued until a 15x15x15 position cube was captured, totaling 3375 positions.

The dimensions of the cube were 64 mm^3, with each side measuring 4 mm across. To determine the size of the scanned cube, two factors were considered. The scanned volume was to be kept in the center of the monolith, to avoid edge effects. There also could not be too great a distance between the furthest two points, as the camera needed to be able to capture both the faintest voxels and the brightest voxels without saturation. These two factors combined to encourage a smaller volume. At a size of 4 mm per side, and with the Basler camera's gain set to

7 on the Pylon Viewer software, the faintest voxel had a maximum intensity of approximately 100/255, while the brightest voxel was roughly 225/255. This was deemed acceptable.

The number of positions was determined based on a tradeoff between the length of time it would take to scan the volume and the resolution of the volume. Preliminary scans of 1000 points took 1845 s (roughly 30 min) to complete. Extrapolating this to a cube 25 positions long (15,625 positions total), it would take roughly 7.5 h to complete the scanning protocol. Dropping the size to 15 positions per side (3375 positions total), it was calculated that it would take roughly 1.5 h to complete (the actual scan took 82 min – roughly 1.3 h – so this was an accurate estimate). With the size of 4 mm per side, at 25 positions per side, the resolution of such a volume was 6.25 voxels per mm (or 0.16 mm between voxels). At 15 positions per side, the resolution was 3.75 voxels per mm (or 0.2667 mm between voxels). For comparison, the waist of the voxel was measured to be approximately 0.15 mm. Doubling the resolution while quintupling the time required for the scan was not seen as a viable trade, and 3.75 voxels per mm was still determined to be sufficient for this experiment. Thus, it was decided that the scanned volume would be a 64 mm^3 cube of 3375 total positions.

The results of the volume scan can be seen in Figure 6.11. The intensities of each voxel were normalized by the mean intensity of the entire volume. The brightest regions were the edge and faces closest to both the camera and the laser. The darkest region was the corner furthest from the camera and laser. Both of these were expected, as the closest parts of the volume had the least attenuation to decrease the intensity of the laser or the emissions, while the furthest parts of the volume had the most attenuation. Slices of the volume showing the fluorescence within the volume are shown in Appendix A.4.

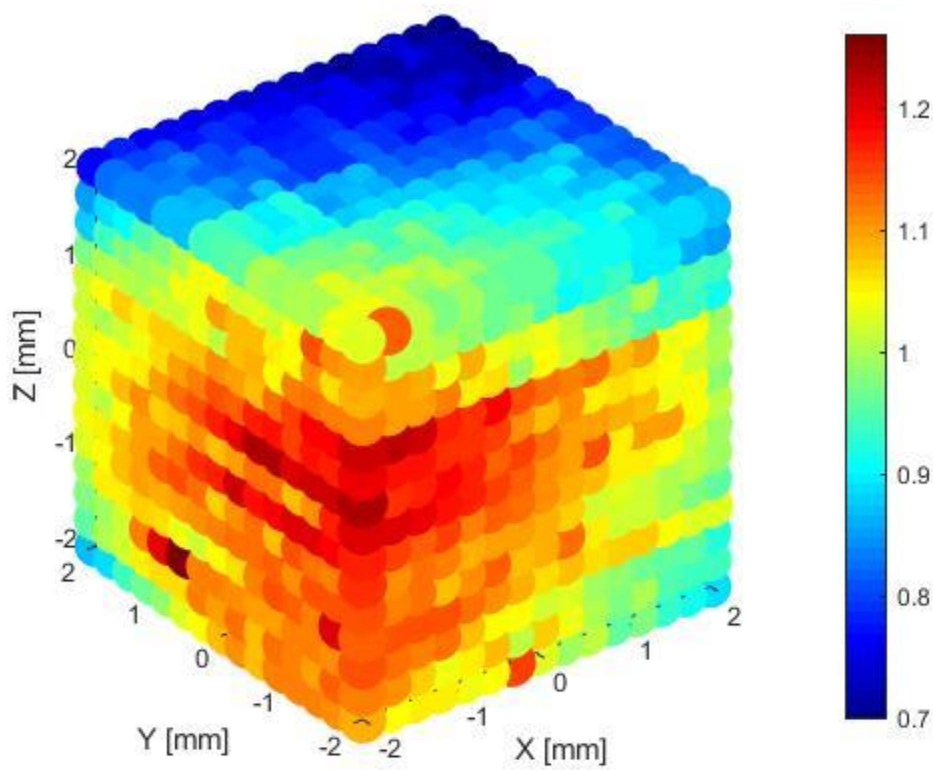

Figure 6.11 Volumetric scan of 64 mm^3 region in center of monolith, normalized by the mean intensity of the volume; 15 positions in each direction means 3375 total positions.

Figure 6.11 well-demonstrates the proof of concept for volumetric scanning; the voxel was scanned throughout the monolith, and its intensity changed due to spatial variability within the monolith. By calibrating to the intensity of an unstrained monolith, loads can be applied, and any changes in intensity could be interpreted as changes in signal due to volumetric strain. The logical next experiment would be to strain the monolith while performing the volume scan. However, concerns about the high level of noise in the previous strain experiments suggested that the most prudent course was to address the noise before performing any other strain experiments; otherwise, any changes in fluorescence due to strain could be masked by the noise, rendering any conclusions impractical. Once the noise floor was reduced to an acceptable level (e.g., about 0.1% noise), strain experiments could continue.

6.3: Mitigation of Noise

As seen in Figure 6.8, the strain experiments had enough variability that effective conclusions on the effect of volumetric strain on fluorescence intensity could not be made. To proceed, it was imperative that the noise floor be decreased. After careful consideration, it was decided that three potential sources of noise would be assessed: the camera, the laser, and the image analysis technique.

6.3.1: Noise Introduced by the Camera

To decrease the amount of noise introduced by the camera, the Canon was replaced by the Basler, as noted in Chapter 6.2.1. As a scientific camera, the Basler had a low noise floor (from Basler's products specifications page [107], EMVA quantum efficiency was given as 62.1%, dark noise was given as 13.8 e^-, and signal-to-noise ratio was given as 40.8 dB), and it was less of a "black box" than commercial cameras (for example, Canon's analogous specifications page did not provide the noise floor [109], though a qualitative analysis of the images showed that the Basler was indeed less noisy than the Canon). The Basler had accompanying software (Pylon Viewer) that allowed it to be controlled through a computer. The software was used to set the Basler camera to take one image every time the camera received a signal from an Arduino Uno, which was in

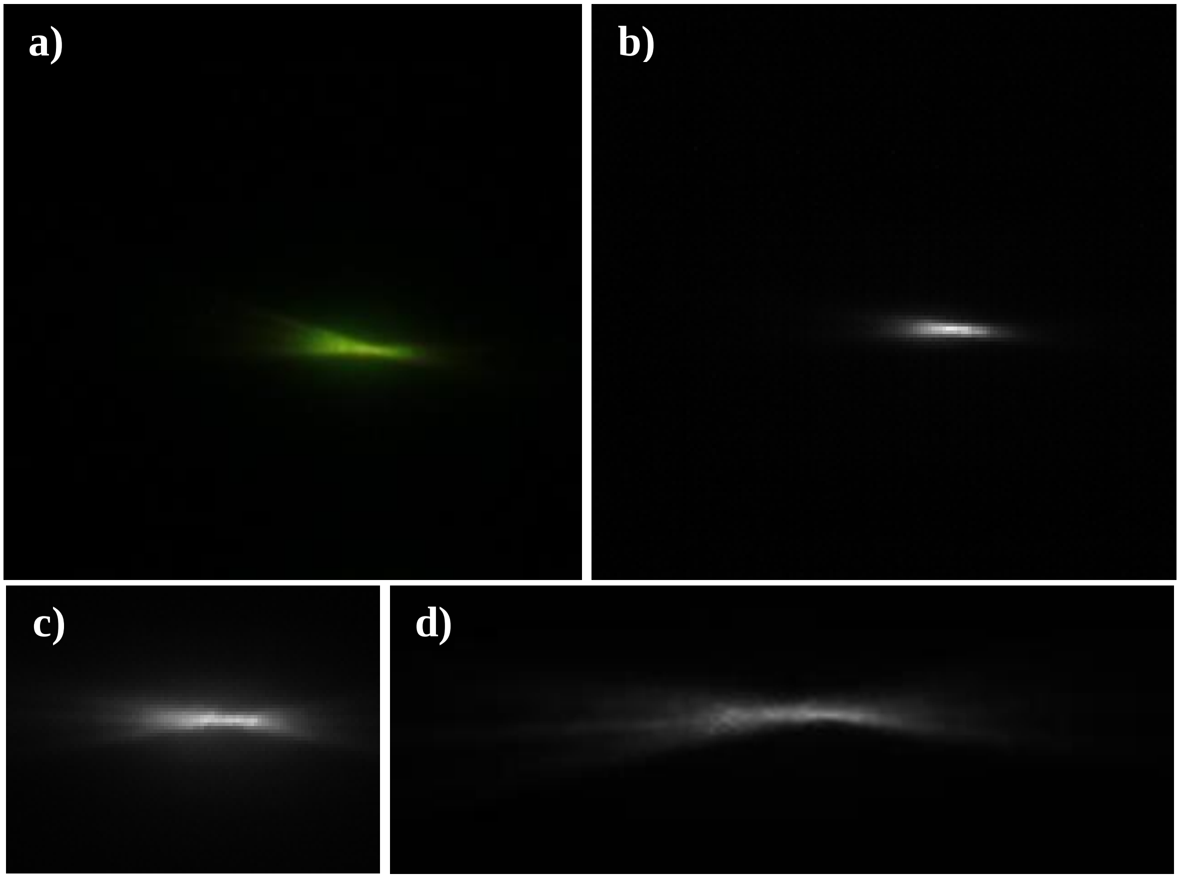

Figure 6.12 Fluorescence of nanoparticles, captured by different cameras with similar settings for exposure time and gain; a) Canon (voxel size ~2.5 mm); b) Basler (voxel size ~2.5 mm); c) FLIR (voxel size ~2.5 mm); d) FLIR with macro lens (voxel size ~2.5 mm).

turn controlled by MATLAB (Appendix A.1.4). The same MATLAB code was used to control the translation stages as well, also described in Chapter 5.4. These factors combined to allow for manipulation of both the camera trigger and the monolith position without requiring a person to manually handle either, reducing experimental inconsistencies. In time, the Basler was itself replaced by the FLIR, described in Chapter 5.3. Once again, the FLIR had a lower noise floor than the Basler (from FLIR's products specifications page [106], higher EMVA quantum efficiency at 72%, lower dark noise at 2.31 e^-, and comparable signal-to-noise ratio at 40.06 dB). The acquisition of a macro lens also allowed for images where the fluorescence represented a significantly larger portion of the image, thus allowing for the voxel to have more pixels, further reducing noise. Figure 6.12 shows representative images from each of the cameras.

6.3.2: Noise Introduced by the Laser

The laser was identified as a potentially large source of noise. It was unknown how much time the laser required to achieve thermal stability, so the laser power output at the start of an experiment could be very different from the power output at the end. Thus, to determine the time required for the laser to achieve thermal stability, an experiment was set up. The laser was turned on and kept on, with a beam block stopping the beam from reaching the monolith. Every five minutes, the beam block was removed, and the resulting fluorescence from the monolith was recorded before the beam block was replaced. With the laser continuously on but the monolith only intermittently exposed to the beam, this experiment would demonstrate how the laser power changed with time without introducing the effects of heating the monolith and/or the nanoparticles. Figure 6.13 shows the results of the experiment. It can be seen that the laser required a period of at least 30 min before the laser achieved thermal stability, with the intensity of the emission sharply dropping over time before steadying at roughly 50% of the maximum. Future experiments all required a minimum of 45 min for the laser to stabilize before capturing any images.

However, as can be seen in Figure 6.13, the “steady state” of the laser was not truly steady, as the intensity of the fluorescence still varied by 1-2%, with occasional spikes and dips that measured between 5-10% that would occur seemingly at random. Thus, to ensure that the laser power was known in real time, a laser power meter was acquired from Thorlabs – the PM16-121.

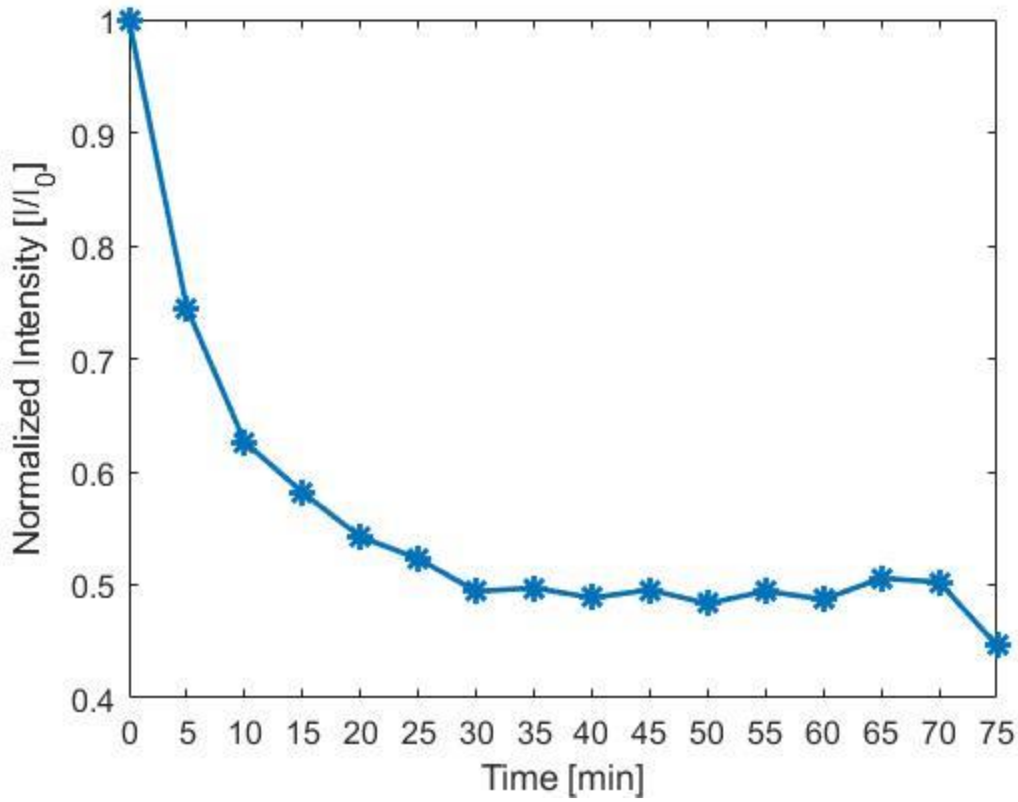

Figure 6.13 Intensity of fluorescence of monolith intermittently exposed to laser, normalized by initial intensity. The laser was powered continuously, while the path of the beam was blocked by a beam block. The beam block was removed every 5 min, exposing the monolith to the beam and allowing for fluorescence.

Ideally, the laser would have a constant output. But with the severe and seemingly random fluctuations, we corrected the signal by normalizing the measured fluorescence intensity with the power meter output. A glass slide was positioned between the laser and the beam expander setup, angled at 45°. The slide reflected roughly 8-9% of the beam, while the other 91% continued through the beam expander to the monolith. While the power meter took one measurement every

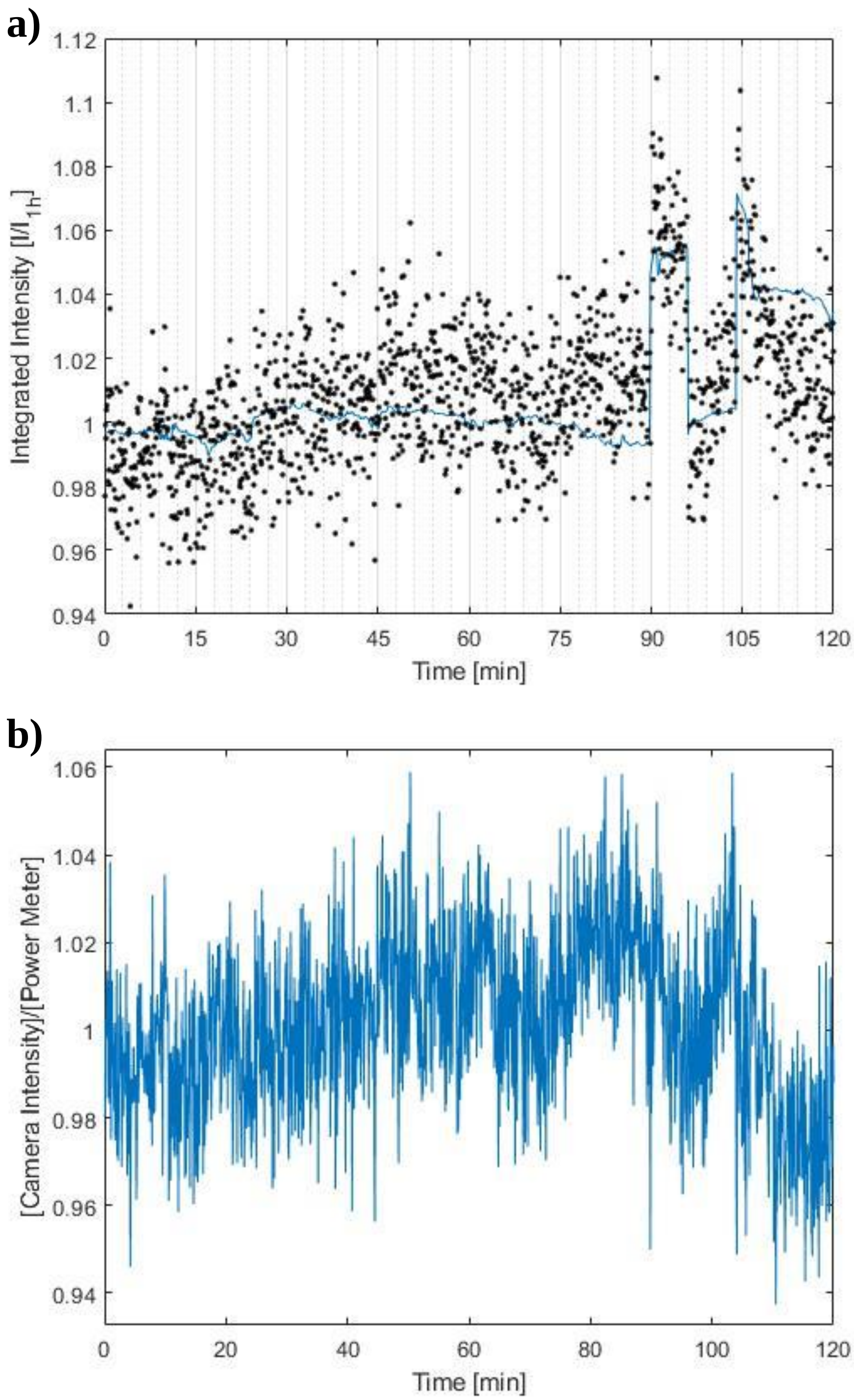

Figure 6.14 Intensity of fluorescence and laser power meter data, normalized by the first hour of data. a) The black dots are the measurements of the fluorescence, and the blue line is the power meter data; CV = 15.9862. b) Normalizing the camera measurements by the power meter data.

5 s for 2 h, the camera also captured the fluorescence in the monolith at the same rate and time. As can be seen in Figure 6.14, the power meter data and the camera measurements followed the same general path; when the power meter showed that the laser had a sharp increase or decrease in power, the camera measurements also showed a sharp increase or decrease, respectively. However, Figure 6.14 also shows that there was a large amount of fluctuation in the camera measurements. The coefficient of variation (CV) of the data was $\sigma/\mu = 15.9862$, demonstrating that there was huge variation in the camera measurements that could not be fully removed by normalizing the camera measurements with the power meter data.

6.3.3: Noise Introduced by the Image Analysis Technique

With a scientific camera and the power meter, two sources of noise (the camera and the laser) were well accounted for. The results seen in Figure 6.14 led to suspicions that the technique used to analyze the camera measurements was a possible third source of noise. Several techniques were used, with the coefficient of variability calculated for each technique.

Before the implementation of the beam expander (and for a few early experiments after), image analysis used a "thresholding" technique. As described in Chapter 6.1.1, every pixel in the image that had an intensity value lower than a specified value (the "threshold") would be treated as "not a number" and ignored. Before the beam expander, the non-NaN pixels would be averaged vertically, creating an intensity profile for the path of the beam. After the beam expander, all pixels with intensity values above the threshold would be summed together to provide a single value that represented the intensity of the fluorescence of the voxel. The "thresholding" technique was very similar to the "boxing" technique described below, which was very successful in decreasing the noise when used with the FLIR (Figure 6.17). But when it was used with microparticles or with the Canon and Basler cameras, which often had images where the fluorescence was non-continuous and/or was a small number of pixels in size, thresholding often resulted in very noisy analysis (Figure 6.2b).

Most image analysis after the implementation of the beam expander utilized a "slicing" technique: the brightest pixel in the image was identified and assumed to be the focal point of the voxel, then a horizontal slice measuring a specified number of pixels was taken across the voxel; that slice was then integrated to give a single value representing the intensity of the fluorescence of the voxel (Appendix A.1.6). This technique usually worked well when the laser had relatively small fluctuations, but large or sudden changes in laser output resulted in dramatic increases in variability (Figure 6.14, Figure 6.15). The effectiveness of the technique was also heavily dependent on the camera used. The data from Figure 6.14 was taken with the Basler, while Figure 6.15 was taken with the FLIR; the image sets from both figures were analyzed with the same slicing technique, but Figure 6.14 had a coefficient of variation of 15.9862, while Figure 6.15 had a coefficient of variation of 0.006809. This dependency on the camera was likely due to the relative number of pixels of the voxel in the images. The FLIR was capable of higher resolution than the Basler, so the voxel consisted of more pixels in the images taken by the FLIR. The larger number of pixels meant more data points to help suppress camera noise and thus improve the signal-to-noise ratio.

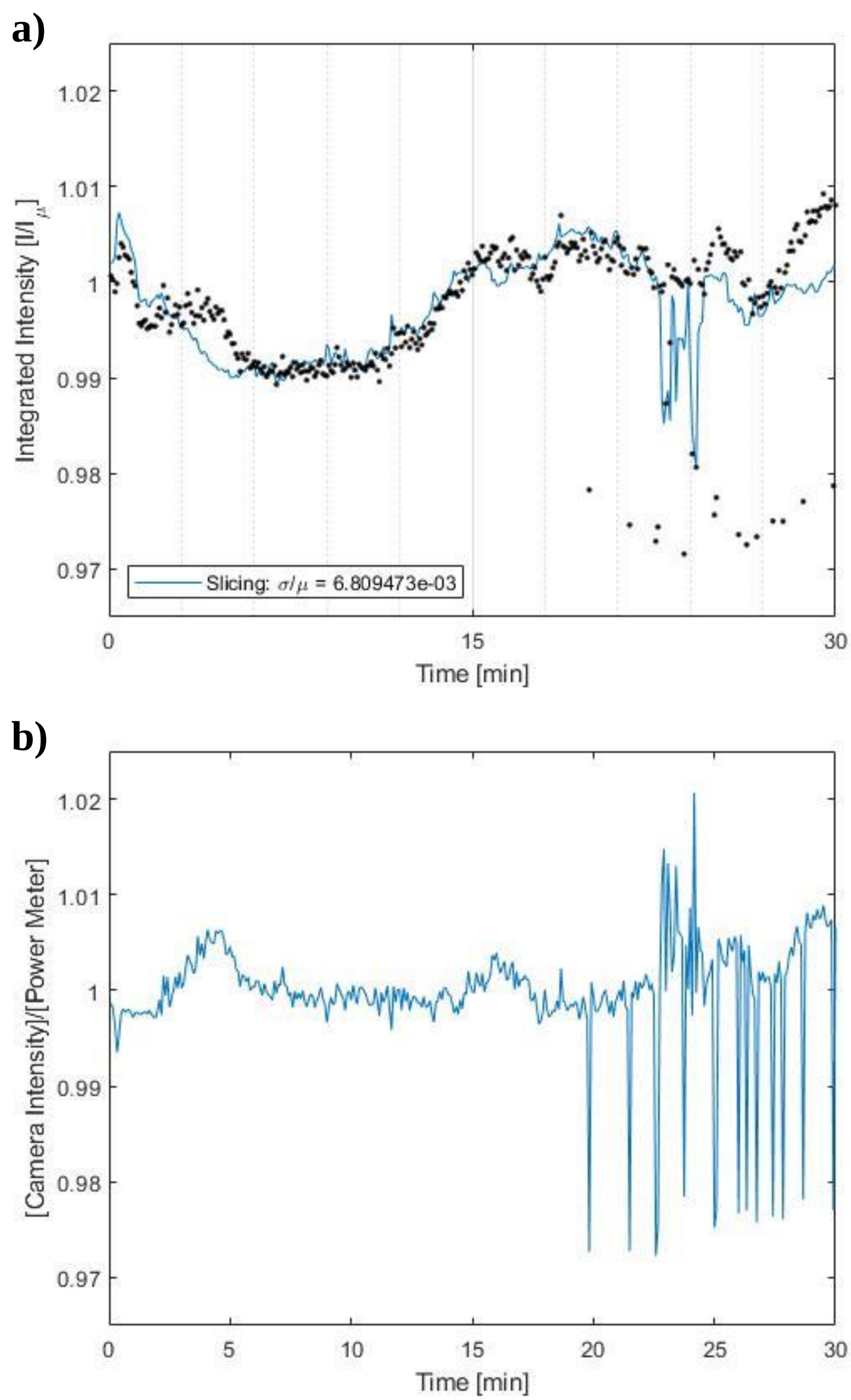

Figure 6.15 Intensity of fluorescence and laser power meter data, normalized by the mean. a) The black dots are the measurements of the fluorescence, analyzed via the slicing technique, and the blue line is the power meter data, CV = 0.006809. b) Normalizing the camera measurements by the power meter data.

When it was suspected that the image analysis technique was artificially introducing noise, a technique other than slicing was tested: fitting a Gaussian. The implementation was very similar; after identifying the brightest pixel in the voxel and “slicing” out an intensity profile, a Gaussian curve was fitted to the profile. The peak of the Gaussian was interpreted as the single value that represented the intensity of the fluorescence of the voxel (Appendix A.1.5). When analyzing images taken with the FLIR, fitting a Gaussian was not as effective as the slicing technique (Figure 6.16). However, when analyzing images taken by the Basler, fitting a Gaussian was less noisy than slicing. This was again hypothesized to be due to the relative number of pixels of the voxel in the images. Because the voxel in the Basler images was smaller and consisted of fewer pixels, it was possibly a closer match to a Gaussian than with the FLIR, as the FLIR was able to capture the cones at the edges of the voxel (Figure 6.12b and Figure 6.12c).

After seeing the results of the Gaussian analysis, another image analysis technique was tested. As noted above, the boxing technique was similar to the thresholding that was performed before. The brightest pixel in the image was identified and assumed to be the focal point of the voxel. Then a box of a specified height and width was drawn with the brightest pixel at the center of the box. All pixels outside the box were ignored, and all pixels within the box were summed to create a single value that represented the intensity of the fluorescence of the voxel (Appendix A.1.6). Using the boxing technique on images taken with the FLIR lead to the lowest noise floor so far, with a coefficient of variability of CV = 0.006699 (Figure 6.17). The laser power meter data tracked well with the analyzed images, with notable deviations when the laser power fluctuated rapidly. When the laser power did not fluctuate, the noise floor of the

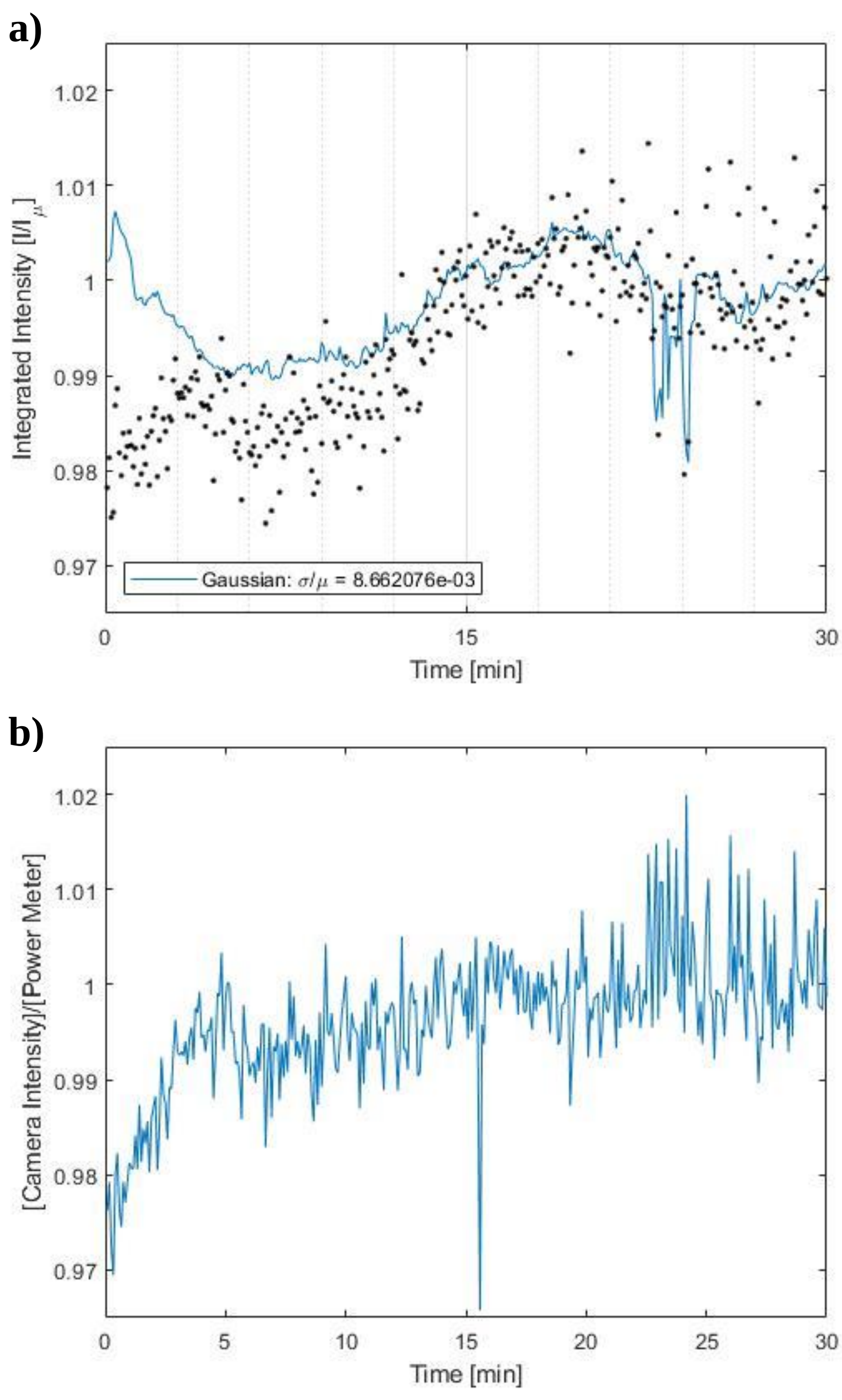

Figure 6.16 Intensity of fluorescence and laser power meter data, normalized by the mean. a) The black dots are the measurements of the fluorescence, analyzed via the Gaussian technique, and the blue line is the power meter data, CV = 0.008662. b) Normalizing the camera measurements by the power meter data.

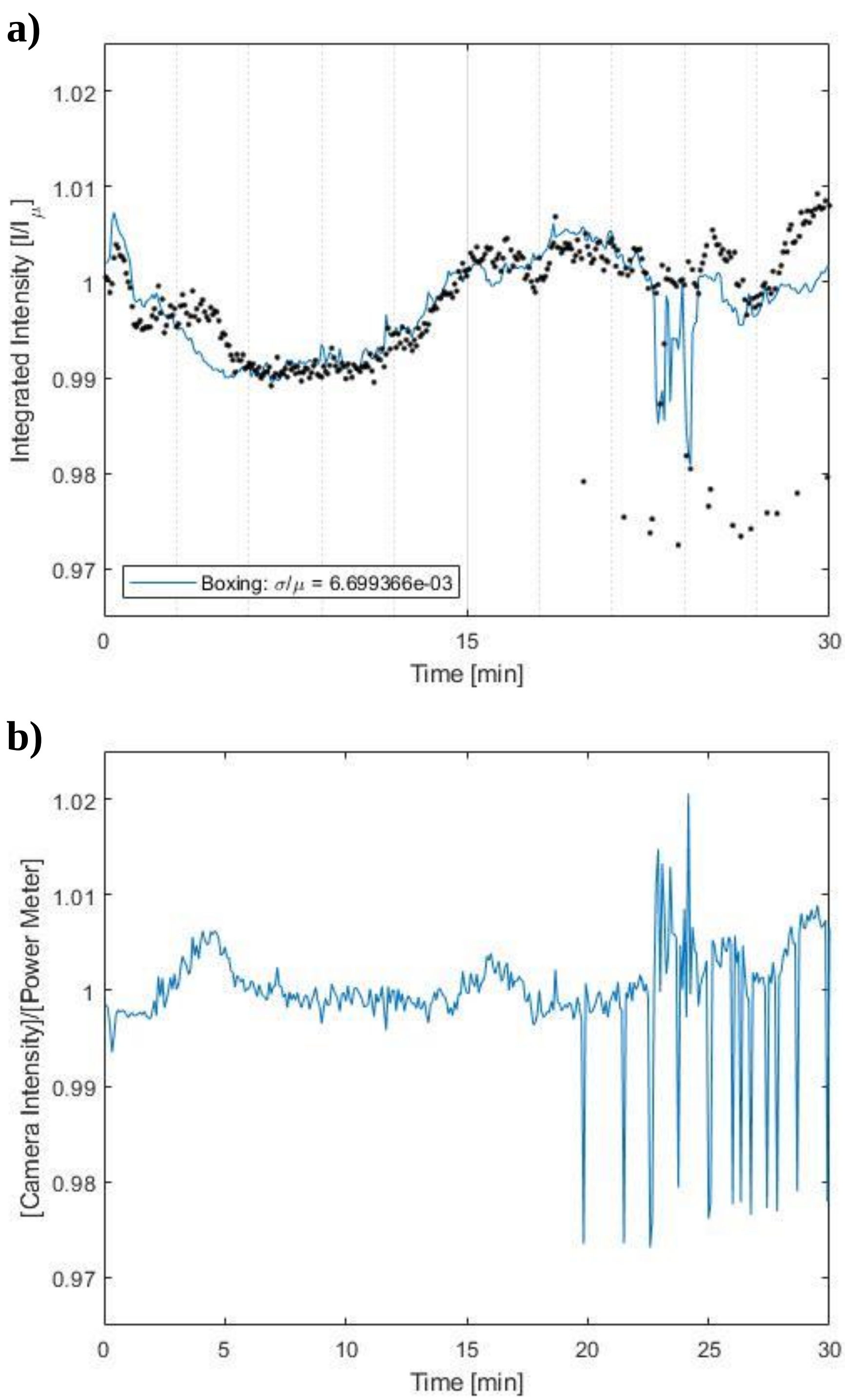

Figure 6.17 Intensity of fluorescence and laser power meter data, normalized by the mean. a) The black dots are the measurements of the fluorescence, analyzed via the boxing technique, and the blue line is the power meter data, CV = 0.006699. b) Normalizing the camera measurements by the power meter data.

analysis dropped by a factor of 6, to CV = 0.00113 (Figure 6.18). With it known that the noise floor can be dropped to as low as 0.1% when the laser power exhibits low variation, the noise was finally down to a level where a signal-to-noise ratio of up to 10 was assumed would result in a detectable difference in the fluorescence.

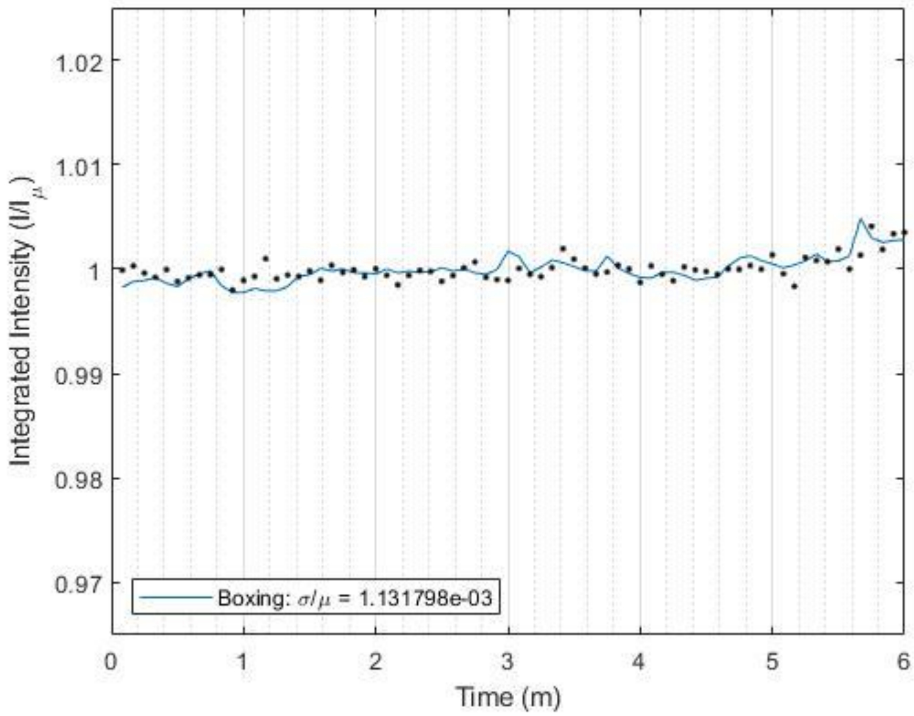

Figure 6.18 Intensity of fluorescence and laser power meter data, normalized by the mean (subset of data from Figure 6.17). The black dots are the measurements of the fluorescence, analyzed via the boxing technique, and the blue line is the power meter data, CV = 0.00113. When the laser power does not fluctuate, the noise floor of the analysis technique drops by a factor of 6.

6.4: Next Steps

After addressing the camera, the laser, and the image analysis technique, the noise floor was reduced to approximately 0.1%. With the system noise minimized, we were confident in our ability to potentially measure volumetric strains in our system (up to 0.2% before yielding). However, the signal generated from the strain resulting from a load of 3.65 kPa (the greatest load applied experimentally thus far) was very small; even with the low noise floor, if the signal itself was weak, it would be difficult to form strong conclusions. Thus, the signal must be increased before effective conclusions could be made from experimental results. One way to increase the signal would be to increase the applied loads. However, physical experiments were limited by mechanical constraints, such as the yield stress of the monoliths and the availability of different monolith formulations. When testing the viability of this optical technique, it was important to determine not only where the limits of physical experiments lie, but also what the limits *should be* in order to properly utilize the technique. Thus, rather than continuing with physical experiments, efforts shifted to numerical simulations, where materials could be tested to beyond their limits.

Chapter 7:

Simulations and Modelling

The noise floor of the image analysis technique was decreased to approximately 0.1%, yet the signal itself was still comparable to the noise when a stress of 3.65 kPa was applied to the physical monolith. Two questions became pertinent: 1) what level of volumetric strain would result in a change in fluorescence that would be large enough to detect, and 2) what kinds of aerogels would be capable of achieving such volumetric strains? To answer the first question, it was assumed that a signal-to-noise ratio approaching 10 would be detectable through the image analysis technique. It was also assumed that the intensity of fluorescence and the reciprocal of volumetric strain were linearly correlated: as volumetric strain decreased, the fluorescence would increase by approximately the same amount. Thus, it was assumed that a minimum of 1% volumetric strain would result in a detectable change in fluorescence intensity. Numerical simulations would allow for the second question to be answered. By creating a computer model with variable properties, not only could several different aerogel formulations be tested, but they could also be subjected to loads well beyond their yield stresses. This would determine what kinds of aerogels would meet the requirements for 1% volumetric strain.

7.1: Modelling in COMSOL: Geometry, Boundary Conditions, and Mesh

The simulations were run using COMSOL 5.2. In all simulations, the aerogel monolith was modelled as a disc with radius 10 mm and height 10 mm, roughly corresponding to the size of the silica aerogel discs that were used in the physical experiments. Symmetrical boundary conditions were set such that only one quarter of the disc would need to be modelled. The particles within the monolith were modelled as rigid, incompressible "voids" by subtracting spheres from the monolith model and using the "Rigid Connector" boundary condition to treat the voids as rigid bodies. As the physical $NaYF_4$:Yb/Er particles are substantially more rigid than the aerogel matrix (the silica aerogel formulation used should have a Young's modulus of approximately 4.1 MPa [derivations in 7.1.1], while the particles have a Young's modulus of approximately 300 GPA [110]), it was assumed that the particles could be approximated as incompressible relative to the monolith. Simulated particle size ranged from radius 0 mm (i.e., no particles) to radius 0.5 mm. The applied loads were modelled as pressures applied to the top surface of the monolith model (i.e., uniaxial compression), and the bottom surface of the model was restricted with boundary conditions such that it could not translate or rotate.

The mesh element size for the models was set to "Normal;" while a more refined mesh increased the accuracy of the simulations for smaller particle radii, this also dramatically increased computation times (from 45 s for "Normal" to 20 min for "Finer" for a single computational run). The difference between the volumetric strain of a simulation with "Normal" mesh and "Finer" mesh was 11.92%. While not insignificant, when considering the tradeoff between refinement and computation time, a "Normal" mesh was deemed sufficiently accurate (Figure 7.1).

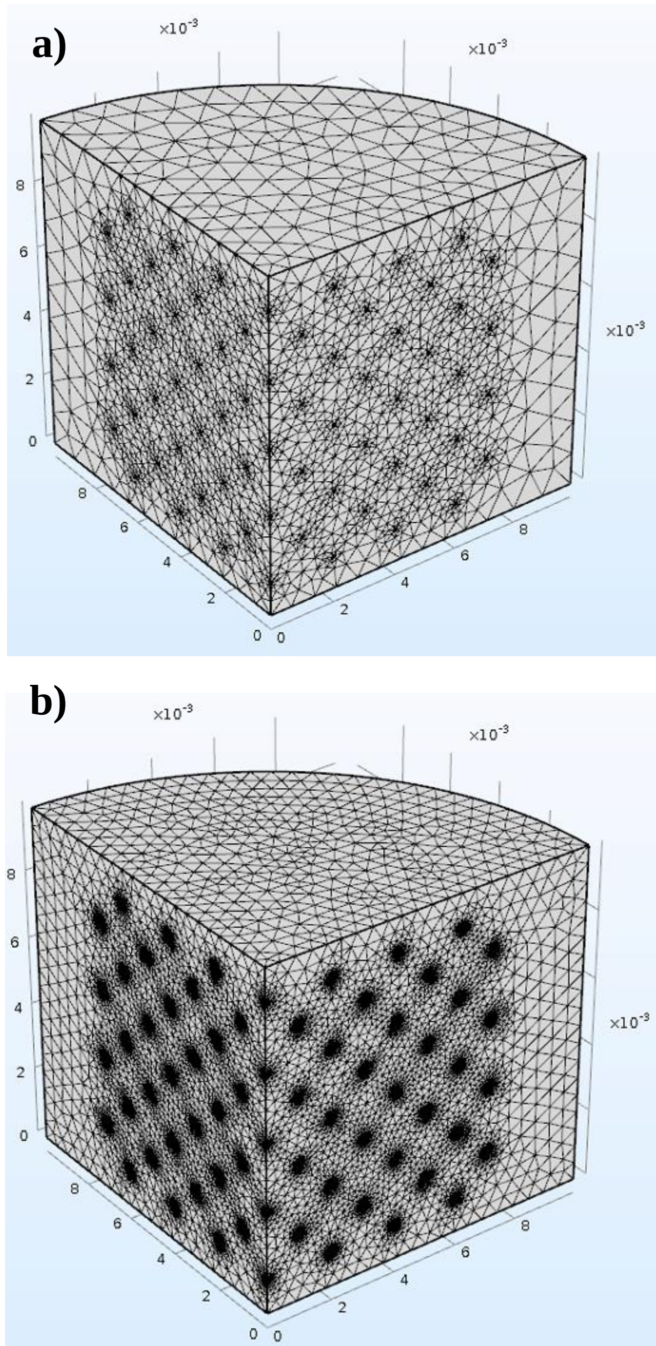

Figure 7.1 Comparison between mesh element sizes; a) “Normal” mesh, and b) “Finer” mesh.

7.2: Uniaxial Compression with No Particles

The first simulations were for the simplest case: a silica aerogel monolith with no particles under uniaxial compression. The properties used to model silica aerogel were Young's modulus, Poisson's ratio, and density. It is well-established that the Young's modulus of silica aerogels follows a power-law relationship with the fabrication density of said aerogels, as seen in Equation 7.1:

$$E = \alpha\rho^{\beta} \tag{7.1}$$

Specifically, Rivas Murillo et al. 2010 [15] and Lei et al. 2013 [111] found that the relationship followed Equation 7.2 and Equation 7.3, respectively.

$$E = 3 \times 10^{-6}\rho^{3.11} \tag{7.2}$$

$$E = 2.223 \times 10^{-6}\rho^{3.168} \tag{7.3}$$

The silica aerogel formulation used in the physical experiments was a modified version of the formulation found at Aerogel.org [103]. Said formulation has a stated density of 0.095 g/cc, thus it was assumed that the modified formulation would have a similar density. Using that density in Equation 7.2 and Equation 7.3 resulted in a Young's modulus of 4.2446 MPa and 4.0961 MPa, respectively. The Young's modulus of the silica aerogel formulation used in the physical experiments (and thus, the Young's modulus of the modelled silica aerogel) was assumed to be approximately 4.1 MPa. Patil et al. 2017 [112] found that the Poisson's ratio of silica aerogel does not vary much with density and is actually similar to the Poisson's ratio of silica glass (i.e., 0.2). Thus, the modelled silica aerogel was assumed to have a Poisson's ratio of 0.2.

After the values for the Young's modulus, Poisson's ratio, and density were applied to the model, the model was subjected to ten loads: 3.65 kPa (the highest load applied in physical experiments), 10 kPa, 18.685 kPa (the assumed yield strength of the silica aerogel formulation, calculated from Woignier et al. 1998 [113]), 50 kPa, 68.3333 kPa (the load required to reach 1% volumetric strain), 100 kPa, 200 kPa, 500 kPa, 1000 kPa, and 3416.6667 kPa (the load required to reach 50% volumetric strain). Table 7.1 shows the simulated volumetric strain as a function of applied load. The simulations match the expected strains calculated using the equation $\epsilon_v = \frac{\sigma}{E}(1-2\nu)$, derived from an algebraic manipulation of Hooke's Law. From here, particles of varying size were added to the model.

Table 7.1 Simulated Volumetric Strain vs. Applied Load, Silica Aerogel with No Particles

Applied Load [kPa]	Volumetric Strain [ ]
3.65	-0.000534
10	-0.00146
18.685	-0.00273
50	-0.00732
68.3333	-0.01
100	-0.01463
200	-0.02927
500	-0.07317
1000	-0.14634
3416.6667	-0.5

7.3: Analyzing the Effect of Particles on Volumetric Strain

After confirming that the simplest case (i.e., no particles) matched expected results, particles were simulated through the aforementioned "voids" cut out of the monolith model. First, nine particles with radius 0.5 mm were arranged in a body-centered cubic lattice (Figure 7.2a), with the center particle located at the geometric center of the monolith model. The centers of each corner particle were separated by 2 mm from adjacent corner particles. A load of 68.3333 kPa was applied to the monolith, and the volumetric average of the volumetric strain was calculated via COMSOL's built-in functions. The simulated particle radius was then varied from 0.5 mm to 0.005 mm, with particle separation and particle number held constant. The largest particle size (i.e., 0.5 mm radius) was selected to model the effect of large particles with length scales on similar orders to the radius of the monolith (i.e., 10 mm). The smallest particle size (i.e., 0.005 mm radius) was on the same order as the physical microparticles used in Chapter 6.1 (i.e., 1-5 µm diameter) and was also the smallest particle that could be modelled in COMSOL. The effect of variable particle radius on volumetric strain can be seen in Table 7.2.

As expected, larger particle sizes deviate from the baseline case of "no particles." Once particle radius drops to 0.01 mm, the relative error of volumetric strain when compared to the "no particle" case becomes 0.4445%. As the physical particles are on the micro- and nanoscales, it can be assumed that particle size has little effect on volumetric strain once the particles are no longer on the same length scale as the monolith. Thus, it can be assumed that aerogel monolith nanocomposites can be modelled as homogeneous structures, regardless of the presence of particles. After particle size was eliminated as a variable, the number of particles was increased to better simulate the physical monoliths (Figure 7.2b). Over 200 particles were added to the model, still following the body-center cubic lattice.

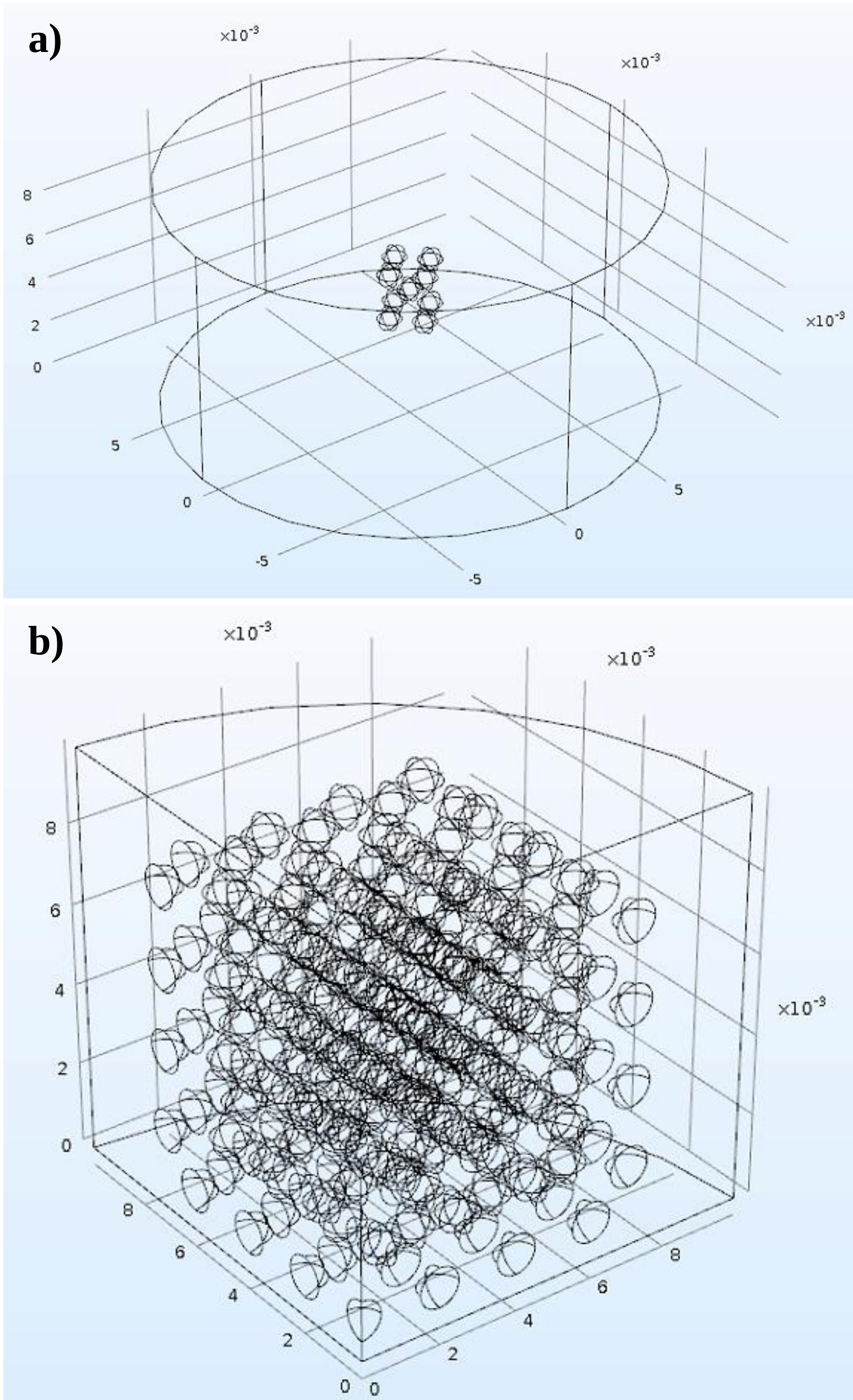

Figure 7.2 COMSOL model of silica aerogel disc under uniaxial compression. a) A full disc with nine particles. b) A quarter disc with 210 particles.

Table 7.2 Volumetric Strain vs. Particle Radius, Silica Aerogel with Applied Load 68.3333 kPa

Particle Radius [mm]	Volumetric Strain [ ]
0.5	-0.00461
0.25	-0.0058
0.1	-0.0076
0.05	-0.00877
0.025	-0.00966
0.01	-0.00996
0.005	-0.01001

7.4: Nondimensionalization of Variables

With the particle number and particle separation (i.e., center-to-center distance) kept constant, there were still three variables that were tested for effects on volumetric strain: 1) particle radius; 2) applied stress; and 3) aerogel formulation. To maintain consistency between the formulations, nondimensionalization was utilized. By nondimensionalizing the stresses and monolith properties, it became trivial to test multiple different aerogel formulations, allowing for an answer to the second question above to be found: what formulations of aerogels would be capable of achieving volumetric strains large enough to detect without yielding? After identifying the dependent variable (volumetric strain) and all possible independent variables, the variables were rewritten to cancel out the dimensions, resulting in four relevant dimensionless variables (Poisson's ratio, particle number density, dimensionless particle radius, and dimensionless stress). The full dimensional analysis can be found in Appendix A.2.

After nondimensionalization, the variable that represented aerogel formulation was the Poisson's ratio (the other relevant variable Young's modulus was already accounted for through dimensionless stress $\bar{\sigma} = \sigma/E$). Silica aerogel formulations were represented in the modelling with Poisson's ratio of 0.2, so three additional formulations were sought. To represent formulations with very high compressibility, cellulose aerogel was selected, as it has a Poisson's ratio of 0.0 [114], meaning that an applied uniaxial load will not result in any deformation in the orthogonal directions. To represent formulations with very low compressibility, graphene aerogels were selected, as they have been demonstrated to have tunable Poisson's ratio ranging from -0.3 to +0.46 [115]. Thus, the Poisson's ratios for relatively incompressible formulations were selected to be 0.3 and 0.46 (negative Poisson's ratios were not simulated).

Table 7.3 shows the nondimensionalized stress (derived from the dimensional stresses applied to the silica model) and the dimensional equivalent stresses to be applied to the cellulose and graphene models. The columns represent, from left to right: 1) the dimensional stresses applied to the silica model; 2) the nondimensionalized stresses; 3) the dimensional stresses applied to cellulose; and 4) the dimensional stresses applied to both graphene formulations. The dimensional values for particle radius, applied stress, and aerogel properties (like Young's modulus and Poisson's ratio; see Table 4) were entered into COMSOL, and their effects on volumetric strain were simulated.

Table 7.3 Nondimensionalized Stress

Dimensional Stress (Silica) [kPa]	Nondimensionalized Stress [ ]	Dimensional Stress (Cellulose) [kPa]	Dimensional Stress (Graphene) [kPa]
3.65	0.00089	1.42439	0.018695
10	0.002439	3.902439	0.05122
18.685	0.004557	7.291707	0.095704
50	0.012195	19.5122	0.256098
68.3333	0.016667	26.66665	0.35
100	0.02439	39.02439	0.512195
200	0.04878	78.04878	1.02439
500	0.121951	195.122	2.560976
1000	0.243902	390.2439	5.121951
3416.6667	0.833333	1333.333	17.5

Table 7.4 Simulated Formulation Properties

Formulation	Poisson's Ratio	Young's Modulus
Silica	0.2	4.1 MPa
Cellulose	0.0	1.6 MPa
Graphene (0.3)	0.3	21 kPa
Graphene (0.46)	0.46	21 kPa

Figures 7.3-7.5 show volumetric strain versus nondimensionalized stresses, separated by particle radius. The volumetric strain is normalized by $(1 - 2\nu)$, a specific form of Poisson's ratio derived from the algebraic manipulation of Hooke's Law described in Chapter 7.2. It can be seen from Figure 7.3 that the volumetric strain curves for all four tested formulations collapse, as

expected from the nondimensionalization process. As particle size increases, the curves deviate from each other and do not collapse anymore. However, this reveals that volumetric strain seems to increase monotonically with increasing Poisson's ratio. In Figures 7.4 and 7.5, it can be seen that cellulose (which has the smallest Poisson's ratio of 0.0) has the smallest volumetric strain, while graphene with Poisson's of 0.46 has the highest volumetric strain. This also is expected, as a higher Poisson's ratio means that uniaxial compression will result in more lateral deformation when compared with smaller Poisson's ratios.

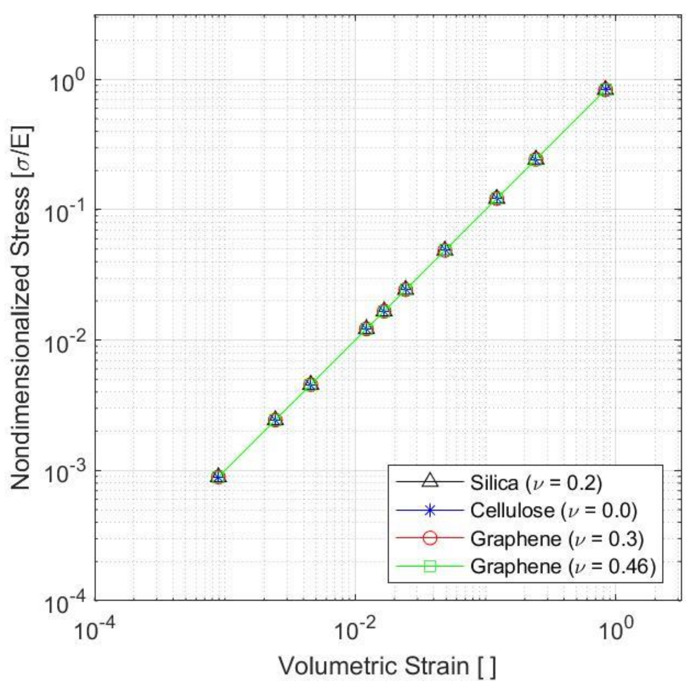

Figure 7.3 Poisson-normalized volumetric strain versus nondimensionalized stresses: no particles.

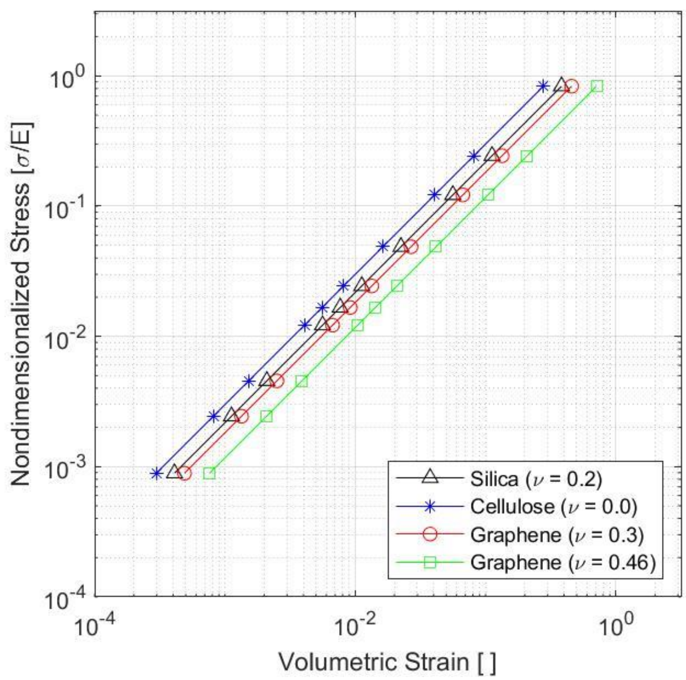

Figure 7.4 Poisson-normalized volumetric strain versus nondimensionalized stresses for particles with r = 0.5 mm.

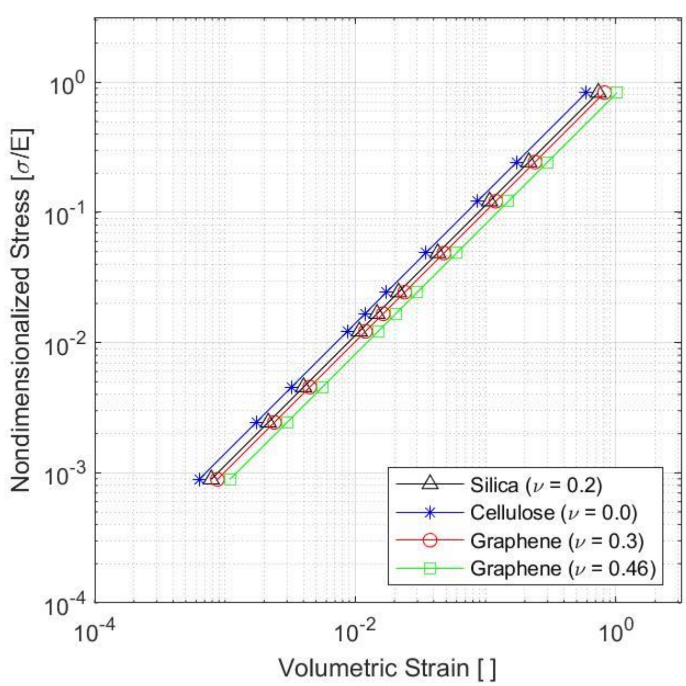

Figure 7.5 Poisson-normalized volumetric strain versus nondimensionalized stresses for particles with r = 0.05 mm

7.5: What was Learned from Simulations

The simulations of four aerogel formulations with very different properties suggest that the best aerogel formulations for identifying a visible change in fluorescence intensity are the aerogels that are capable of undergoing dramatic deformations without yielding. To reach the assumed visible minimum of 1% volumetric strain, silica aerogel requires far in excess of its yield stress, while cellulose can reversibly undergo strains up to 99% [114]. Graphene has an ultimate strength of 990 kPa [115], well beyond the stress required to produce 50% volumetric strain. Thus, brittle aerogels like silica are not preferred over less friable aerogels like cellulose and graphene.

Using what was learned from these simulations, additional physical experiments should be performed. Previous experiments did not subject the silica monolith to stresses above 3.65 kPa; additional experiments should apply at least the yield stress (estimated to be 18.685 kPa for the specific silica aerogel formulation used in these physical experiments). At the estimated yield stress, the numerical simulations produced a volumetric strain of roughly 0.27%, which is also on the same order as the noise floor of the image analysis technique; if the physical experiment has similar results, the experiment would likely verify the limits of using this technique on this specific silica formulation. Thus, physical experiments involving other formulations should be pursued. As noted, both cellulose and graphene can withstand strains far beyond 50% volumetric strain, much more than the brittle silica formulation used. However, polymer-reinforced silica aerogels have been shown to recover from up to 25% compressive strain [116,117]. Additional physical experiments applying uniaxial compression to cellulose aerogels (very compressible), high-Poisson's ratio graphene aerogels (very incompressible), and polymer-reinforced silica aerogels (a stronger formulation than the silica used previously) would provide results that either support or fail to support the conclusions made from the numerical simulations: the analysis technique is most viable for aerogel formulations that can experience large deformations (greater than 1% strain) without fracture.

Chapter 8:

Conclusions and Recommendations

The goal of this work was to develop an optical scanning technique that could observe the strain of a drying aerogel monolith *in situ* using fluorescent particles. To determine the viability of the optical technique, it was first developed using *ex situ* experiments, where an already-dried fluorescent aerogel monolith nanocomposite was strained while interrogated by a voxel of illumination from a focused IR laser. Any changes in the intensity of the fluorescence of the voxel were captured by a camera and analyzed in MATLAB. The results of the *ex situ* experiments, shown throughout Chapter 6, demonstrate that the optical technique can be successfully used to scan through a specified volume of a monolith, with a noise floor as low as 0.1%. However, the maximum applied stress in the physical experiments was small (3.65 kPa, resulting in 0.05% volumetric strain). It was hypothesized that a minimum of 1% volumetric strain would be required to produce a visible change in the fluorescence intensity, so the changes in the signal from only 0.05% volumetric strain were too small to make strong conclusions. To compensate for the limitations of the physical experiments, numerical simulations were performed such that the stresses required to produce strains ranging from 1% volumetric strain to 50% volumetric strain in four different aerogel formulations were identified, as documented in Chapter 7. From those simulations, it was concluded that the stress required for 1% volumetric strain in silica aerogel (68.3333 kPa) was well beyond the yield stress of silica aerogel monoliths of comparable density to the formulation used in the physical experiments (18.685 kPa).

Using what was learned from these simulations, additional physical experiments should be performed; the silica monolith should be subjected to at least the yield stress (18.685 kPa) and observed for notable changes in fluorescence intensity. A laser with more stable power output should be utilized. In-house nanoparticle synthesis should be revisited (either through additional attempts of the previous three protocols or through attempting additional protocols found within the literature), as the synthesis of large quantities of nanoparticles would allow for the production of silica monoliths with high particle densities, increasing the fluorescence intensity. Other aerogel formulations should also be explored, such as cellulose aerogels, graphene aerogels, and polymer-reinforced silica aerogels. The results of such experiments would provide data that could support the conclusion made from the numerical simulations: the optical scanning technique is most viable for aerogel formulations that can experience large deformations (greater than 1% strain) without fracture.

However, uniaxial compression is not necessarily reflective of the forms of stresses that a drying aerogel monolith can expect to experience. It is not uncommon for a drying monolith to undergo over 25% volumetric strain while shrinking, permanently deforming but not fracturing [29]. Thus, for *in situ* measurements of strain, this technique can still be viable even for very brittle aerogel formulations like silica. This technique has not been tested with *in situ* experiments, but there is a potential, as seen with *ex situ* experiments and simulations. Additional experiments should be based around *in situ* analysis; silica formulations embedded with fluorescent particles should be dried in a pressure vessel with optical access, while a lens configuration focuses the IR laser within the monolith. Similarly to the *ex situ* experiments, while the monolith is experiencing stress during drying, a camera should record any changes to the fluorescence intensity of the illuminated voxel. Such experiments would confirm the viability of the technique in *in situ* applications.

There is a potential difficulty in applying the strain mapping technique to *in situ* analysis: to produce a small voxel with low aspect ratio, a focusing lens with short focal length (FL = +25.4 mm) was used for *ex situ* analysis, thus the monolith must be within 25.4 mm away from the focusing lens. Since the monolith must be dried within a pressure vessel for *in situ* analysis, the geometry of the vessel could be a limiting factor; the walls of the vessel (and any windows created for optical access) must be thick enough to withstand the high pressures of the supercritical drying process, but such a thick-walled vessel would likely not be able to allow the monolith to be close enough to the focusing lens. This is a problem that could potentially be solved via intersecting beam sheets. By using a cylindrical lens to expand the beam along only one axis, the resulting beam sheet could be shown through the monolith. Hypothetically, intersecting the beam sheet with another beam sheet would produce a line of detectable fluorescence along the line of intersection; introducing a third beam sheet (and decreasing the excitation power of each beam sheet appropriately) would produce detectable fluorescence only at the single point where all three sheets intersect. However, as noted in Chapter 5.1, crossing two beams using a beam splitter did not produce a small voxel of illumination; rather, fluorescence was visible throughout the paths of both beams. Intersecting three beam sheets could have similar results. Experiments varying the properties of the cylindrical lenses should be performed before making strong conclusions.

There are limitations for the large-scale implementation of this technique. While there is evidence suggesting a positive correlation between induced strain and fluorescence intensity, it has not yet been demonstrated in physical experiments that strains on the order of 1% can be accurately mapped to changes in fluorescence intensity. In addition, if this technique is to be developed for use in 3D volumetric displays, the voxel of illumination must be smaller, more spheroidal, and able to scan through its medium at high speeds. However, if the signal is large enough and consistent enough, by mapping strain to fluorescence intensity, *in situ* strain measurements can be used for real-time monitoring of any transparent structure undergoing strain.

References

[1] Aegerter, M. A., Leventis, N., and Koebel, M. M., eds., 2011, *Aerogels Handbook*, Springer New York, New York, NY.

[2] Fricke, J., 1992, "Aerogels and Their Applications," J. Non-Cryst. Solids, **148**, pp. 356–362.

[3] Smirnova, I., and Gurikov, P., 2018, "Aerogel Production: Current Status, Research Directions, and Future Opportunities," J. Supercrit. Fluids, **134**, pp. 228–233.

[4] Gurav, J. L., Jung, I.-K., Park, H.-H., Kang, E. S., and Nadargi, D. Y., 2010, "Silica Aerogel: Synthesis and Applications," J. Nanomater., **2010**, pp. 1–11.

[5] Koebel, M., Rigacci, A., and Achard, P., 2012, "Aerogel-Based Thermal Superinsulation: An Overview," J. Sol-Gel Sci. Technol., **63**(3), pp. 315–339.

[6] Cuce, E., Cuce, P. M., Wood, C. J., and Riffat, S. B., 2014, "Toward Aerogel Based Thermal Superinsulation in Buildings: A Comprehensive Review," Renew. Sustain. Energy Rev., **34**, pp. 273–299.

[7] McFarlane, B., 2013, "Garment with Aerogel Insulation," p. 7.

[8] Markesbery, M. G., and Venna, R., 2016, "Garment with Strategically Positioned Polyimide Aerogel Panels," p. 17.

[9] Nelson, R., Griffin, J. S., Kiziltas, A., Mielewski, D., and Steiner, S. A., III, 2018, "Automotive Engine Covers Made From Mechanically Strong Monolithic Polymer Aerogels," *Fourth International Seminar on Aerogels 2018*, Hamburg, Germany.

[10] Hogan, E. J., Krajewski, M. T., and Muthukumaran, P., 2007, "Aerogel-Based Vehicle Thermal Management Systems and Methods," p. 23.

[11] Marques, L. M., Carrott, P. J. M., and Ribeiro Carrott, M. M. L., 2016, "Carbon Aerogels Used in Carbon Dioxide Capture," Carbon.

[12] Guo, X., Ding, L., Kanamori, K., Nakanishi, K., and Yang, H., 2017, "Functionalization of Hierarchically Porous Silica Monoliths with Polyethyleneimine (PEI) for CO_2 Adsorption," Microporous Mesoporous Mater., **245**, pp. 51–57.

[13] Anas, M., Gönel, A. G., Bozbag, S. E., and Erkey, C., 2017, "Thermodynamics of Adsorption of Carbon Dioxide on Various Aerogels," J. CO2 Util., **21**, pp. 82–88.

[14] Thapliyal, P. C., and Singh, K., 2014, "Aerogels as Promising Thermal Insulating Materials: An Overview," J. Mater., **2014**, pp. 1–10.

[15] Rivas Murillo, J. S., Bachlechner, M. E., Campo, F. A., and Barbero, E. J., 2010, "Structure and Mechanical Properties of Silica Aerogels and Xerogels Modeled by Molecular Dynamics Simulation," J. Non-Cryst. Solids, **356**(25–27), pp. 1325–1331.

[16] Bisson, A., Rigacci, A., Lecomte, D., Rodier, E., and Achard, P., 2003, "Drying of Silica Gels to Obtain Aerogels: Phenomenology and Basic Techniques," Dry. Technol., **21**(4), pp. 593–628.
[17] Lolli, N., and Andresen, I., 2016, "Aerogel vs. Argon Insulation in Windows: A Greenhouse Gas Emissions Analysis," Build. Environ., **101**, pp. 64–76.
[18] Griffin, J. S., Nelson, R., and Steiner, S. A., III, 2018, "Synthesis and Characterization of High-Strength, High-Temperature, Flexible, Water-Resistant Polyamide Aerogels," *Fourth International Seminar on Aerogels 2018*, Hamburg, Germany.
[19] Lei, J., Hu, J., and Liu, Z., 2013, "Mechanical Properties of Silica Aerogel – A Molecular Dynamics Study," Adv. Struct. Eng. Mech., pp. 778–785.
[20] Elmanovich, I. V., Pryakhina, T. A., Gallyamov, M. O., Migulin, D. A., Meshkov, I. B., Vasil'ev, V. G., and Muzafarov, A. M., 2019, "Silicone Aerogels with Tunable Mechanical Properties Obtained via Hydrosilylation Reaction in Supercritical CO2," J. Supercrit. Fluids, **149**, pp. 120–126.
[21] Bay, B. K., Smith, T. S., Fyhrie, D. P., and Saad, M., 1999, "Digital Volume Correlation: Three-Dimensional Strain Mapping Using X-Ray Tomography," Exp. Mech., **39**(3), pp. 217–226.
[22] Tong, W., 2005, "An Evaluation of Digital Image Correlation Criteria for Strain Mapping Applications," Strain, **41**(4), pp. 167–175.
[23] Mao, L., and Chiang, F., 2016, "3D Strain Mapping in Rocks Using Digital Volumetric Speckle Photography Technique," Acta Mech., **227**(11), pp. 3069–3085.
[24] Bart-Smith, H., Bastawros, A. F., Mumm, D. R., Evans, A. G., Sypeck, D. J., and Wadley, H. N. G., 1998, "Compressive Deformation and Yielding Mechanisms in Cellular Al Alloys Determined Using X-Ray Tomography and Surface Strain Mapping," Acta Mater., **46**(10), pp. 3583–3592.
[25] Zeng, J. S. Q., Stevens, P. C., Hunt, A. J., Grief, R., and Lee, D., 1996, "Thin-Film-Heater Thermal Conductivity Apparatus and Measurement of Thermal Conductivity of Silica Aerogel," Int. J. Heat Mass Transf., **39**(11), pp. 2311–2317.
[26] Tabata, M., Adachi, I., Ishii, Y., Kawai, H., Sumiyoshi, T., and Yokogawa, H., 2010, "Development of Transparent Silica Aerogel over a Wide Range of Densities," Nucl. Instrum. Methods Phys. Res. Sect. Accel. Spectrometers Detect. Assoc. Equip., **623**(1), pp. 339–341.
[27] Woods, T., 2011, "Aerogels: Thinner, Lighter, Stronger," NASA [Online]. Available: https://www.nasa.gov/topics/technology/features/aerogels.html.
[28] Brinker, C. J., and Scherer, G. W., 1985, "Sol → Gel → Glass: I. Gelation and Gel Structure," J. Non-Cryst. Solids, **70**(3), pp. 301–322.
[29] Scherer, G. W., 1988, "Aging and Drying of Gels," J. Non-Cryst. Solids, **100**(1–3), pp. 77–92.
[30] Iswar, S., Malfait, W. J., Balog, S., Winnefeld, F., Lattuada, M., and Koebel, M. M., 2017, "Effect of Aging on Silica Aerogel Properties," Microporous Mesoporous Mater., **241**, pp. 293–302.
[31] Omranpour, H., and Motahari, S., 2013, "Effects of Processing Conditions on Silica Aerogel during Aging: Role of Solvent, Time and Temperature," J. Non-Cryst. Solids, **379**, pp. 7–11.
[32] Mills, D. H., 2011, "Apparatus to Measure Ethanol Extraction Rates During Supercritical CO_2-Based Drying of Alcogels," Master's Thesis, Tufts University.

[33] Shimizu, T., Kanamori, K., Maeno, A., Kaji, H., Doherty, C. M., Falcaro, P., and Nakanishi, K., 2016, “Transparent, Highly Insulating Polyethyl- and Polyvinylsilsesquioxane Aerogels: Mechanical Improvements by Vulcanization for Ambient Pressure Drying,” Chem. Mater., **28**(19), pp. 6860–6868.
[34] Hwang, S.-W., Jung, H.-H., Hyun, S.-H., and Ahn, Y.-S., 2007, “Effective Preparation of Crack-Free Silica Aerogels via Ambient Drying,” J. Sol-Gel Sci. Technol., **41**(2), pp. 139–146.
[35] Yang, G., Ning, T., Zhao, W., Deng, W., and Liu, X., 2017, “Robust Ambient Pressure Dried Polyimide Aerogels and Their Graphene Oxide Directed Growth of 1D–2D Nanohybrid Aerogels Using Water as the Only Solvent,” RSC Adv., **7**(26), pp. 16210–16216.
[36] Koebel, M. M., Huber, L., Zhao, S., and Malfait, W. J., 2016, “Breakthroughs in Cost-Effective, Scalable Production of Superinsulating, Ambient-Dried Silica Aerogel and Silica-Biopolymer Hybrid Aerogels: From Laboratory to Pilot Scale,” J. Sol-Gel Sci. Technol., **79**(2), pp. 308–318.
[37] “Aerogel Technologies, LLC | Our Company,” Aerogel Technol. [Online]. Available: http://www.aerogeltechnologies.com/about/our-company/.
[38] Liu, Y., Zhao, Y., and Feng, X., 2008, “Exergy Analysis for a Freeze-Drying Process,” Appl. Therm. Eng., **28**(7), pp. 675–690.
[39] Degn Egeberg, E., and Engell, J., 1989, “Freeze Drying of Silica Gels Prepared from Siliciumethoxid,” J. Phys. Colloq., **24**(C4), pp. C4-23-C4-28.
[40] Simón-Herrero, C., Caminero-Huertas, S., Romero, A., Valverde, J. L., and Sánchez-Silva, L., 2016, “Effects of Freeze-Drying Conditions on Aerogel Properties,” J. Mater. Sci., **51**(19), pp. 8977–8985.
[41] Ciftci, D., Ubeyitogullari, A., Huerta, R. R., Ciftci, O. N., Flores, R. A., and Saldaña, M. D. A., 2017, “Lupin Hull Cellulose Nanofiber Aerogel Preparation by Supercritical CO_2 and Freeze Drying,” J. Supercrit. Fluids, **127**, pp. 137–145.
[42] Wang, T., Sun, H., Long, J., Wang, Y.-Z., and Schiraldi, D., 2016, “Biobased Poly(Furfuryl Alcohol)/Clay Aerogel Composite Prepared by a Freeze-Drying Process,” ACS Sustain. Chem. Eng., **4**(5), pp. 2601–2605.
[43] Mathieu, B., Blacher, S., Pirard, R., Pirard, J. P., Sahouli, B., and Brouers, F., 1997, “Freeze-Dried Resorcinol-Formaldehyde Gels,” J. Non-Cryst. Solids, **212**(2–3), pp. 250–261.
[44] Griffin, J. S., Mills, D. H., Cleary, M., Nelson, R., Manno, V. P., and Hodes, M., 2014, “Continuous Extraction Rate Measurements during Supercritical CO_2 Drying of Silica Alcogel,” J. Supercrit. Fluids, **94**, pp. 38–47.
[45] Kiran, E., Pöhler, H., and Xiong, Y., 1996, “Volumetric Properties of Pentane + Carbon Dioxide at High Pressures,” J. Chem. Eng. Data, **41**(2), pp. 158–165.
[46] Pöhler, H., and Kiran, E., 1997, “Volumetric Properties of Carbon Dioxide + Ethanol at High Pressures,” J. Chem. Eng. Data, **42**(2), pp. 384–388.
[47] Hekayati, J., Roosta, A., and Javanmardi, J., 2016, “Volumetric Properties of Supercritical Carbon Dioxide from Volume-Translated and Modified Peng-Robinson Equations of State,” Korean J. Chem. Eng., **33**(11), pp. 3231–3244.
[48] Wörmeyer, K., and Smirnova, I., 2013, “Adsorption of CO2, Moisture and Ethanol at Low Partial Pressure Using Aminofunctionalised Silica Aerogels,” Chem. Eng. J., **225**, pp. 350–357.

[49] Wörmeyer, K., and Smirnova, I., 2014, “Breakthrough Measurements of CO2 through Aminofunctionalised Aerogel Adsorbent at Low Partial Pressure: Experiment and Modeling,” Microporous Mesoporous Mater., **184**, pp. 61–69.
[50] García-González, C. A., Camino-Rey, M. C., Alnaief, M., Zetzl, C., and Smirnova, I., 2012, “Supercritical Drying of Aerogels Using CO_2: Effect of Extraction Time on the End Material Textural Properties,” J. Supercrit. Fluids, **66**, pp. 297–306.
[51] Selmer, I., Behnecke, A.-S., Farrell, P., Morales, A. B., Gurikov, P., and Smirnova, I., 2018, “Model Development for Sc-Drying Kinetics of Aerogels: Part 2. Packed Bed of Spherical Particles,” J. Supercrit. Fluids.
[52] Kocon, L., Despetis, F., and Phalippou, J., 1998, “Ultralow Density Silica Aerogels by Alcohol Supercritical Drying,” J. Non-Cryst. Solids, **225**, pp. 96–100.
[53] Sanz-Moral, L. M., Rueda, M., Mato, R., and Martín, Á., 2014, “View Cell Investigation of Silica Aerogels during Supercritical Drying: Analysis of Size Variation and Mass Transfer Mechanisms,” J. Supercrit. Fluids, **92**, pp. 24–30.
[54] Quiño, J., Ruehl, M., Klima, T., Ruiz, F., Will, S., and Braeuer, A., 2016, “Supercritical Drying of Aerogel: *In Situ* Analysis of Concentration Profiles inside the Gel and Derivation of the Effective Binary Diffusion Coefficient Using Raman Spectroscopy,” J. Supercrit. Fluids, **108**, pp. 1–12.
[55] 2019, *Inventory of U.S. Greenhouse Gas Emissions and Sinks 1990-2017*, EPA 430-R-19-001, United States Environmental Protection Agency.
[56] Caldeira, K., Jain, A. K., and Hoffert, M. I., 2003, “Climate Sensitivity Uncertainty and the Need for Energy Without CO_2 Emission,” Science, **299**(5615), pp. 2052–2054.
[57] Linneen, N., Pfeffer, R., and Lin, Y. S., 2013, “CO_2 Capture Using Particulate Silica Aerogel Immobilized with Tetraethylenepentamine,” Microporous Mesoporous Mater., **176**, pp. 123–131.
[58] Kong, Y., Jiang, G., Fan, M., Shen, X., Cui, S., and Russell, A. G., 2014, “A New Aerogel Based CO_2 Adsorbent Developed Using a Simple Sol–Gel Method along with Supercritical Drying,” Chem Commun, **50**(81), pp. 12158–12161.
[59] Yang, G., Luo, H., Ohba, T., and Kanoh, H., 2016, “CO_2 Capture by Carbon Aerogel–Potassium Carbonate Nanocomposites,” Int. J. Chem. Eng., **2016**, pp. 1–8.
[60] Anas, M., Unsal, S., and Erkey, C., 2017, “Investigation of Various Aerogels as Adsorbents for Methane Storage,” J. Supercrit. Fluids.
[61] Tian, T., Zeng, Z., Vulpe, D., Casco, M. E., Divitini, G., Midgley, P. A., Silvestre-Albero, J., Tan, J.-C., Moghadam, P. Z., and Fairen-Jimenez, D., 2017, “A Sol–Gel Monolithic Metal–Organic Framework with Enhanced Methane Uptake,” Nat. Mater., **17**(2), pp. 174–179.
[62] Economidou, M., Atanasiu, B., Despret, C., Maio, J., Nolte, I., and Rapf, O., 2011, *Europe’s Buildings Under the Microscope*, Buildings Performance Institute Europe.
[63] 2015, *Aerogel Market - Global Trends & Forecasts to 2019*, MarketsAndMarkets.
[64] 2018, *Insulation Market Size & Share Analysis Report By Product (Glass Wool, Mineral Wool, EPS, XPS), By Application (Residential Construction, Non-Residential Construction, Industrial, HVAC & OEM), And Segment Forecasts, 2018 - 2025*, Grand View Research.
[65] “Aerogel,” Cabot [Online]. Available: http://www.cabotcorp.com/solutions/products-plus/aerogel.

[66] "Industrial Insulation Products by Industry," Aspen Aerogels [Online]. Available: https://www.aerogel.com/products-and-solutions/overview/.
[67] Wasielewski, S. P., 2004, "Windows: Energy Efficiency Facts and Myths."
[68] Smith, D. M., Scherer, G. W., and Anderson, J. M., 1995, "Shrinkage during Drying of Silica Gel," J. Non-Cryst. Solids, **188**(3), pp. 191–206.
[69] Scherer, G. W., 1992, "Stress Development during Supercritical Drying," J. Non-Cryst. Solids, **145**, pp. 33–40.
[70] Scherer, G. W., 2019, "Stress and Strain during Supercritical Drying," J. Sol-Gel Sci. Technol., **90**(1), pp. 8–19.
[71] Helmchen, F., and Denk, W., 2005, "Deep Tissue Two-Photon Microscopy," Nat. Methods, **2**(12), pp. 932–940.
[72] Pawlicki, M., Collins, H. A., Denning, R. G., and Anderson, H. L., 2009, "Two-Photon Absorption and the Design of Two-Photon Dyes," Angew. Chem. Int. Ed., **48**(18), pp. 3244–3266.
[73] Wang, H., Zhang, R., Bridle, K. R., Jayachandran, A., Thomas, J. A., Zhang, W., Yuan, J., Xu, Z. P., Crawford, D. H. G., Liang, X., Liu, X., and Roberts, M. S., 2017, "Two-Photon Dual Imaging Platform for in Vivo Monitoring Cellular Oxidative Stress in Liver Injury," Sci. Rep., **7**, p. 45374.
[74] Durr, N. J., Larson, T., Smith, D. K., Korgel, B. A., Sokolov, K., and Ben-Yakar, A., 2007, "Two-Photon Luminescence Imaging of Cancer Cells Using Molecularly Targeted Gold Nanorods," Nano Lett., **7**(4), pp. 941–945.
[75] Wang, H., Huff, T. B., Zweifel, D. A., He, W., Low, P. S., Wei, A., and Cheng, J.-X., 2005, "In Vitro and in Vivo Two-Photon Luminescence Imaging of Single Gold Nanorods," Proc. Natl. Acad. Sci. U. S. A., **102**(44), pp. 15752–15756.
[76] Lillis, K. P., Eng, A., White, J. A., and Mertz, J., 2008, "Two-Photon Imaging of Spatially Extended Neuronal Network Dynamics with High Temporal Resolution," J. Neurosci. Methods, **172**(2), pp. 178–184.
[77] Fu, T., Tang, J., Chen, K., and Zhang, F., 2015, "Visible, near-Infrared and Infrared Optical Properties of Silica Aerogels," Infrared Phys. Technol., **71**, pp. 121–126.
[78] Hodak, J., Chen, Z., Wu, S., and Etchenique, R., 2016, "Multiphoton Excitation of Upconverting Nanoparticles in Pulsed Regime," Anal. Chem., **88**(2), pp. 1468–1475.
[79] Sorbello, C., and Etchenique, R., 2018, "Intrinsic Optical Sectioning with Upconverting Nanoparticles," Chem. Commun.
[80] Wang, F., and Liu, X., 2008, "Upconversion Multicolor Fine-Tuning: Visible to Near-Infrared Emission from Lanthanide-Doped $NaYF_4$ Nanoparticles," J. Am. Chem. Soc., **130**(17), pp. 5642–5643.
[81] Li, Z., and Zhang, Y., 2008, "An Efficient and User-Friendly Method for the Synthesis of Hexagonal-Phase $NaYF_4$:Yb, Er/Tm Nanocrystals with Controllable Shape and Upconversion Fluorescence," Nanotechnology, **19**(34), p. 345606.
[82] Shan, J., Kong, W., Wei, R., Yao, N., and Ju, Y., 2010, "An Investigation of the Thermal Sensitivity and Stability of the β-$NaYF_4$:Yb,Er Upconversion Nanophosphors," J. Appl. Phys., **107**(5), p. 054901.
[83] Li, D., Shao, Q., Dong, Y., and Jiang, J., 2014, "Anomalous Temperature-Dependent Upconversion Luminescence of Small-Sized $NaYF_4$:Yb^{3+}, Er^{3+} Nanoparticles," J. Phys. Chem. C, **118**(39), pp. 22807–22813.

[84] Yu, W., Xu, W., Song, H., and Zhang, S., 2014, "Temperature-Dependent Upconversion Luminescence and Dynamics of $NaYF_4$:Yb^{3+}/Er^{3+} Nanocrystals: Influence of Particle Size and Crystalline Phase," Dalton Trans, **43**(16), pp. 6139–6147.
[85] Klier, D. T., and Kumke, M. U., 2015, "Analysing the Effect of the Crystal Structure on Upconversion Luminescence in Yb^{3+},Er^{3+}-Co-Doped $NaYF_4$ Nanomaterials," J. Mater. Chem. C, **3**(42), pp. 11228–11238.
[86] Klier, D. T., and Kumke, M. U., 2015, "Upconversion Luminescence Properties of $NaYF_4$:Yb:Er Nanoparticles Codoped with Gd^{3+}," J. Phys. Chem. C, **119**(6), pp. 3363–3373.
[87] Chen, X., Zhou, D., Xu, W., Zhu, J., Pan, G., Yin, Z., Wang, H., Zhu, Y., Shaobo, C., and Song, H., 2017, "Fabrication of Au-Ag Nanocage@NaYF4@NaYF4:Yb,Er Core-Shell Hybrid and Its Tunable Upconversion Enhancement," Sci. Rep., **7**, p. 41079.
[88] Han, Q., Zhang, C., Wang, C., Wang, Z., Li, C., Gao, W., Dong, J., He, E., Zhang, Z., and Zheng, H., 2017, "Unique Adjustable UC Luminescence Pattern and Directional Radiation of Peculiar-Shaped NaYF4:Yb^{3+}/Er^{3+} Microcrystal Particle," Sci. Rep., **7**(1).
[89] Lei, P., An, R., Yao, S., Wang, Q., Dong, L., Xu, X., Du, K., Feng, J., and Zhang, H., 2017, "Ultrafast Synthesis of Novel Hexagonal Phase $NaBiF_4$ Upconversion Nanoparticles at Room Temperature," Adv. Mater., **29**(22), p. 1700505.
[90] Meyer, P., and Waas, A. M., 2015, "Measurement of In Situ-Full-Field Strain Maps on Ceramic Matrix Composites at Elevated Temperature Using Digital Image Correlation," Exp. Mech., **55**(5), pp. 795–802.
[91] Pan, B., Qian, K., Xie, H., and Asundi, A., 2009, "Two-Dimensional Digital Image Correlation for in-Plane Displacement and Strain Measurement: A Review," Meas. Sci. Technol., **20**(6), p. 062001.
[92] Pan, B., 2011, "Recent Progress in Digital Image Correlation," Exp. Mech., **51**(7), pp. 1223–1235.
[93] Smith, B. W., Li, X., and Tong, W., 1998, "Error Assessment for Strain Mapping by Digital Image Correlation," Exp. Tech., pp. 19–21.
[94] Franck, C., Hong, S., Maskarinec, S. A., Tirrell, D. A., and Ravichandran, G., 2007, "Three-Dimensional Full-Field Measurements of Large Deformations in Soft Materials Using Confocal Microscopy and Digital Volume Correlation," Exp. Mech., **47**(3), pp. 427–438.
[95] Refai, H. H., Petrich, E., Sluss Jr, J. J., Tull, M. P., Verma, P., Newman, G. K., and Dreyer, M., 2010, "Light Surface Display for Rendering a Three-Dimensional Image."
[96] Refai, H. H., and Sluss Jr, J. J., 2009, "Virtual Moving Screen for Rendering Three Dimensional Image."
[97] Soltan, P., Trias, J. A., Dahlke, W. J., Belfatto, R. V., and Sanzone, F., 1998, "Laser Based 3D Volumetric Display System."
[98] Marinov, V. R., Lima, Jr., I. T., and Miller, R., 2010, "Quantum Dot Dispersions in Aerogels: A New Material for True Volumetric Color Displays," Proc SPIE, **7690**, p. 76900X.
[99] Downing, E., Hesselink, L., Ralston, J., and MacFarlane, R. M., 1996, "A Three-Color, Solid-State, Three-Dimensional Display," Science, **273**, pp. 1185–1189.
[100] Kumagai, K., Hasegawa, S., and Hayasaki, Y., 2017, "Volumetric Bubble Display," Optica, **4**(3), p. 298.

[101] Zhu, B., Qian, B., Liu, Y., Xu, C., Liu, C., Chen, Q., Zhou, J., Liu, X., and Qiu, J., 2017, “A Volumetric Full-Color Display Realized by Frequency Upconversion of a Transparent Composite Incorporating Dispersed Nonlinear Optical Crystals,” NPG Asia Mater., **9**(6), p. e394.
[102] Smalley, D. E., Nygaard, E., Squire, K., Van Wagoner, J., Rasmussen, J., Gneiting, S., Qaderi, K., Goodsell, J., Rogers, W., Lindsey, M., Costner, K., Monk, A., Pearson, M., Haymore, B., and Peatross, J., 2018, “A Photophoretic-Trap Volumetric Display,” Nature, **553**, pp. 486–493.
[103] “Silica Aerogel (TMOS, Base-Catalyzed),” Aerogel.org [Online]. Available: http://www.aerogel.org/?p=1406.
[104] “Carbon Dioxide,” NIST Chem. WebBook SRD 69 [Online]. Available: https://webbook.nist.gov/cgi/cbook.cgi?ID=C124389&Mask=4#Thermo-Phase.
[105] “Supercritical Drying with Liquid Carbon Dioxide Part 2 of 2,” Aerogel.org [Online]. Available: http://www.aerogel.org/?p=1344.
[106] “Blackfly S USB3,” FLIR Syst. [Online]. Available: https://www.flir.com/products/blackfly-s-usb3?model=BFS-U3-51S5M-C.
[107] “Basler Ace AcA2040-90um - Area Scan Camera,” Basler [Online]. Available: https://www.baslerweb.com/en/products/cameras/area-scan-cameras/ace/aca2040-90um/.
[108] “Motion Control Software,” Thorlabs [Online]. Available: https://www.thorlabs.com/software_pages/ViewSoftwarePage.cfm?Code=Motion_Control&viewtab=0.
[109] “DSLR | EOS Rebel T5i 18-55mm IS STM Lens Kit,” Canon USA [Online]. Available: https://www.usa.canon.com/internet/portal/us/home/products/details/cameras/eos-dslr-and-mirrorless-cameras/dslr/eos-rebel-t5i-ef-s-18-55-is-stm-kit.
[110] Lay, A., Wang, D. S., Wisser, M. D., Mehlenbacher, R. D., Lin, Y., Goodman, M. B., Mao, W. L., and Dionne, J. A., 2017, “Upconverting Nanoparticles as Optical Sensors of Nano- to Micro-Newton Forces,” Nano Lett., **17**(7), pp. 4172–4177.
[111] Lei, J., Liu, Z., Yeo, J., and Ng, T. Y., 2013, “Determination of the Young’s Modulus of Silica Aerogels – an Analytical–Numerical Approach,” Soft Matter, **9**(47), p. 11367.
[112] Patil, S. P., Rege, A., Sagardas, Itskov, M., and Markert, B., 2017, “Mechanics of Nanostructured Porous Silica Aerogel Resulting from Molecular Dynamics Simulations,” J. Phys. Chem. B, **121**(22), pp. 5660–5668.
[113] Woignier, T., Reynes, J., Hafidi Alaoui, A., Beurroies, I., and Phalippou, J., 1998, “Different Kinds of Structure in Aerogels: Relationships with the Mechanical Properties,” J. Non-Cryst. Solids, **241**, pp. 45–52.
[114] Karadagli, I., Schulz, B., Schestakow, M., Milow, B., Gries, T., and Ratke, L., 2015, “Production of Porous Cellulose Aerogel Fibers by an Extrusion Process,” J. Supercrit. Fluids, **106**, pp. 105–114.
[115] Xu, X., Zhang, Q., Yu, Y., Chen, W., Hu, H., and Li, H., 2016, “Naturally Dried Graphene Aerogels with Superelasticity and Tunable Poisson’s Ratio,” Adv. Mater., **28**(41), pp. 9223–9230.
[116] Nguyen, B. N., Meador, M. A. B., Medoro, A., Arendt, V., Randall, J., McCorkle, L., and Shonkwiler, B., 2010, “Elastic Behavior of Methyltrimethoxysilane Based Aerogels Reinforced with Tri-Isocyanate,” ACS Appl. Mater. Interfaces, **2**(5), pp. 1430–1443.
[117] Randall, J. P., Meador, M. A. B., and Jana, S. C., 2011, “Tailoring Mechanical Properties of Aerogels for Aerospace Applications,” ACS Appl. Mater. Interfaces, **3**(3), pp. 613–626.

Appendix 1:

MATLAB Code

All MATLAB code was written using MATLAB R2018b running on a Windows 10 machine. Backwards-compatibility with older Windows machines should be possible (provided that the machine can run MATLAB), but compatibility with older versions of MATLAB is not guaranteed.

A1.1: Volumetric Scanning Protocol

The below code was used to perform volumetric scans through the monolith. Modifications to the scanning protocol allow for scans along only one or two axes, or for scanning different sizes of the volume.

```
clear; close all; clc;

%% Prepare stages for MATLAB control

% Load assemblies
fprintf('Loading assemblies.\n');
NET.addAssembly('C:\Program
Files\Thorlabs\Kinesis\Thorlabs.MotionControl.DeviceManagerCLI.dll');
```

```
NET.addAssembly('C:\Program
Files\Thorlabs\Kinesis\Thorlabs.MotionControl.GenericMotorCLI.dll');
NET.addAssembly('C:\Program
Files\Thorlabs\Kinesis\Thorlabs.MotionControl.KCube.DCServoCLI.dll');

% Initialize device list
import Thorlabs.MotionControl.DeviceManagerCLI.*
import Thorlabs.MotionControl.GenericMotorCLI.*
import Thorlabs.MotionControl.KCube.DCServoCLI.*

DeviceManagerCLI.BuildDeviceList();
DeviceManagerCLI.GetDeviceListSize();

serialX = '27252918'; % x-direction stage
serialY = '27252934'; % y-direction stage
serialZ = '27253232'; % z-direction stage

timeout = 60000; % time until time out [ms]

% Set up device and configuration
fprintf('Configuring stages.\n');
deviceX = KCubeDCServo.CreateKCubeDCServo(serialX); % create X device
deviceX.Connect(serialX); % connect with respective stage
deviceX.WaitForSettingsInitialized(5000); % wait 5 s for settings

deviceY = KCubeDCServo.CreateKCubeDCServo(serialY); % repeat for Y
deviceY.Connect(serialY);
deviceY.WaitForSettingsInitialized(5000);

deviceZ = KCubeDCServo.CreateKCubeDCServo(serialZ); % repeat for Z
deviceZ.Connect(serialZ);
deviceZ.WaitForSettingsInitialized(5000);

motorSettingsX = deviceX.LoadMotorConfiguration(serialX); % load motor config
motorSettingsX.DeviceSettingsName = 'PT1-Z8';
motorSettingsX.UpdateCurrentConfiguration(); % update the RealToDeviceUnit
converter

motorSettingsY = deviceY.LoadMotorConfiguration(serialY); % load motor config
motorSettingsY.DeviceSettingsName = 'PT1-Z8';
motorSettingsY.UpdateCurrentConfiguration(); % update the RealToDeviceUnit
converter

motorSettingsZ = deviceZ.LoadMotorConfiguration(serialZ); % load motor config
motorSettingsZ.DeviceSettingsName = 'PT1-Z8';
motorSettingsZ.UpdateCurrentConfiguration(); % update the RealToDeviceUnit
converter

MotorDeviceSettingsX = deviceX.MotorDeviceSettings; % push settings down to
device
deviceX.SetSettings(MotorDeviceSettingsX, true, false);

MotorDeviceSettingsY = deviceY.MotorDeviceSettings; % push settings down to
device
```

```
deviceY.SetSettings(MotorDeviceSettingsY, true, false);

MotorDeviceSettingsZ = deviceZ.MotorDeviceSettings; % push settings down to
device
deviceZ.SetSettings(MotorDeviceSettingsZ, true, false);

deviceX.StartPolling(250); % keep track of device, with delay
pause(1); % pause uses seconds as units?
deviceY.StartPolling(250); % this uses ms as units?
pause(1);
deviceZ.StartPolling(250);
pause(1);

% Home all devices
fprintf('Homing: X stage.\n');
deviceX.Home(timeout);
fprintf('X stage homed.\n');

fprintf('Homing: Y stage.\n');
deviceY.Home(timeout);
fprintf('Y stage homed.\n');

fprintf('Homing: Z stage.\n');
deviceZ.Home(timeout);
fprintf('Z stage homed.\n');

%% Set the positions for the stages
centerx = 15.5; centery = 6.5; centerz = 12; % coords for center [mm]
rangexy = 2.0; % define +/- about the center [mm]
    % make sure that center +/- range <= 25 mm
rangez = 2.0; % define +/- about the center [mm]

fprintf('\nCentering: [X, Y, Z] = [%d, %d, %d]
mm\n',centerx,centery,centerz);
deviceZ.MoveTo(centerz,0);
deviceY.MoveTo(centery,0);
deviceX.MoveTo(centerx,timeout); % move xyz simul
    % by setting quicker devices to 0 and slower device to timeout
    % change which devices move and in what order, based on timing
fprintf('Monolith is centered.\n');
pause(1); % 1 s delay to give time to complete movements

posx = [linspace(centerx-rangexy,centerx+rangexy,15)]'; % front to back
posy = [linspace(centery-rangexy,centery+rangexy,15)]'; % front to back
posz = [linspace(centerz-rangez,centerz+rangez,15)]'; % top to bottom
    % this should encompass the entire thickness of the monolith,
    % with points roughly 0.1 mm apart

%% Connect Arduino
ard1 = arduino('COM6','Uno'); % identify the proper Arduino board
fprintf('\nArduino connected.\n');
pause(1); % pause for 1 s just to make sure everything is set

%% Move the stages and trigger camera with Arduino (Z Scan)
tv01 = 0; % initialize counting variable
```

```
% Move the stages (use loops)
tv02 = length(posz); % total number of positions
fprintf('\nTotal number of positions: %d\n',tv02);

%{
fprintf('\nCentering: [X, Y, Z] = [%d, %d, %d]
mm\n',centerx,centery,centerz);
deviceZ.MoveTo(centerz,timeout);
deviceY.MoveTo(centery,timeout);
deviceX.MoveTo(centerx,timeout); % move xyz simul
    % by setting quicker devices to 0 and slower device to timeout
    % change which devices move and in what order, based on timing
fprintf('Monolith is centered.\n');
pause(1); % 1 s delay to give time to complete movements
%}

tic
for k = 1:length(posz) % move in z direction
    fprintf('\nMoving stages:\n');
    deviceZ.MoveTo(posz(k),timeout); % move z stage
    fprintf('Z stage moved to %d mm.\n',posz(k));

    for j = 1:length(posy) % move in y direction
        deviceY.MoveTo(posy(j),timeout); % move y stage
        fprintf('Y stage moved to %d mm.\n',posy(j));

        for i = 1:length(posx) % move in x direction
            tv01 = tv01 + 1; % iterate counting variable
            deviceX.MoveTo(posx(i),timeout); % move x stage
            fprintf('X stage moved to %d mm.\n',posx(i));

            for m = 1 % take one image per location
                writeDigitalPin(ard1,'D13',1); % set digital pin 13 to high
for LED
                writeDigitalPin(ard1,'D4',1); % set digital pin 4 to high for
camera
                pause(0.05); % wait 0.05 s
                writeDigitalPin(ard1,'D13',0); % set digital pin 13 to low
for LED
                writeDigitalPin(ard1,'D4',0); % set digital pin 4 to low for
camera
                pause(0.01); % wait 0.01 s (sync total pause time with exp
time)
            end

            fprintf('Images taken at position %d [%d,%d,%d]
mm.\n',tv01,posx(i),posy(j),posz(k));
            pause(0.05); % wait 0.05 s
        end
    end
end
toc

%% End the program and disconnect the stages/Arduino
```

```
clear ard1;
fprintf('\nArduino disconnected.\n');

fprintf('\nHoming: X stage.\n');
deviceX.MoveTo(0,timeout); % move to 0 mm before homing (saves time)
deviceX.Home(timeout);
fprintf('X stage homed.\n');
deviceX.StopPolling(); deviceX.Disconnect();
fprintf('X stage disconnected.\n');

fprintf('\nHoming: Y stage.\n');
deviceY.MoveTo(0,timeout); % move to 0 mm before homing (saves time)
deviceY.Home(timeout);
fprintf('Y stage homed.\n');
deviceY.StopPolling(); deviceY.Disconnect();
fprintf('Y stage disconnected.\n');

fprintf('\nHoming: Z stage.\n');
deviceZ.MoveTo(0,timeout); % move to 0 mm before homing (saves time)
deviceZ.Home(timeout);
fprintf('Z stage homed.\n');
deviceZ.StopPolling(); deviceZ.Disconnect();
fprintf('Z stage disconnected.\n');

fprintf('\nProgram is finished.\n');
```

A1.2: Analysis of Microparticle Fluorescence

The images of microparticle fluorescence shown in Fig. 6.2 were analyzed by treating all pixel values greater than a certain threshold as "not a number" values. Then the NaN values were ignored to plot the intensity of the fluorescence.

```
clear; close all; clc;
%% Create length scale, misc., etc.
x_length = 25; % roughly 25 mm long; this is for disks (blocks ~ 29 mm?)
tv00 = 1; % create iterative variable that represents figure number
%% Load images - Sonicated disk, 1% loading (0.01 mg/mL)
Sonic = imread('Sonic.CR2'); % read in RGB image
Sonic_bg = imread('Sonic_bg.CR2'); % read in bg image
Sonic_laser = Sonic(:,:,2) - Sonic_bg(:,:,2); % select only green light
    % and subtract bg from original (ideally, there is only laser now)
figure(tv00); tv00 = tv00 + 1; % figure(1)
imshow(Sonic_laser); % show image with most bg light removed
title('Laser Fluorescence (Background Removed) - Sonicated Disk');
```

```
%% Replace every value except the fluorescence with NaN
tv_thres = 130; % set threshold value
figure(tv00); tv00 = tv00 + 1; % figure(3)
imshow(Sonic_laser); % show image with most bg light removed
zoom(10) % set zoom factor, zoom in on fluorescence
% saveas(gcf, 'Zoom.tiff')

[tv_r,tv_c] = size(Sonic_laser); % get size of image
% for i =
tv_double = double(Sonic_laser); % convert from uint8 to double
tv_double(tv_double < tv_thres) = NaN; % overwrite all values
    % less than threshold, redefine as Not a Number
figure(tv00); tv00 = tv00 + 1; % figure(4)
tv_temp = uint8(tv_double); % temp convert to uint8 for plotting
imshow(tv_temp); % show image with most pixels replaced with NaN
tv_NaN = mean(tv_double, 'omitnan'); % average over columns while
    % omitting/ignoring NaN
Sonic_laser_NaN = tv_NaN(~isnan(tv_NaN))'; % take all values that are
xlength_NaN = linspace(0,x_length,length(Sonic_laser_NaN))';
figure(tv00); tv00 = tv00 + 1; % figure(5)
plot(xlength_NaN, Sonic_laser_NaN, 'b.-')
xlabel('Length [mm]'); ylabel('Intensity [arbitrary]');
% saveas(gcf, 'Sonic.tiff')

[tv01, tv_gof] =
fit(log(xlength_NaN(10:end)),log(Sonic_laser_NaN(10:end)),'poly1');
% linear fit to logarithm, avoid Inf by ignoring first 10 points
A_Sonic = exp(tv01(0)); b_Sonic = tv01(1)-tv01(0); % A = exp(p2) % b = p1
best_Sonic = A_Sonic*xlength_NaN.^b_Sonic; % define best fit power law
figure(tv00); tv00 = tv00 + 1; % figure(6)
plot(xlength_NaN, Sonic_laser_NaN, 'b.-'); hold on; % plot IP of beam
plot(xlength_NaN, best_Sonic, 'k'); % plot best fit
xlabel('Length [mm]'); ylabel('Intensity [arbitrary]');
ylim([0 255])
legend('Intensity Profile','Best Fit Power Law','Location','south')
% saveas(gcf, 'Sonic.tiff')
saveas(gcf, 'UseThis.tiff')

tv_gof
A_Sonic, b_Sonic
```

A1.3: Reading Images

The following code reads the images into MATLAB and allows for analysis. It allows for averaging of repeated images at the same position.

```
function [mean_test1] = readimages(tv_test1imgs,num_pos,num_abc)
%readimages Reads images and averages iterations for analysis
%   Inputs:
%       num_pos         number of distinct positions
%       num_abc         number of iterations of the same position
%       tv_test1imgs    root name of files to be read
%   Outputs:
%       mean_test1      stores values of mean images and associated names
%                       (might want to rename them instead of default)
%                       col1: mean; col2: names; col3: std (might as well)
%
num_total = num_pos*num_abc; % total number of images in this set
imgname_test1 = cell(1,num_total); % initialize size; holds names of images
tv_holdimage = cell(size(imgname_test1)); % temporarily holds images after
    % they are read by imread
tv_double = tv_holdimage; % stores images after being converted to double
for i = 1:num_total % this loads the names to prep for reading
    if i <= 9 % for the future, make a separate array holding the number
        tv_garbage = sprintf('%s000%d',tv_test1imgs,i);
        imgname_test1{i} = tv_garbage; % holds first 9 names
    elseif (10 <= i) && (i <= 99)
        tv_garbage = sprintf('%s00%d',tv_test1imgs,i);
        imgname_test1{i} = tv_garbage; % holds names 10 up to 99
    elseif (100 <= i) && (i <= 999)
        tv_garbage = sprintf('%s0%d',tv_test1imgs,i);
        imgname_test1{i} = tv_garbage; % holds names 100 up to 999
    else
        tv_garbage = sprintf('%s%d',tv_test1imgs,i);
        imgname_test1{i} = tv_garbage; % holds names 1000 up to 9999
    end % the naming scheme is _0001 through _2000+, so this is needed
    tv_holdimage{i} = imread(imgname_test1{i},'tiff'); % reads images
    tv_double{i} = double(tv_holdimage{i}); % convert from uint16 to double
        % calculations are better in double
end
fprintf('Finished reading images.\n');
tv_double = reshape(tv_double,num_abc,num_pos)'; % reshape cell array
    % group [abc] together across columns to prep for averaging
tv_matrix = cell(1,num_pos)'; % holds cell array for matrix conversion
tv_mean = tv_matrix; % holds mean of pixels of images
tv_std = tv_matrix; % holds std of pixels of images
mean_test1 = cell(3,num_pos)'; % stores values of mean images
    % and associated names (might want to rename them instead of default)
    % col 1: mean; col 2: names; col 3: std (might as well)
for i = 1:num_pos % iterate over number of distinct positions
    tv_matrix{i} = cat(3, tv_double{i,:}); % convert cell array to matrix
        % stores all [abc] together as a 3D matrix in one cell per matrix
```

```
    tv_mean{i} = mean(tv_matrix{i}, 3); % calc mean of pixels of images
    mean_test1{i,1} = uint16(tv_mean{i}); % first column stores means
        % convert from double to uint16; plotting is better (?)
    tv_std{i} = std(tv_matrix{i}, [], 3); % calc std of pixels of images
    mean_test1{i,3} = uint16(tv_std{i}); % third column stores stds
        % convert from double to uint16; plotting is better (?)
end
fprintf('Finished averaging images.\n');
% if I want to keep the default names:
tv_z = 0; % temp vari; initialize iterative variable
for i = 1:num_abc:length(imgname_test1) % choose every third name
    tv_z = tv_z + 1; % iterate index of mean_load0
    mean_test1{tv_z,2} = imgname_test1{i}(1:end); % no '.tiff'
        % store truncated names in second column of mean_load0
end
% if I want to change the names to match the positions:
for i = 1:num_pos
    mean_test1{i,2} = sprintf('test_pos%d',i); % consider changing this
        % to match the [xyz] positions
end


end
```

A1.4: Voxel Intensity Analysis: Slicing Method

The “slicing” technique referenced in Ch. 6.2.3 identified the brightest pixel in a given image, then took a horizontal “slice” across the image to create an intensity profile. That intensity profile was integrated to create a single value representing the voxel.

```
function [IPx_test1] = makeIPcuts(mean_test1,mywinsize,myprofwidth)
%makeIPcuts Horizontal slices for analysis
%   Inputs:
%       mean_test1      stores values of mean images and associated names
%                       (might want to rename them instead of default)
%                       col1: mean; col2: names; col3: std (might as well)
%       mywinsize       zoom window half-width [pixels]
%       myprofwidth     half-width of intensity profile 'cut'
%   Outputs:
%       IPx_test1       intensity profiles cut in x-axis
%       IPy_test1       intensity profiles cut in y-axis
%                       (isn't generally needed for my analysis)
%
y_peakloc = cell(1,size(mean_test1,1))'; % initialize cell array (column)
    % this holds the y location of the peak intensity spot
```

```
x_peakloc = y_peakloc; % this holds the x location
maxint = y_peakloc; % this holds the value of the max/peak intensity
IPy_test1 = y_peakloc; % this holds the intensity profiles cut in y-axis
IPx_test1 = IPy_test1; % this holds the intensity profiles cut in x-axis
for i = 1:length(mean_test1)
% for i = 1:length(y_peakloc) % iterate over number of mean images
    % find location of max of each image, i.e., peak of intensity spot
    [y_peakloc{i}, x_peakloc{i}] = ...
        find(mean_test1{i,1} == max(mean_test1{i,1}(:)),1);
    % find value of peak intensity
    maxint{i} = mean_test1{i,1}(y_peakloc{i}, x_peakloc{i});
    % create x intensity profile for each image through maximum
    tv_x = mean_test1{i,1}(y_peakloc{i} - myprofwidth:y_peakloc{i} ...
        + myprofwidth, x_peakloc{i} - mywinsize:x_peakloc{i} + mywinsize);
    IPx_test1{i} = mean(tv_x,1)';
    % create y intensity profile for each image through maximum
    tv_y = mean_test1{i,1}(y_peakloc{i} - mywinsize:y_peakloc{i} ...
        + mywinsize, x_peakloc{i}-myprofwidth:x_peakloc{i}+myprofwidth);
    IPy_test1{i} = mean(tv_y,2);
end
fprintf('Finished intensity profile cuts.\n');

end
```

A1.5: Voxel Intensity Analysis: Gaussian Method

The “Gaussian” analysis technique identified the brightest pixel of the image, took a horizontal slice to create an intensity profile, then fit a Gaussian curve to the profile. The peak of the Gaussian was identified and treated as the singular value representing the voxel.

```
function [peak_Gauss,std_x] = peakGauss(mean_test1,mywinsize,myprofwidth)
%peakGauss Fits a Gaussian over a data set, then outputs the value of
%           the peak of the fit
%   Inputs:
%       mean_test1      stores values of mean images and associated names
%                       (might want to rename them instead of default)
%                       col1: mean; col2: names; col3: std (might as well)
%       mywinsize       zoom window half-width [pixels]
%       myprofwidth     half-width of intensity profile 'cut'
%   Outputs:
%       peak_Gauss    value of peak of Gaussian fit
%       std_x           value of standard deviation in x
%
y_peakloc = zeros(1,size(mean_test1,1))'; % initialize array (column)
    % this holds the y location of the peak intensity spot (one per image)
```

```
x_peakloc = y_peakloc; % this holds the x location
maxint = y_peakloc; % this holds the value of the max/peak intensity

IPy_test1 = cell(1,size(mean_test1,1))'; % this holds the intensity profiles
cut in y-axis
IPx_test1 = IPy_test1; % this holds the intensity profiles cut in x-axis
gauss_x = IPy_test1; gauss_y = IPy_test1; gauss_x_coeff = IPy_test1;
std_x = gauss_x;
peak_Gauss = IPy_test1; % this holds the value of peak of 2D Gaussian fit
tv_box = cell(1,size(mean_test1,1))'; % box centered around peak
for i = 1:length(mean_test1)
    % find location of max of each image, i.e., peak of intensity spot
    tv_meantest1 = mean_test1{i,1};
    [y_peakloc(i), x_peakloc(i)] = ...
        find(tv_meantest1 == max(tv_meantest1(:)),1);
    % find value of peak intensity
    maxint(i) = tv_meantest1(y_peakloc(i), x_peakloc(i));
    % isolate a box centered around the brightest pixel of the image
    tv_box{i} = tv_meantest1(y_peakloc(i) - myprofwidth:y_peakloc(i) ...
        + myprofwidth, x_peakloc(i) - mywinsize:x_peakloc(i) + mywinsize);
    % fit Gaussians
    % create x intensity profile for each image through maximum
    tv_x = tv_meantest1(y_peakloc(i), ...
        x_peakloc(i) - mywinsize:x_peakloc(i) + mywinsize);
    IPx_test1{i} = mean(tv_x,1)';
    % create y intensity profile for each image through maximum
    tv_y = tv_meantest1(y_peakloc(i) - myprofwidth:y_peakloc(i) ...
        + myprofwidth, x_peakloc(i));
    IPy_test1{i} = mean(tv_y,2);
    % fit gaussians
    tv_IPx = IPx_test1{i};
    gauss_x{i} = fit([-mywinsize:mywinsize]',tv_IPx,'gauss1');
    tv_IPy = IPy_test1{i};
    gauss_y{i} = fit([-myprofwidth:myprofwidth]',tv_IPy,'gauss1');
    tv_gaussx = gauss_x{i};
    gauss_x_coeff{i} = coeffvalues(tv_gaussx); % find coeff of gauss fit
    tv_gaussxcoeff = gauss_x_coeff{i};
    std_x{i} = tv_gaussxcoeff(3)/sqrt(2); % find std from coeff
    peak_Gauss{i} = tv_gaussxcoeff(1); % identify peak of fit
end
fprintf('Finished Gaussian fits.\n');

end
```

A1.6: Voxel Intensity Analysis: Boxing Method

The “boxing” technique identified the brightest pixel of the image, then summed all pixel values within a certain area of that brightest pixel. This summed value represented the voxel.

```
function [IPx_test1] = boxingint(mean_test1,mywinsize,myprofwidth)
%boxingint Sums intensity values around peak intensity pixel
%   Inputs:
%       mean_test1      stores values of mean images and associated names
%                       (might want to rename them instead of default)
%                       col1: mean; col2: names; col3: std (might as well)
%       mywinsize       zoom window half-width [pixels]
%       myprofwidth     half-width of intensity profile 'cut'
%   Outputs:
%       IPx_test1       intensity profiles cut in x-axis
%       IPy_test1       intensity profiles cut in y-axis
%                       (isn't generally needed for my analysis)
%
y_peakloc = cell(1,size(mean_test1,1))'; % initialize cell array (column)
    % this holds the y location of the peak intensity spot
x_peakloc = y_peakloc; % this holds the x location
maxint = y_peakloc; % this holds the value of the max/peak intensity
IPy_test1 = y_peakloc; % this holds the intensity profiles cut in y-axis
IPx_test1 = IPy_test1; % this holds the intensity profiles cut in x-axis
for i = 1:length(mean_test1)
    % find location of max of each image, i.e., peak of intensity spot
    [y_peakloc{i}, x_peakloc{i}] = ...
        find(mean_test1{i,1} == max(mean_test1{i,1}(:)),1);
    % find value of peak intensity
    maxint{i} = mean_test1{i,1}(y_peakloc{i}, x_peakloc{i});
    % sum all values of image in rectangle around peak
    tv_x = mean_test1{i,1}(y_peakloc{i} - myprofwidth:y_peakloc{i} ...
        + myprofwidth, x_peakloc{i} - mywinsize:x_peakloc{i} + mywinsize);
    IPx_test1{i} = sum(sum(tv_x));
end
fprintf('Finished intensity profile cuts.\n');

end
```

A1.7: Analysis of Volume Scans

The following code analyzes the images taken to produce Fig. 6.11. It then plots the data in a 3D scatterplot and creates slices through the scatterplot.

```
clear; clc; close all;
tv00 = 1; % initialize figure iterative variable
folder = fileparts(which(mfilename)); % IDs name and location of this file
addpath(genpath(folder)); % adds location and all subfolders to path
%% Read images and make intensity profile cuts
sidelength = 15; % length of one side
num_pos = 3375; % number of distinct positions
num_abc = 1; % number of iterations of the same position
num_total = num_pos*num_abc; % total number of images in this set
% num_load = 4; % number of distinct loading levels
    % num_load might be defined down below as well, so remember to comment
    % out the below code if num_load is defined up here
mywinsize = 30; % zoom window half-width [pixels]
myprofwidth = 10; % half-width of intensity profile 'cut'

% Test 2
tic
fprintf('Begin analysis of Test 2 images.\n');
tv_test2imgs = 'Basler_acA2040-90um__21775167__20190719_144204422_';
[mean_test2] = readimages(tv_test2imgs,num_pos,num_abc);
    % read and average images together
[IPx_test2] = windowint(mean_test2,mywinsize,myprofwidth);
    % make intensity profile cuts in x-direction
fprintf('Finished analysis of Test 2 images.\n\n');
save('fifteencubed.mat','mean_test2','IPx_test2'); % save analyzed images

load('fifteencubed.mat'); % load pre-analyzed images to save time
toc

tv_15cubed = reshape(IPx_test2,15,225)'; % make new array for calculations
IPx_15cubed = cellfun(@mean,tv_15cubed); % take mean of each IP cut
meanIP = mean(mean(IPx_15cubed)); % find mean intensity of entire gel
% save('IPx_15cubed.mat','IPx_15cubed')

%% Create 3D space of points
tv_points = linspace(-2,2,sidelength); % predefine this for later
tv_points1 = linspace(2,-2,sidelength); % predefine this for later

xyz_map = cell(length(IPx_15cubed(:,1)),1); % initialize
m = 1; % initialize
for j = 1:sidelength % count along z
    for i = 1:sidelength % count along y
        xyz_map{m} = [tv_points;
            linspace(tv_points1(i),tv_points1(i),sidelength);
            linspace(tv_points1(j),tv_points1(j),sidelength)];
```

```
        m = m + 1; % iterate
    end
end

%% 3D Plots
figure(tv00); tv00 = tv00 + 1;
myscale = 300; % scaling variable
for i = 1:length(IPx_15cubed(:,1))
    scatter3(xyz_map{i}(1,:), xyz_map{i}(2,:), xyz_map{i}(3,:),...
        myscale*IPx_15cubed(i,:)/meanIP, IPx_15cubed(i,:)/meanIP, 'filled')
    hold on
end
colormap(jet)
xlabel('X [mm]'); ylabel('Y [mm]'); zlabel('Z [mm]');
% title('15^3 Volumetric Scan of Monolith')
daspect([1 1 1]); colorbar

% saveas(gcf, 'MeanIP_VolumScan_15cubed.jpg')

%% 3D Slices
A = reshape(IPx_15cubed',[15 15 15])/meanIP; % columns for x
[X,Y,Z] = meshgrid(linspace(-2,2,15)); % just a guess

xslice = linspace(-2,2,15);
yslice = linspace(2,-2,15);
zslice = linspace(2,-2,15);

for i = 1:length(xslice)
figure(tv00); tv00 = tv00 + 1;
    h = slice(X,Y,Z,A,xslice(end),yslice(i),zslice(end));
    daspect([1 1 1]); colormap(jet)
xlabel('Y [mm]'); ylabel('X [mm]'); zlabel('Z [mm]');
    colorbar
    set(h,'edgecolor','none')
% tv_text1 = sprintf('Appendix_VolSlices%d.jpg',i);
% saveas(gcf, tv_text1)
end
```

Appendix 2:

Dimensional Analysis

The dimensional analysis used to determine the relevant dimensionless variables for analyzing different aerogel formulations is given below. After identifying the dependent variable (volumetric strain) and all possible independent variables, the variables were rewritten to cancel out the dimensions, resulting in four relevant dimensionless variables (Poisson's ratio, particle number density, dimensionless particle radius, and dimensionless stress).

LMT: length (L), mass (M), and time (T) are the relevant dimensions

Dependent variable [dimensions in terms of length-mass-time]:

Volumetric strain e_v [ ]

Create a function where the nondimensionalized dependent variable is a function of nondimensionalized independent variables (e.g., $e_v = \Phi(\bar{A}, \bar{B}, \bar{C})$)

Independent variables [dimensions in terms of length-mass-time]:

Applied stress $\sigma\left[\frac{M}{LT^2}\right]$

Particle radius $r\ [L]$

Particle separation $\delta\ [L]$

Young's (matrix) $E\left[\frac{M}{LT^2}\right]$

Density (matrix) $\rho\left[\frac{M}{L^3}\right]$

Monolith height $h\,[L]$

Poisson's ratio $\nu\,[\,]$

Rewrite length-mass-time dimensions in terms of independent variables, cancelling out dimensions:

$$L = r$$

$$M = \rho r^3$$

$$T = r\left(\frac{\rho}{E}\right)^{\frac{1}{2}}$$

Rewrite all variables in terms of the new length-mass-time variables to nondimensionalize:

$$e_v \to already\ dimensionless$$

$$\bar{\sigma} = \frac{\sigma}{\rho r^3}\frac{r^3\rho}{E} = \frac{\sigma}{E}$$

$$\bar{r} = \frac{r}{r} = 1$$

$$\bar{\delta} = \frac{\delta}{r}$$

$$\bar{E} = \frac{E}{\rho r^3}\frac{r^3\rho}{E} = \frac{E}{E} = 1$$

$$\bar{\rho} = \frac{\rho}{\rho r^3}r^3 = 1$$

$$\bar{h} = \frac{h}{\delta}$$

$$\nu \to already\ dimensionless$$

Dependent variable (volumetric strain) as a function of independent variables:

$$e_v = \Phi\left(\bar{\sigma}, \bar{\delta}, \bar{h}\right)$$

$$\nu \to constant, won't\ change\ (so\ won't\ affect\ e_v)$$

$$e_v = \Phi\left(\frac{\sigma}{E}, \frac{\delta}{r}, \frac{h}{\delta}\right)$$

Hold $\frac{h}{\delta}$ constant for all simulations (constant particle number density, reflective of experiments).

Hold $\frac{\delta}{r}$ constant and vary $\frac{\sigma}{E}$, then change $\frac{\delta}{r}$ and vary $\frac{\sigma}{E}$ again.

Appendix 3:

Variability of Strain Experiments

The following figures show the variability within the monolith, based on position. 17 different positions within the monolith were imaged under strain, with the average of those images resulting in Fig. 6.8.

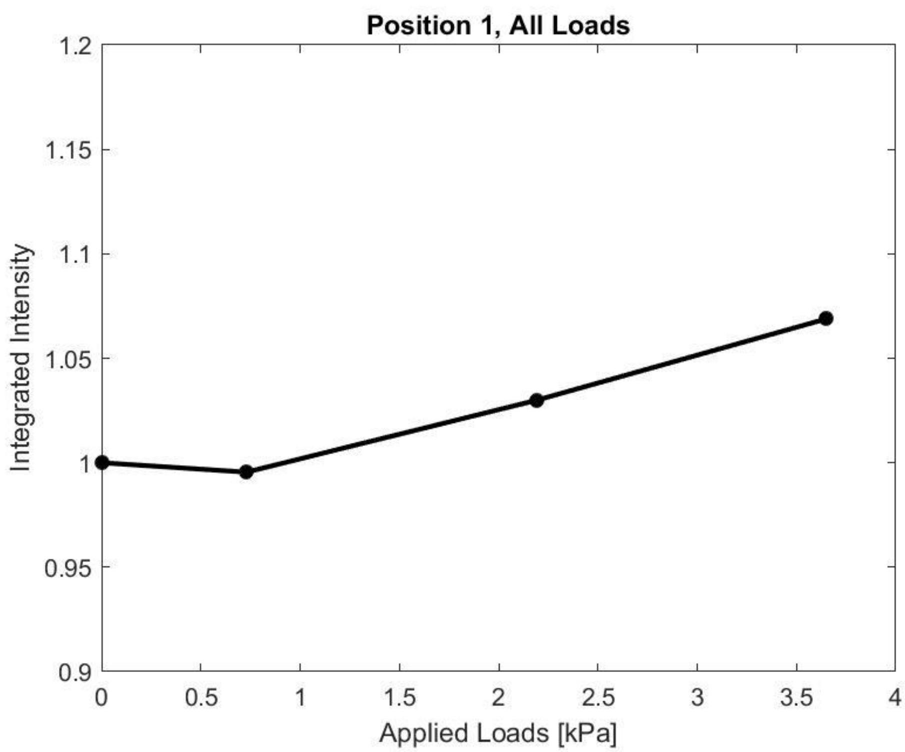

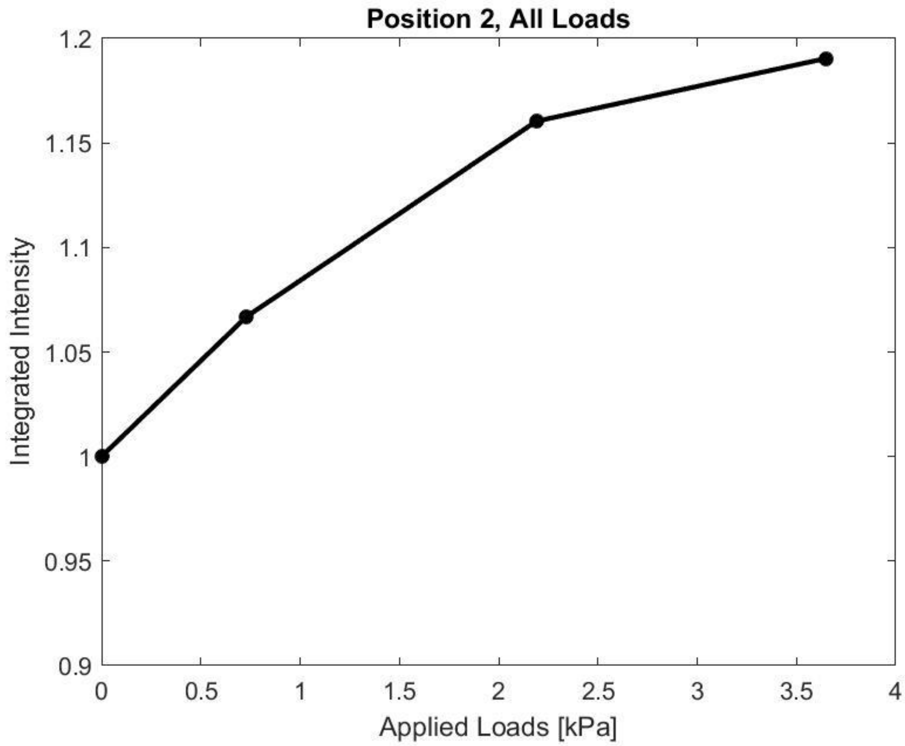
Position 2, All Loads
Integrated Intensity
Applied Loads [kPa]
1.2
1.15
1.1
1.05
1
0.95
0.9
0
0.5
1
1.5
2
2.5
3
3.5
4

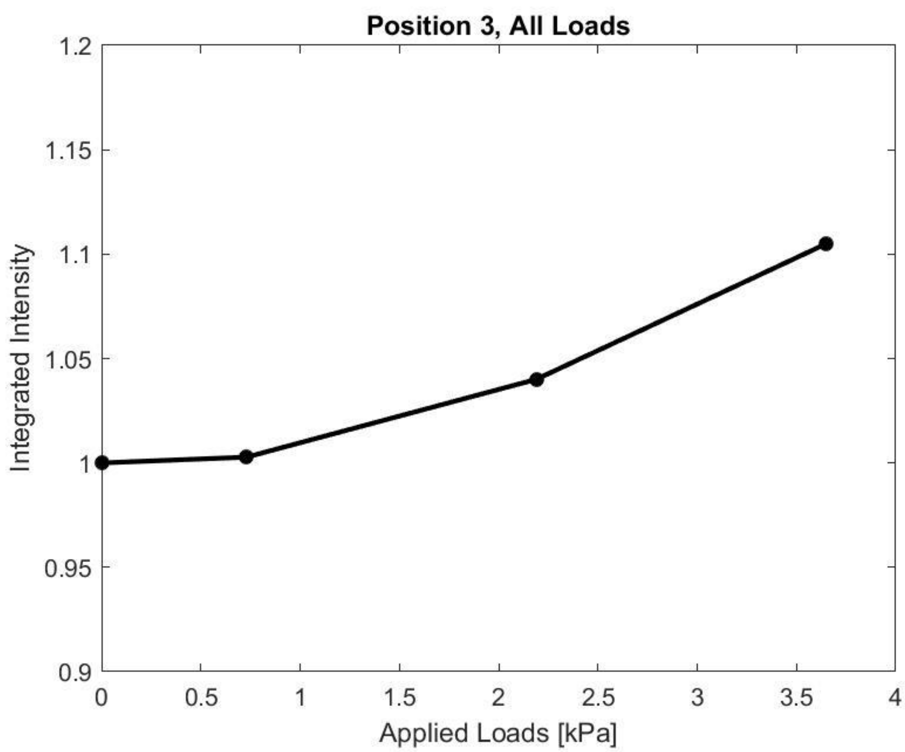
Position 3, All Loads
Integrated Intensity
Applied Loads [kPa]
1.2
1.15
1.1
1.05
1
0.95
0.9
0
0.5
1
1.5
2
2.5
3
3.5
4

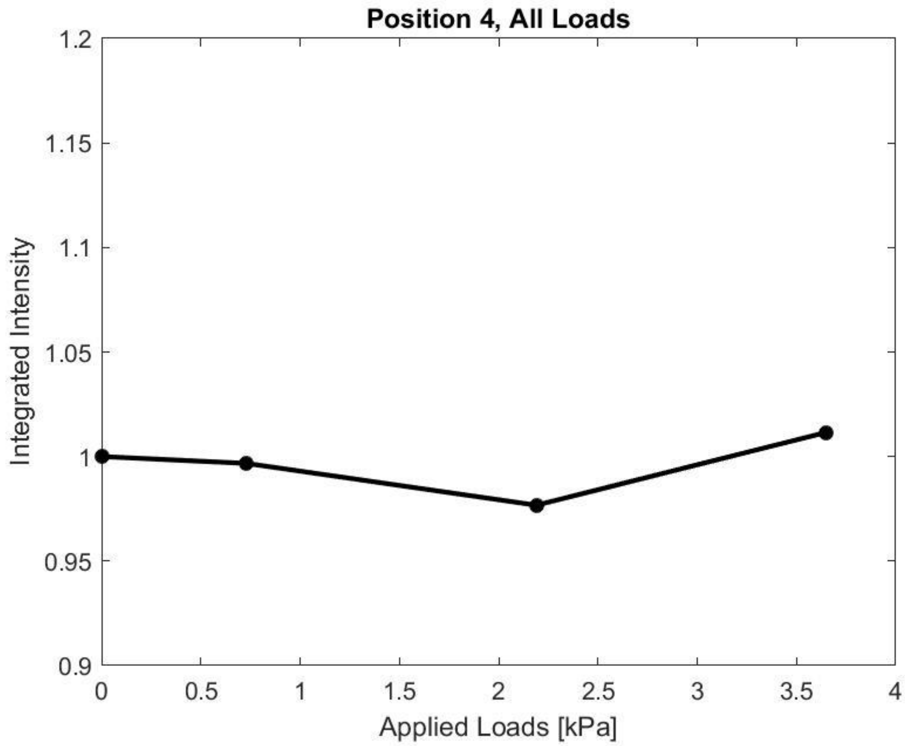
Position 4, All Loads
Integrated Intensity
Applied Loads [kPa]
1.2
1.15
1.1
1.05
1
0.95
0.9
0
0.5
1
1.5
2
2.5
3
3.5
4

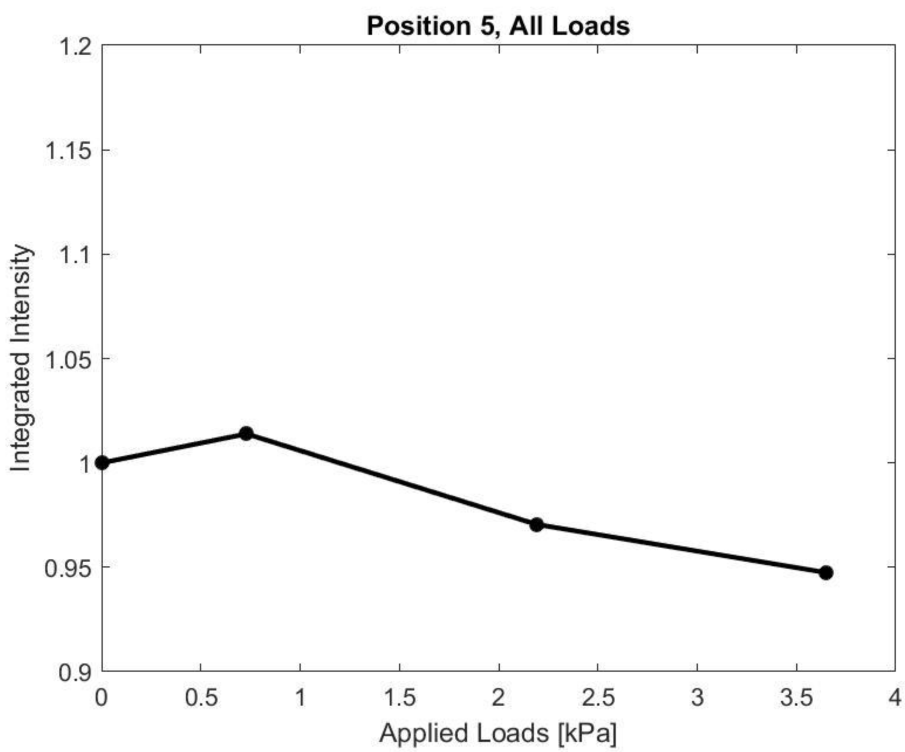
Position 5, All Loads
Integrated Intensity
Applied Loads [kPa]
1.2
1.15
1.1
1.05
1
0.95
0.9
0
0.5
1
1.5
2
2.5
3
3.5
4

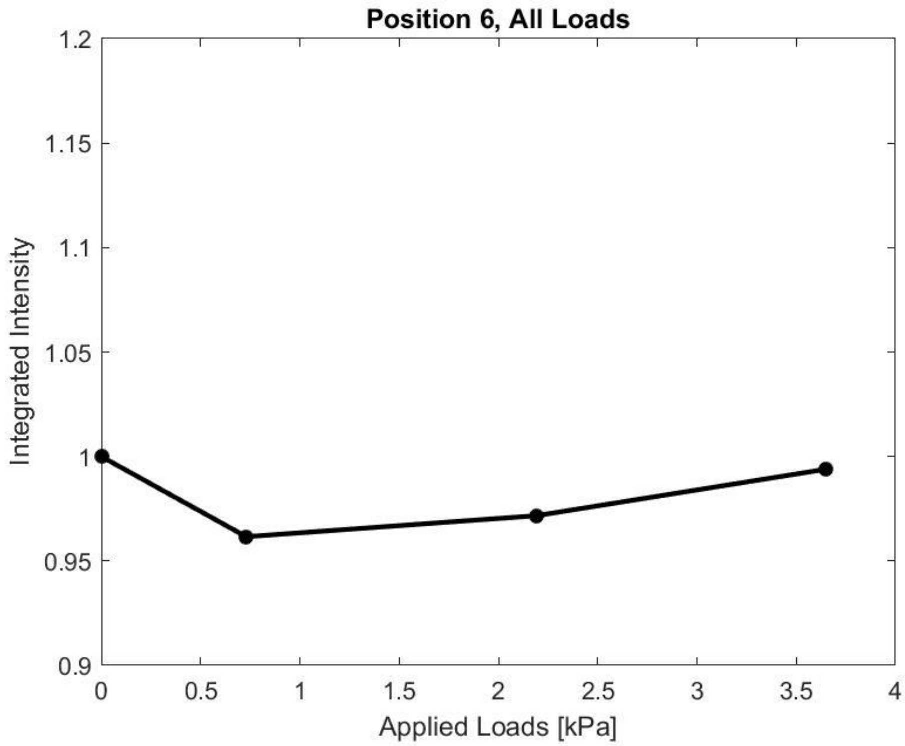
Position 6, All Loads
Integrated Intensity
Applied Loads [kPa]
1.2
1.15
1.1
1.05
1
0.95
0.9
0
0.5
1
1.5
2
2.5
3
3.5
4

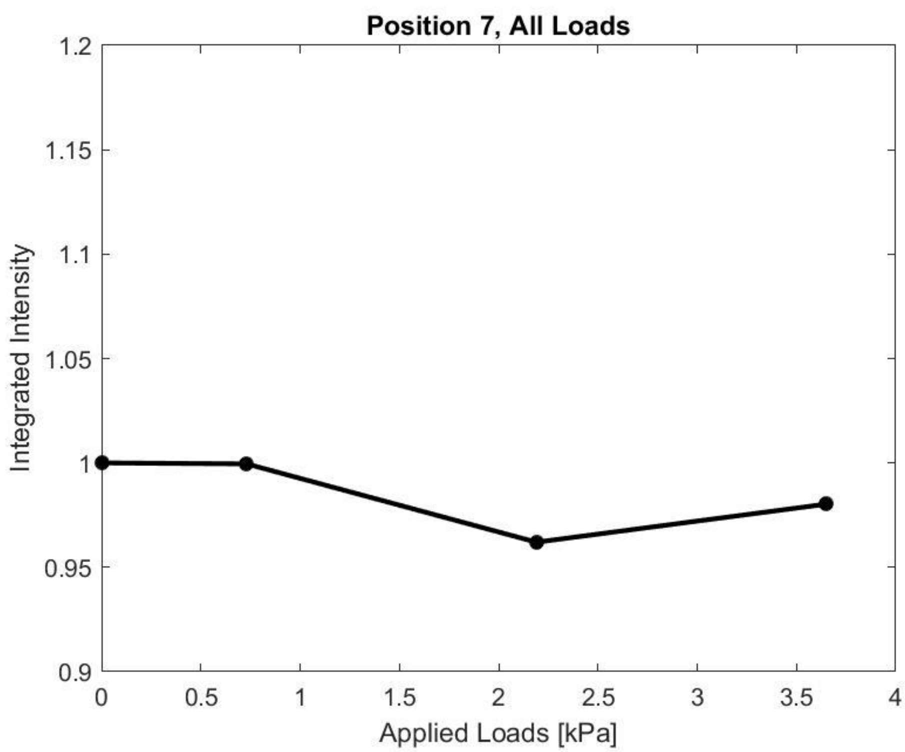
Position 7, All Loads
Integrated Intensity
Applied Loads [kPa]
1.2
1.15
1.1
1.05
1
0.95
0.9
0
0.5
1
1.5
2
2.5
3
3.5
4

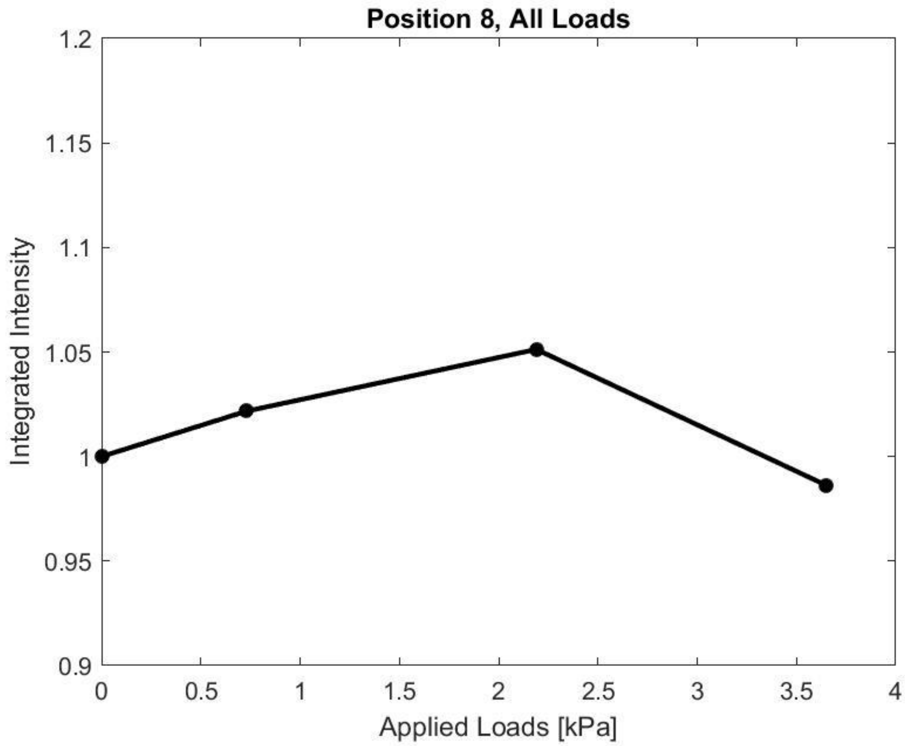
Position 8, All Loads
Integrated Intensity
Applied Loads [kPa]
1.2
1.15
1.1
1.05
1
0.95
0.9
0
0.5
1
1.5
2
2.5
3
3.5
4

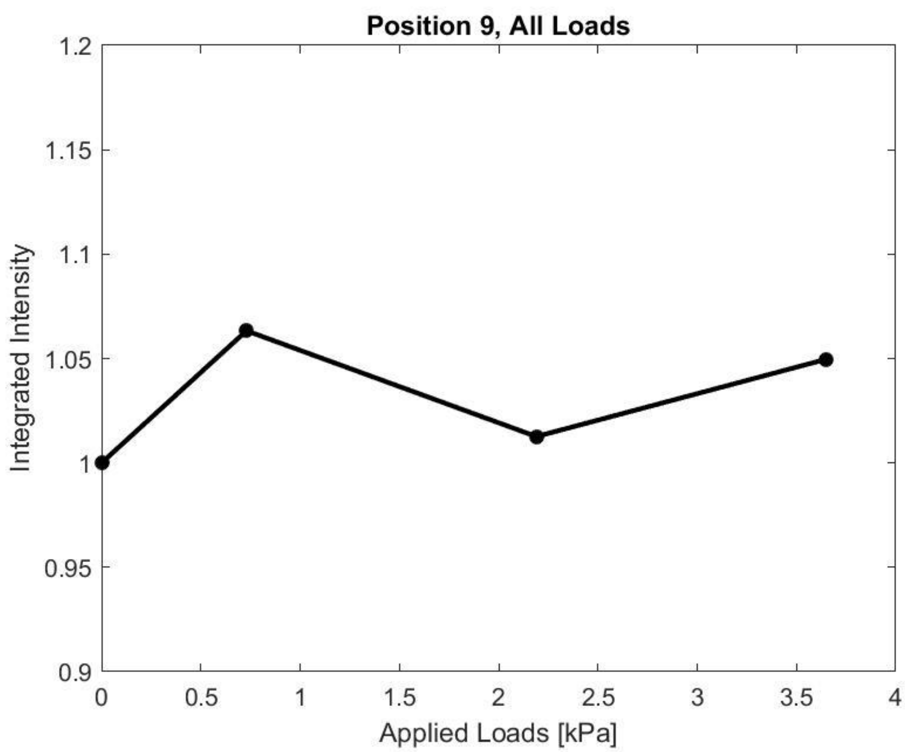
Position 9, All Loads
Integrated Intensity
Applied Loads [kPa]
1.2
1.15
1.1
1.05
1
0.95
0.9
0
0.5
1
1.5
2
2.5
3
3.5
4

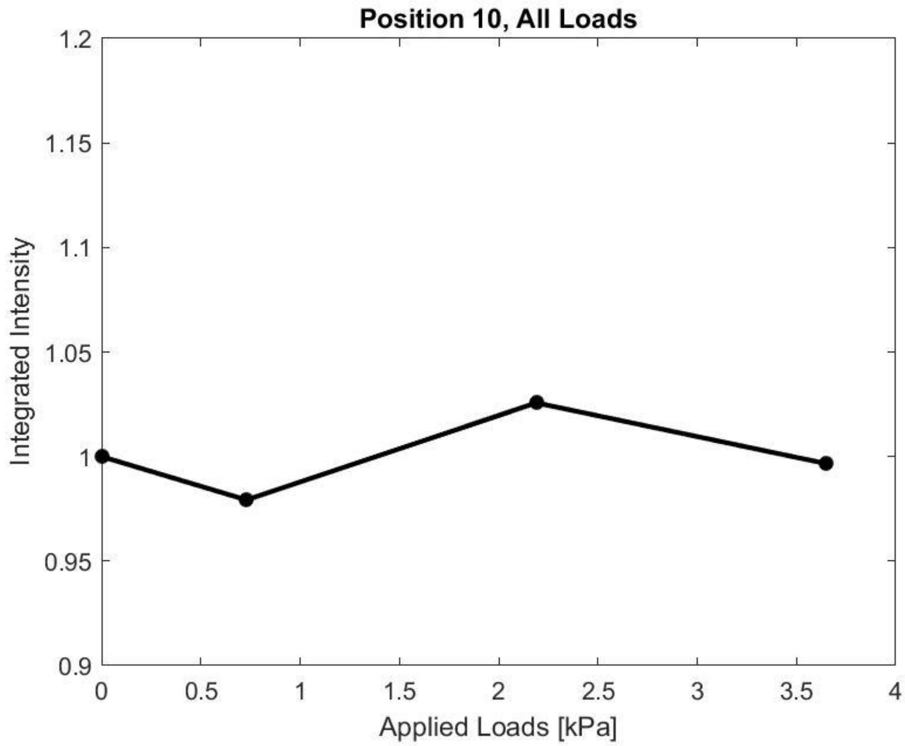
Position 10, All Loads
Integrated Intensity
Applied Loads [kPa]
1.2
1.15
1.1
1.05
1
0.95
0.9
0
0.5
1
1.5
2
2.5
3
3.5
4

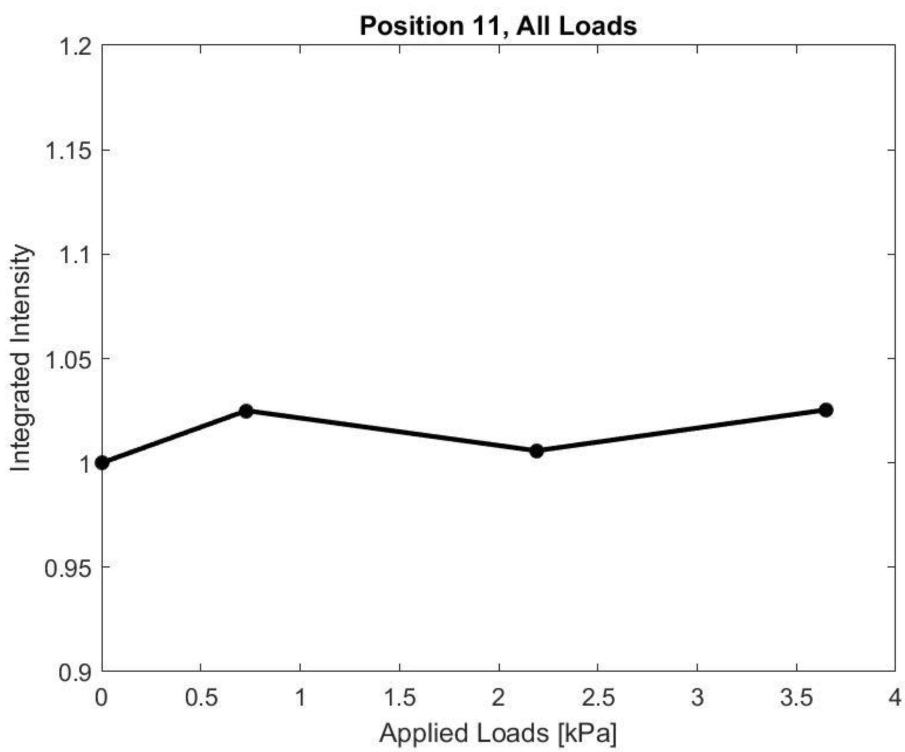
Position 11, All Loads
Integrated Intensity
Applied Loads [kPa]
1.2
1.15
1.1
1.05
1
0.95
0.9
0
0.5
1
1.5
2
2.5
3
3.5
4

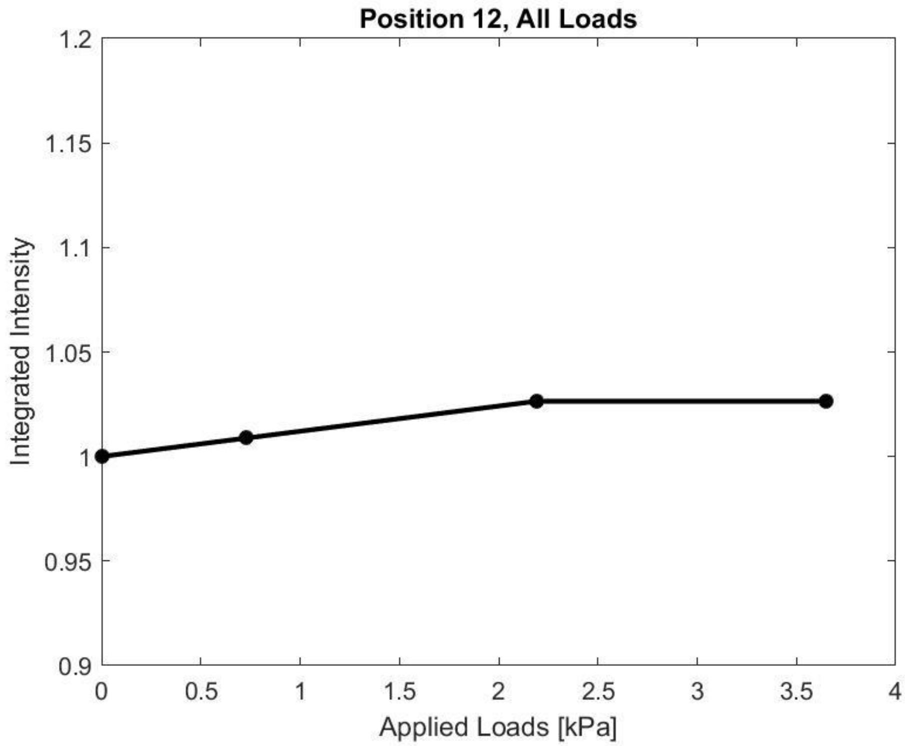
Position 12, All Loads
Integrated Intensity
Applied Loads [kPa]
1.2
1.15
1.1
1.05
1
0.95
0.9
0
0.5
1
1.5
2
2.5
3
3.5
4

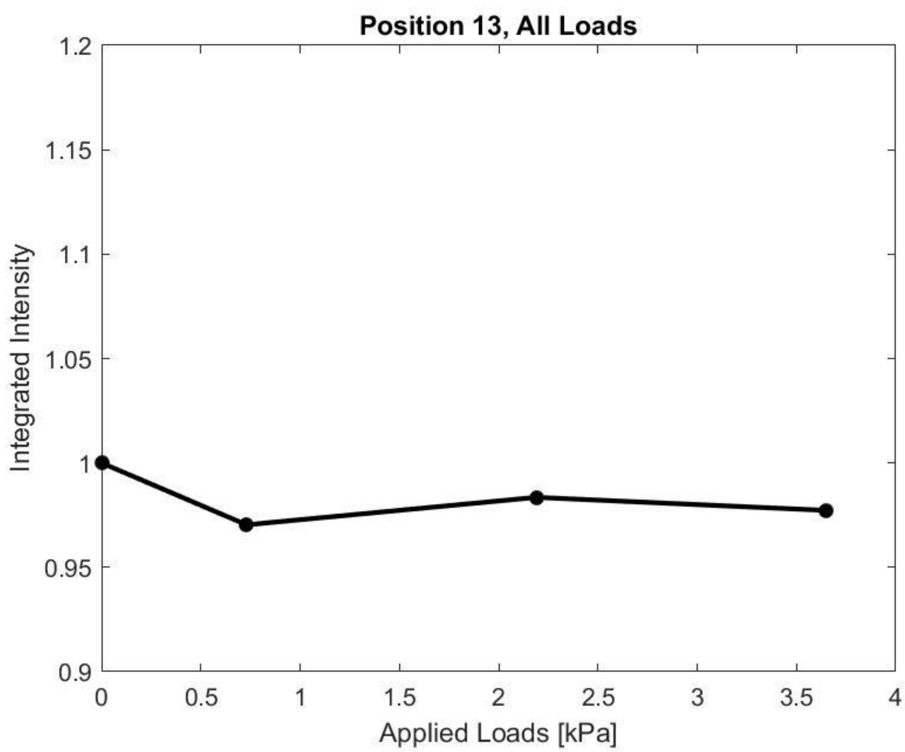
Position 13, All Loads
Integrated Intensity
Applied Loads [kPa]
1.2
1.15
1.1
1.05
1
0.95
0.9
0
0.5
1
1.5
2
2.5
3
3.5
4

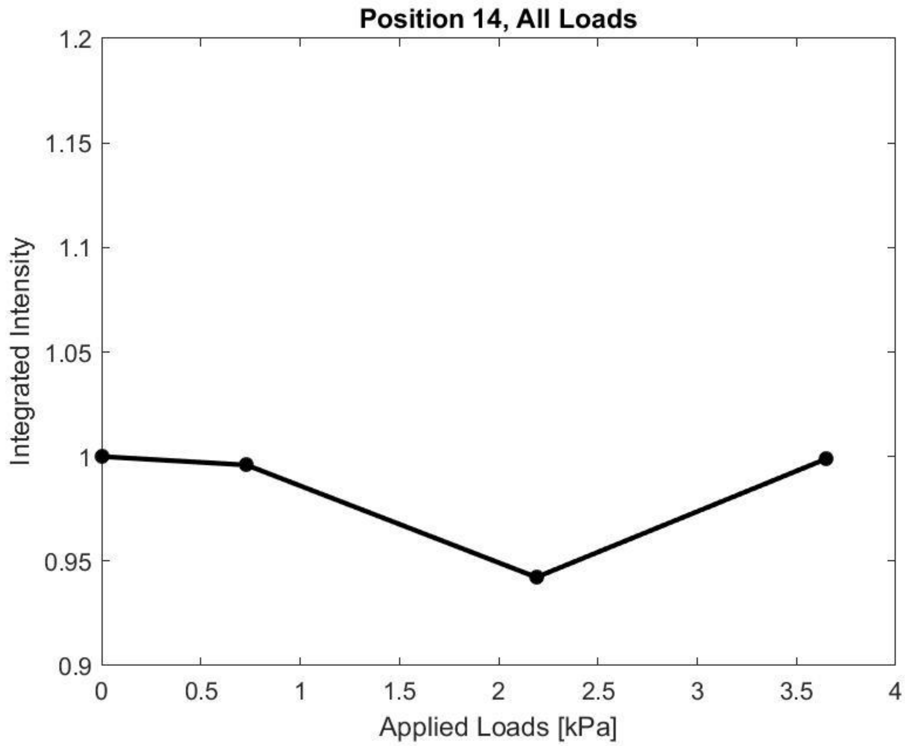
Position 14, All Loads
Integrated Intensity
Applied Loads [kPa]
1.2
1.15
1.1
1.05
1
0.95
0.9
0
0.5
1
1.5
2
2.5
3
3.5
4

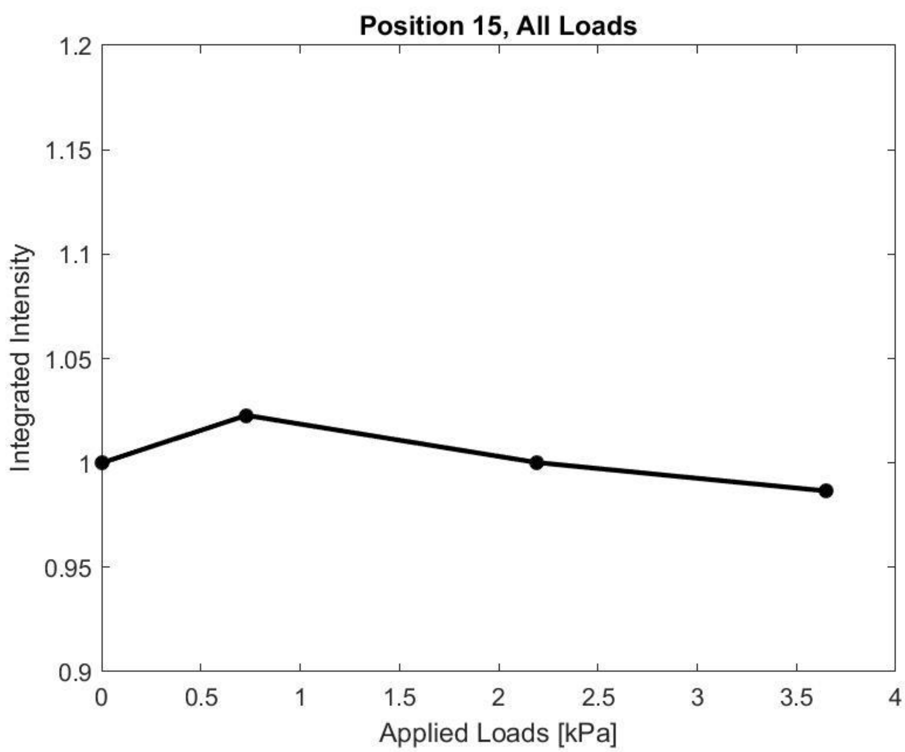
Position 15, All Loads
Integrated Intensity
Applied Loads [kPa]
1.2
1.15
1.1
1.05
1
0.95
0.9
0
0.5
1
1.5
2
2.5
3
3.5
4

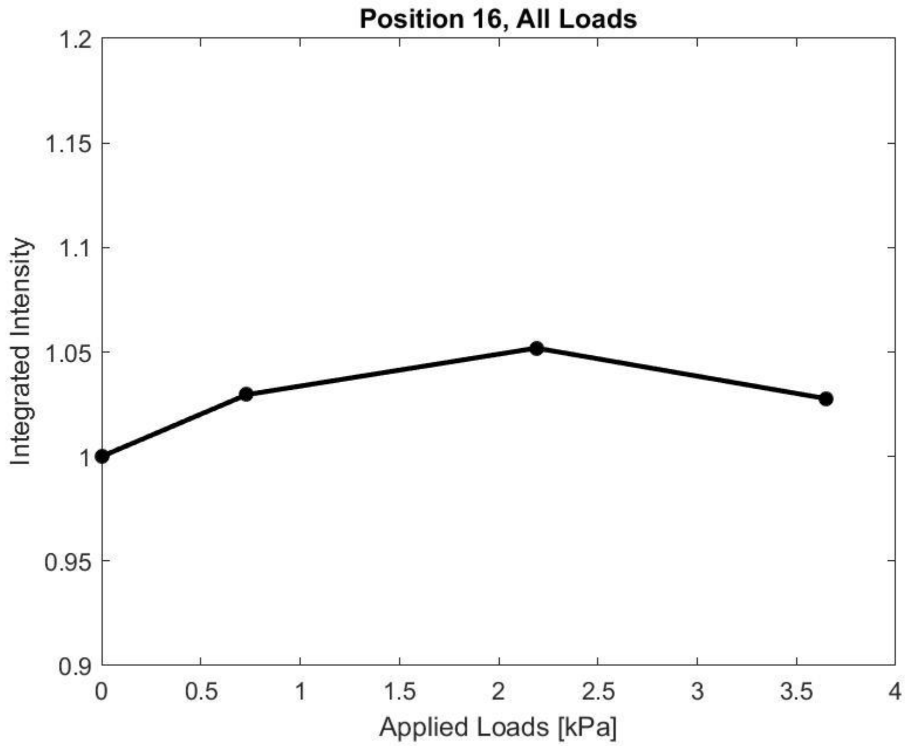
Position 16, All Loads
Integrated Intensity
Applied Loads [kPa]
1.2
1.15
1.1
1.05
1
0.95
0.9
0
0.5
1
1.5
2
2.5
3
3.5
4

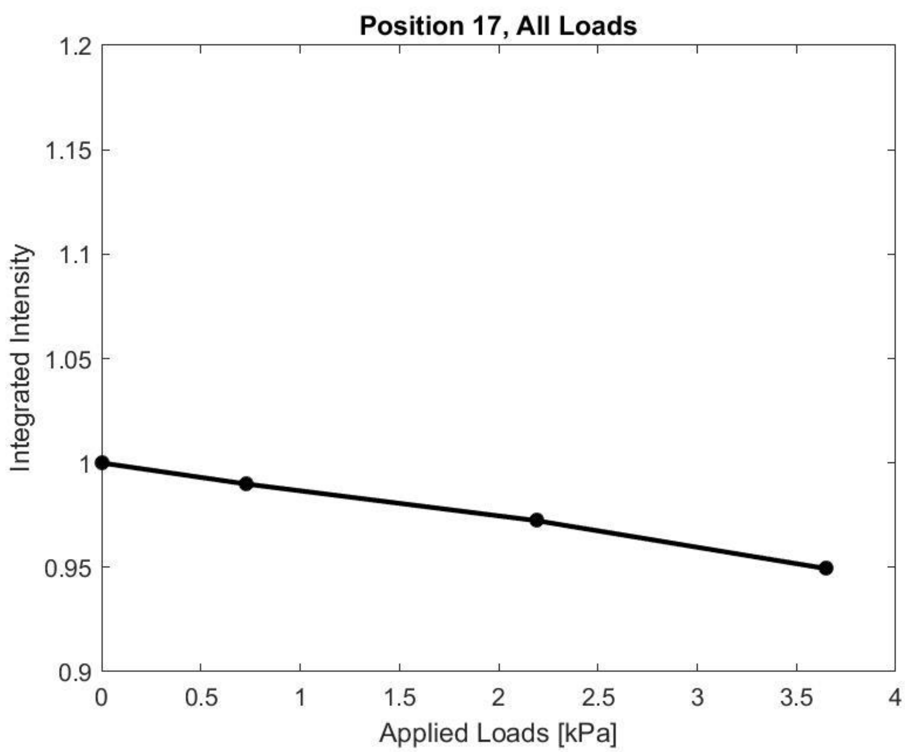
Position 17, All Loads
Integrated Intensity
Applied Loads [kPa]
1.2
1.15
1.1
1.05
1
0.95
0.9
0
0.5
1
1.5
2
2.5
3
3.5
4

Appendix 4:

Plane Slices of Volume Scans

The following figures show slices of the volume of Fig. 6.11. Each slice shows a different X position, with all points along the YZ plane visible.

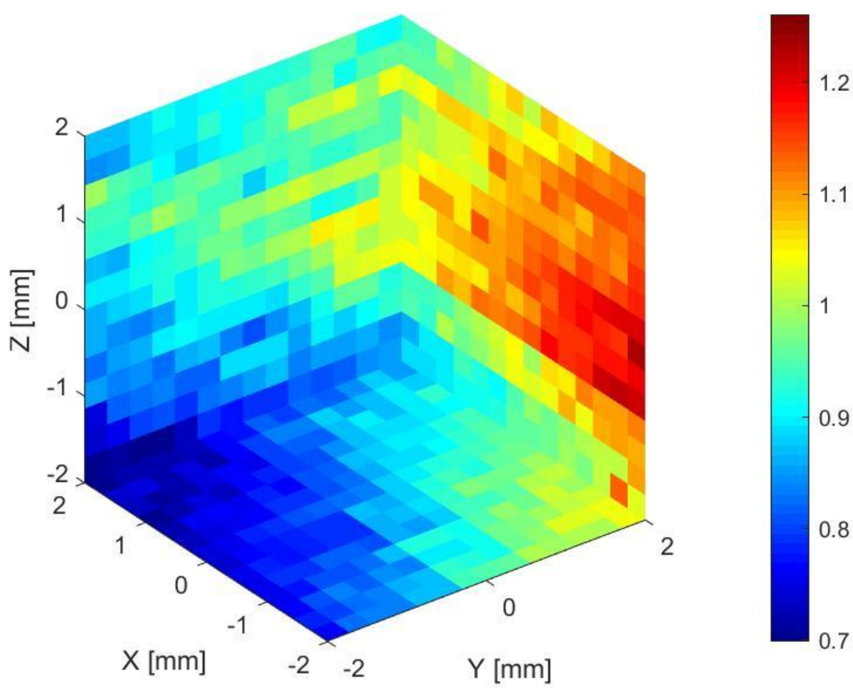

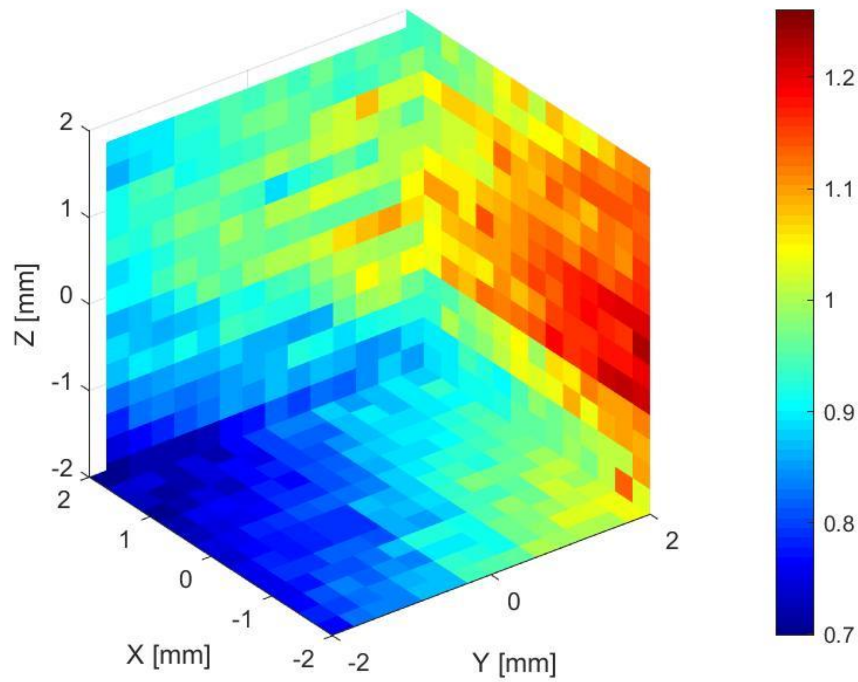

2
1
0
-1
-2
Z [mm]
2
1
0
-1
-2
X [mm]
-2
0
2
Y [mm]
1.2
1.1
1
0.9
0.8
0.7

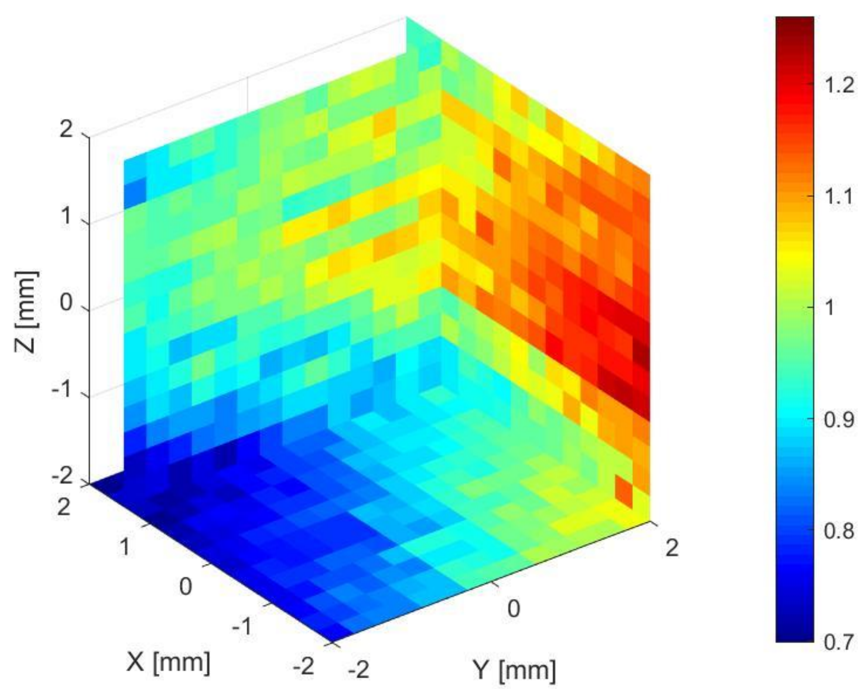

2
1
0
-1
-2
Z [mm]
2
1
0
-1
-2
X [mm]
-2
0
2
Y [mm]
1.2
1.1
1
0.9
0.8
0.7

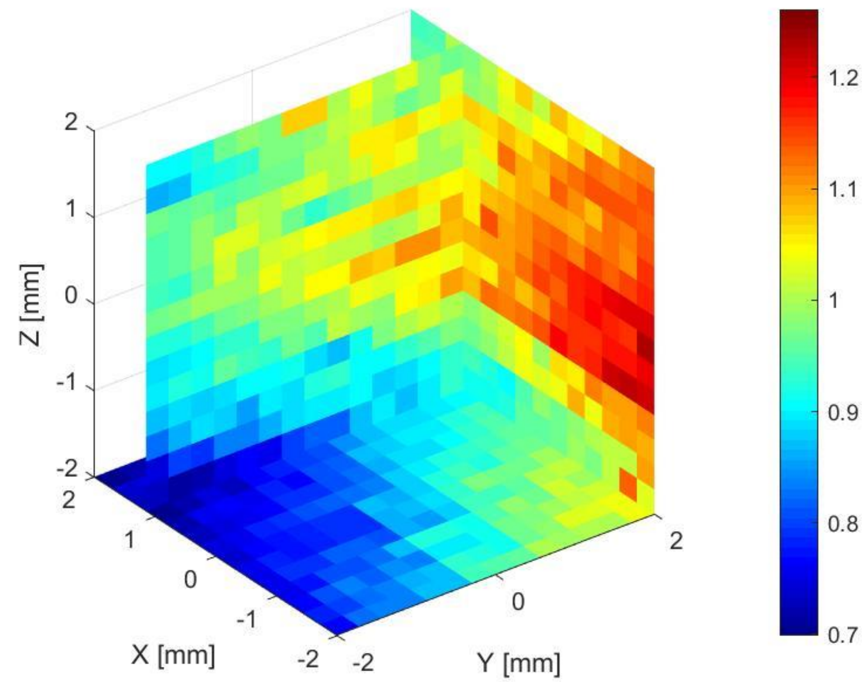
Z [mm]
2
1
0
-1
-2
X [mm]
2
1
0
-1
-2
Y [mm]
-2
0
2
1.2
1.1
1
0.9
0.8
0.7

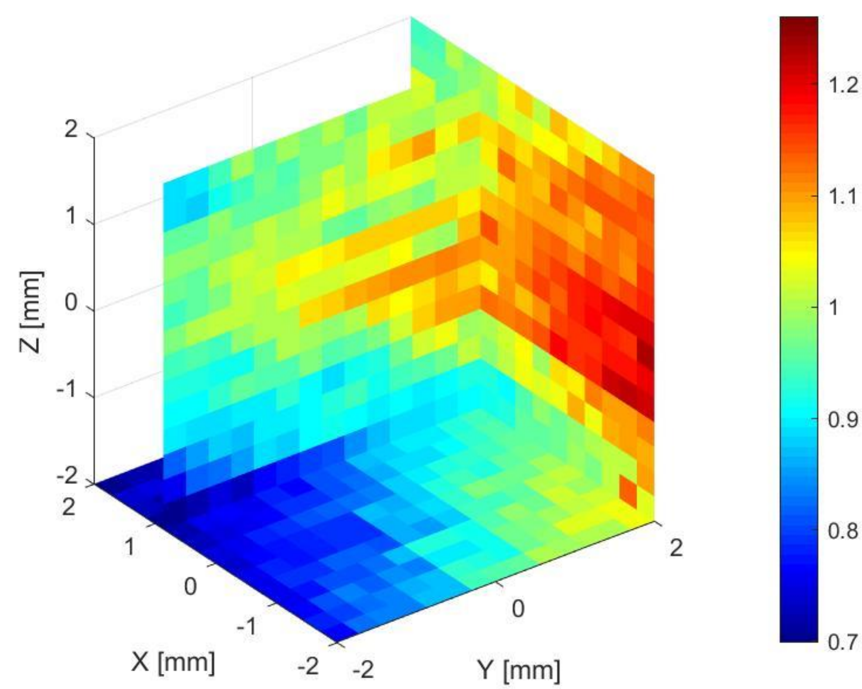
Z [mm]
2
1
0
-1
-2
X [mm]
2
1
0
-1
-2
Y [mm]
-2
0
2
1.2
1.1
1
0.9
0.8
0.7

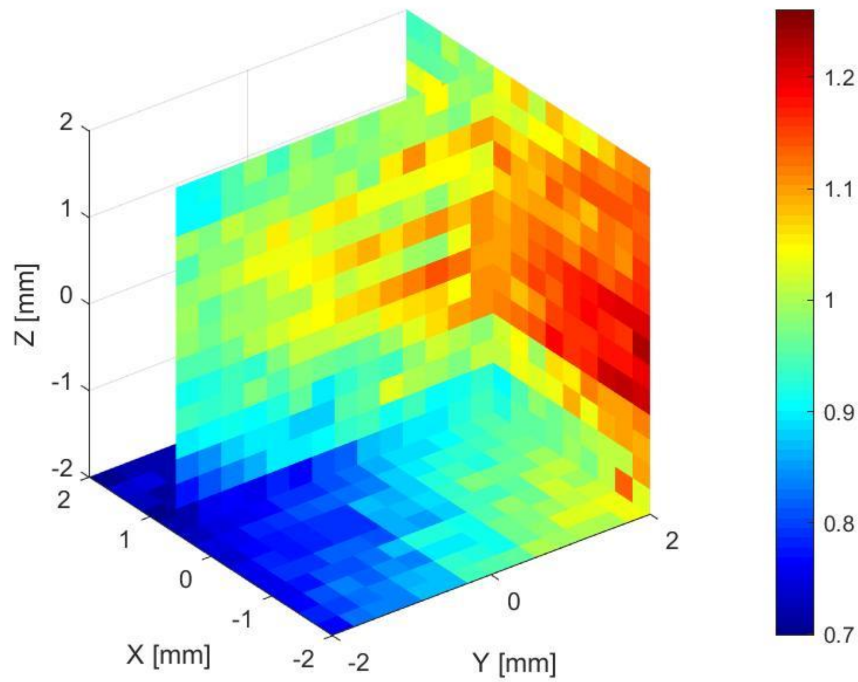

2
1
0
-1
-2
Z [mm]
2
1
0
-1
-2
X [mm]
-2
0
2
Y [mm]
1.2
1.1
1
0.9
0.8
0.7

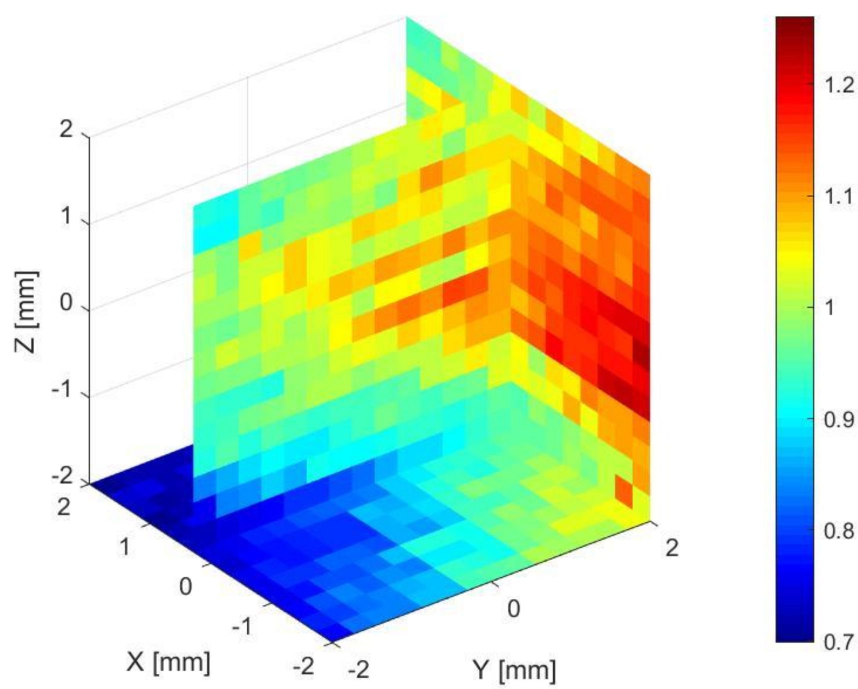

2
1
0
-1
-2
Z [mm]
2
1
0
-1
-2
X [mm]
-2
0
2
Y [mm]
1.2
1.1
1
0.9
0.8
0.7

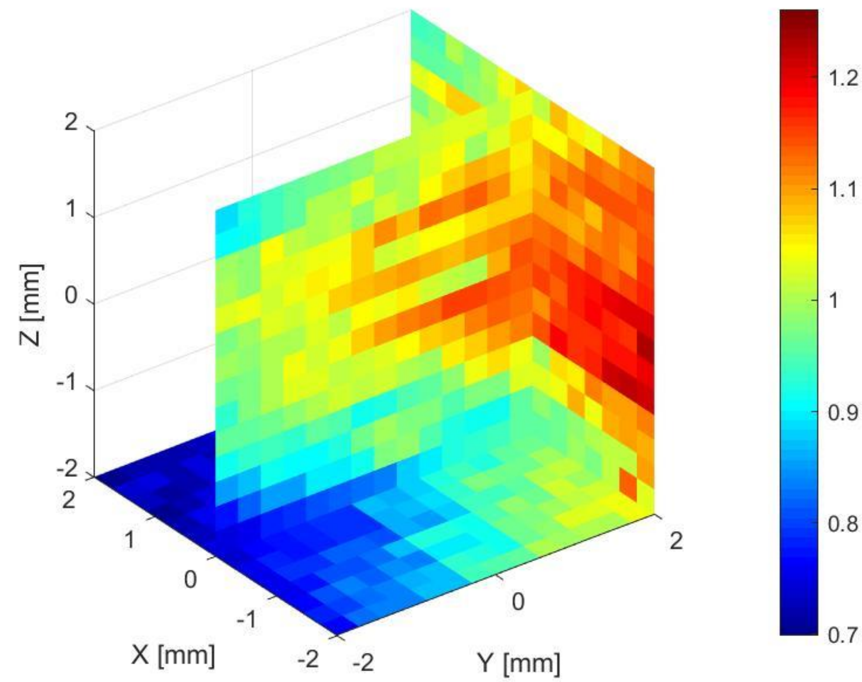
2
1
0
-1
-2
Z [mm]
2
1
0
-1
-2
X [mm]
-2
0
2
Y [mm]
1.2
1.1
1
0.9
0.8
0.7

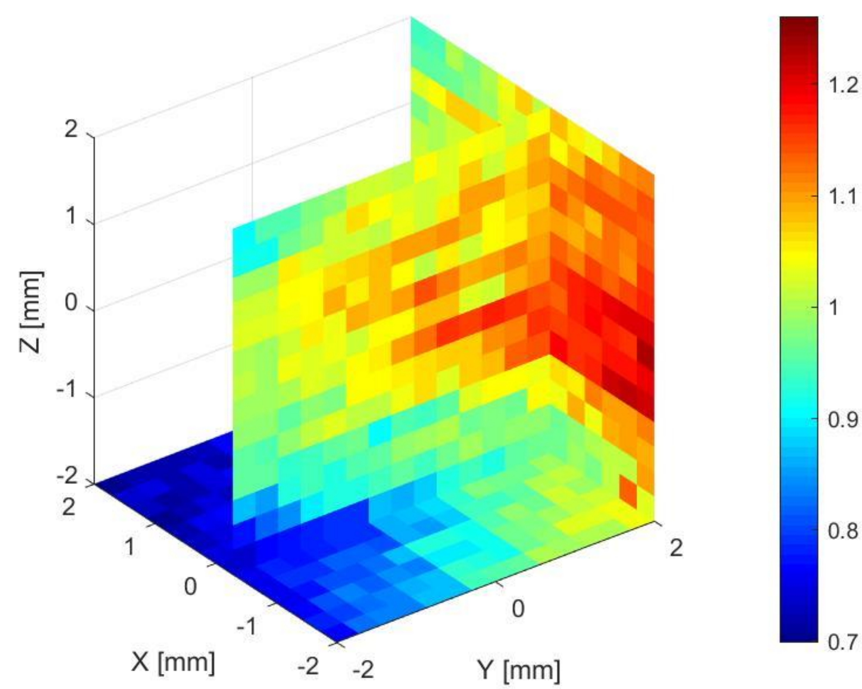
2
1
0
-1
-2
Z [mm]
2
1
0
-1
-2
X [mm]
-2
0
2
Y [mm]
1.2
1.1
1
0.9
0.8
0.7

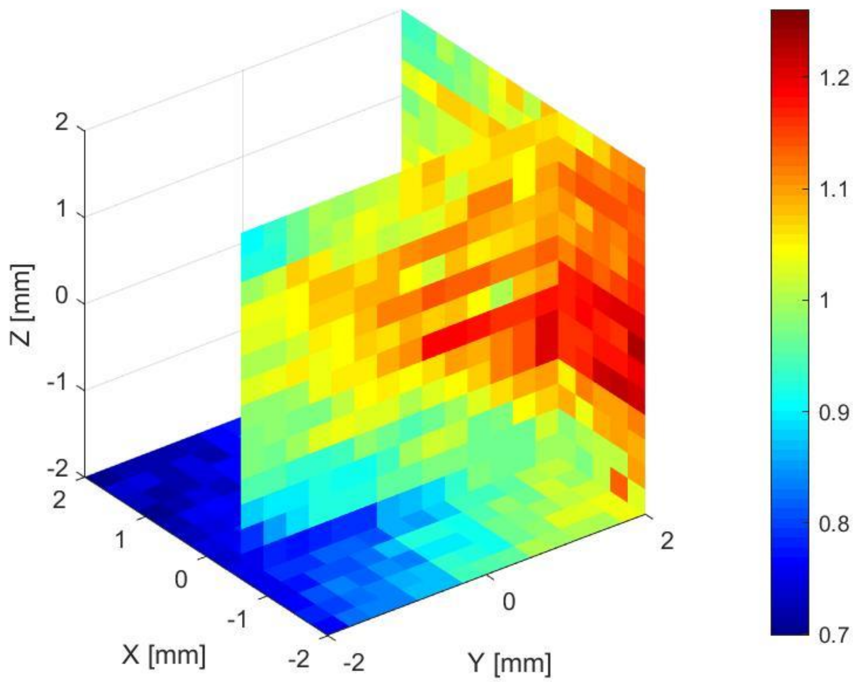

Z [mm]
X [mm]
Y [mm]

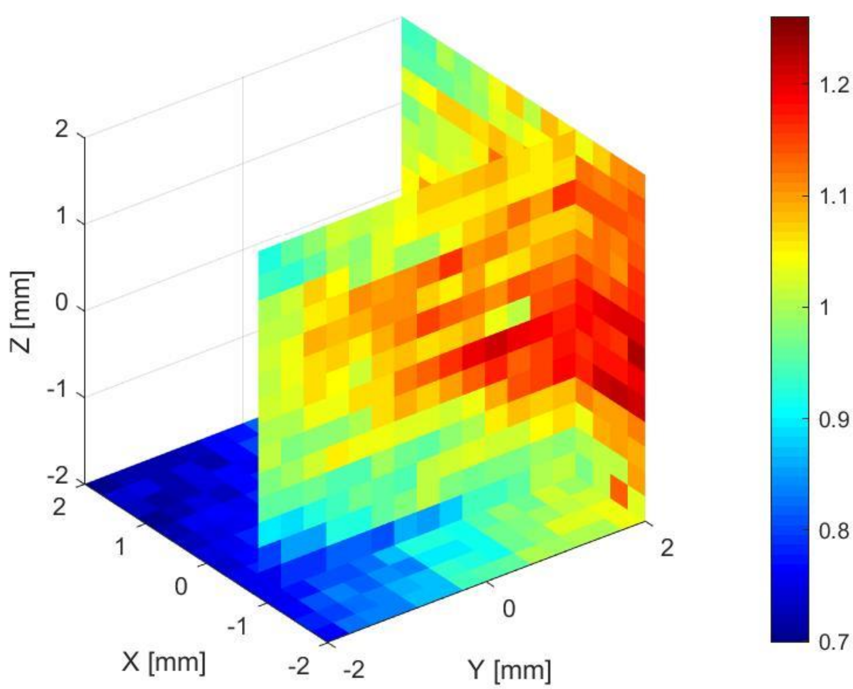

Z [mm]
X [mm]
Y [mm]

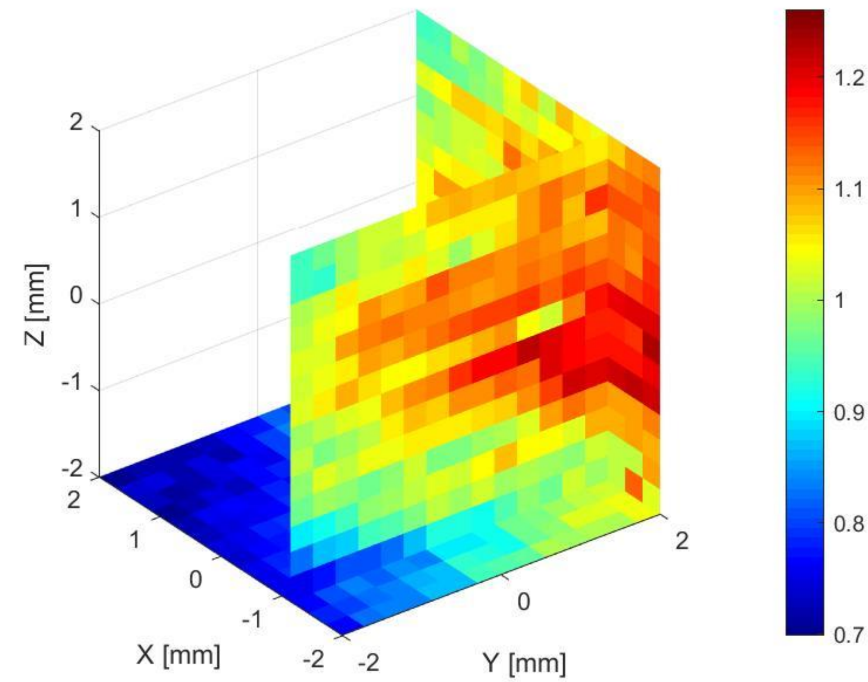
Z [mm]
2
1
0
-1
-2
X [mm]
2
1
0
-1
-2
Y [mm]
-2
0
2
1.2
1.1
1
0.9
0.8
0.7

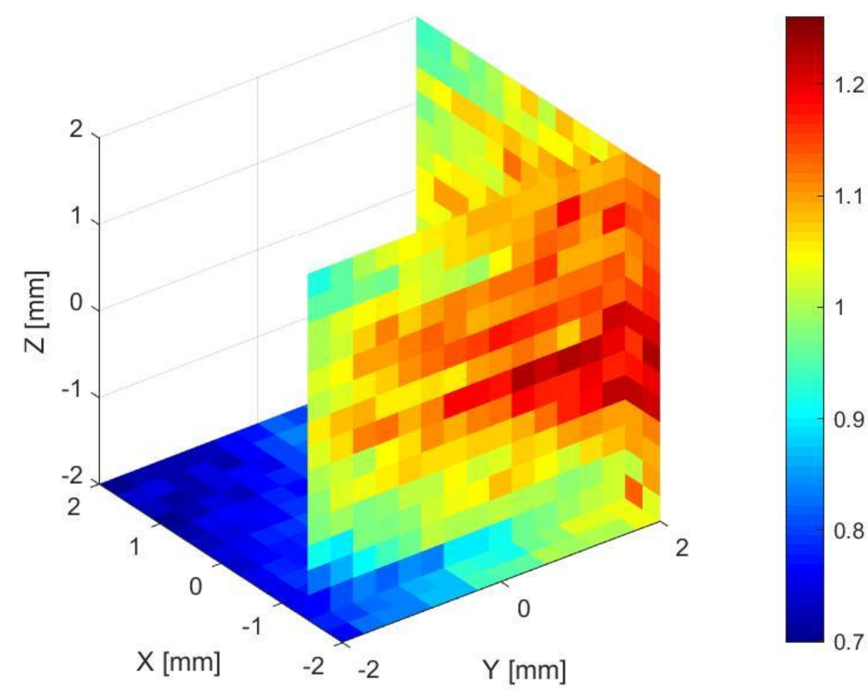
Z [mm]
2
1
0
-1
-2
X [mm]
2
1
0
-1
-2
Y [mm]
-2
0
2
1.2
1.1
1
0.9
0.8
0.7

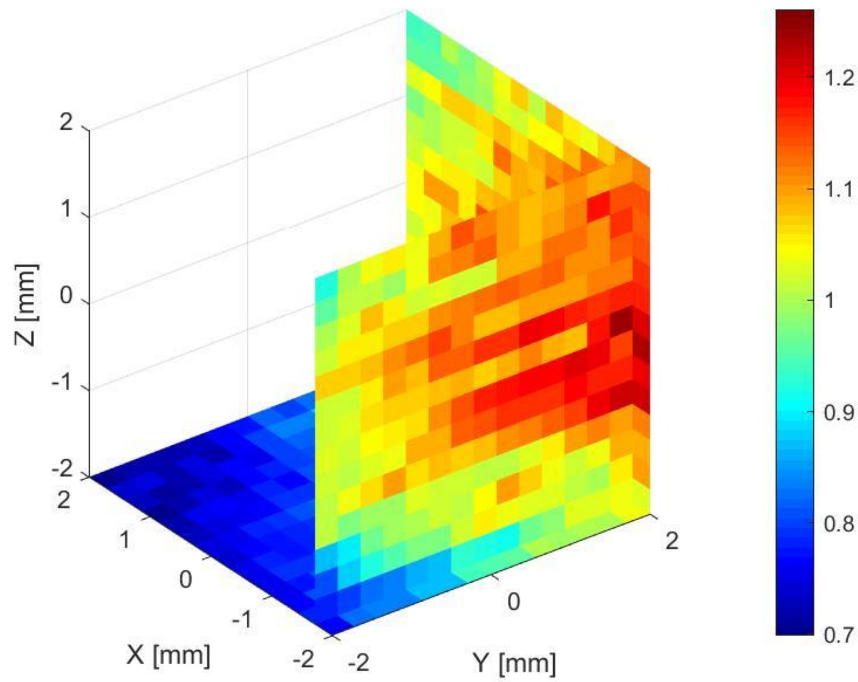

Z [mm]
X [mm]
Y [mm]

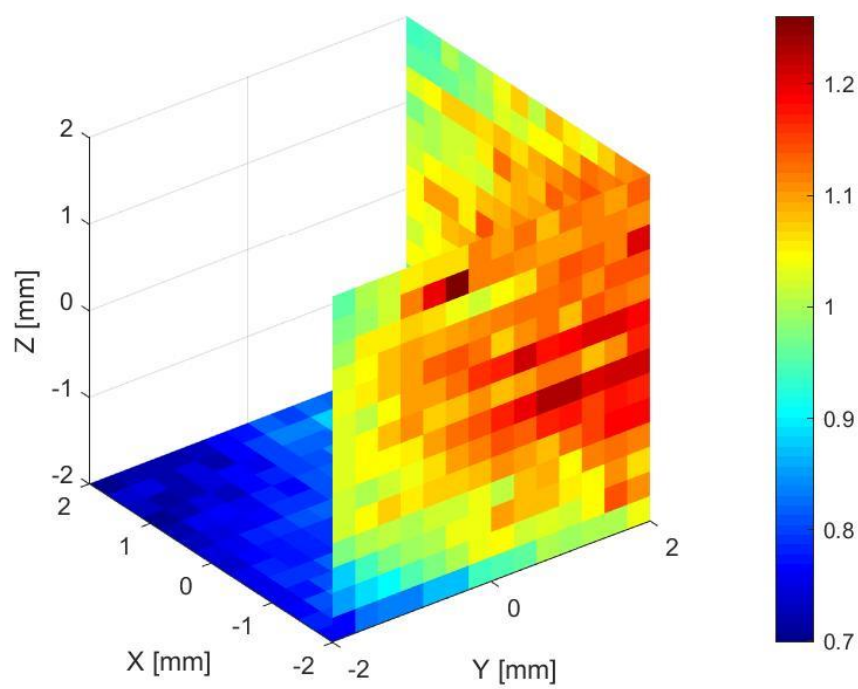

Z [mm]
X [mm]
Y [mm]